A METAMATERIAL WAVEGUIDE INCORPORATING ELECTRIC COUPLING FOR CONTACTLESS DATA AND POWER TRANSFER

Yue Li
Jesus College
Department of Engineering Science
University of Oxford

A thesis submitted for the degree of Doctor of Philosophy
Trinity term 2015

This page is intentionally left blank

To my parents and grandma,

Lan Lü and Jinghai Li

Yuzhen Wang

ACKNOWLEDGEMENTS

This thesis marks the end of an incredible journey I have been taking for the last four years. I would like to thank many people for their support, help and encouragement along the way.

First and foremost, I would like to thank my supervisor Prof. Chris Stevens for all his time and support. He has taught me how to look positively at failures and benefit from them. His enduring enthusiasm for research has always been a very important source of my motivation and persistence. I also greatly appreciate all his suggestions and the many fruitful discussions I have had with him, which helped shape this project in fundamental ways.

I would like to thank my previous colleague Dr Chris Chan for his help in the lab and for many interesting discussions both on and off the topic.

I would like to thank Mr Grahame Faulkner for his extensive technical support during my study and Prof. David Edwards for his funding support for building two-dimensional waveguide structures.

I would like to thank Prof. Ekaterina Shamonina for giving me the chance to work for her project and for many interesting discussions.

I would like to thank all my colleagues in the Oxford Communication Research Group for their esteemed and most rewarding friendship.

I would like to thank all my friends for their support along the journey. In particular, I would like to thank Dr Liang Kong for exploring Oxford with me and for being such an interesting and caring friend. I would also like to thank Dr Luyun Jiang for always being a superb cheerleader, especially throughout my writing-up time and for sharing a lot with me.

I would like to thank my parents and my grandma for always being there for me. I appreciate all the love, understanding and support I received from them.

Finally, I would like to thank mon petit ami Yue Dong for talking to me, understanding me, tolerating me, helping me and loving me.

ABSTRACT

The background to this study is an effort to exploit a magneto-inductive waveguide (MIW) for near-field contactless data and power transfer applications. MIWs are almost purely magnetically coupled metamaterial waveguides whose coupling strengths can never exceed the limit of conservation of magnetic flux.

This study raises the hypothesis that the coupling strength limit of MIWs can be overcome by incorporating additional electric coupling into the structures; therefore, more strongly coupled metamaterial waveguides can be built and serve as contactless near-field communication channels with wider passbands and lower attenuations. The hypothesis was tested in this study by investigating a new variant of the metamaterial waveguide: the Capacitor-Connected Grid (CCG), in which additional electric coupling is introduced by connecting coupling capacitors over inter-element gaps between conventional MIW metallic loop resonators.

The study investigates the dispersion and attenuation characteristics of both one- (1-D) and two-dimensional (2-D) CCG devices, leading to a discussion on their potential uses in ultra-wideband (UWB) contactless near-field data transfer applications. A mixed coupling model calculating inter-element mixed coupling coefficients for arbitrarily configured CCG waveguides is derived based on the state-of-the-art, taking into account the shift of resonant frequency caused by electric coupling. The study also looks at terminal optimizations for 1-D CCG with a view to maximizing power transfer efficiency.

A highlight of this study is that a 1-D CCG demonstration device in theory should be able to achieve 192.4% fractional bandwidth, which exceeds the 20% requirement of a UWB channel by a factor of 9.6, and is only $\frac{1}{10}$ of the minimum attenuation of an equivalent-sized MIW

device. Similar communication characteristics have also been found at selected transmission paths on a 2-D CCG demonstration structure.

The results of this study on CCG waveguides verify the hypothesis that incorporating additional electric coupling into an almost purely magnetically coupled waveguide can improve its coupling strength and thereby achieve a communication channel with larger bandwidths and lower losses.

The work on this thesis is accompanied by the following publications:

(1) Y. Li, C. J. Stevens, “Terminal Optimization for Wireless Power Transfer with Capacitor-Connected Grids Metamaterial Waveguides”, 9th International Congress on Advanced Electromagnetic Materials in Microwaves and Optics, Oxford, UK, 2015.

(2) C. J. Stevens, Y. Li, C. W.T. Chan, “Forward magneto-inductive wave propagation in planar magnetically coupled capacitor grids,” Journal of Electromagnetic Waves and Applications, Vol. 29, No. 6, pp. 753 – 762, 2015.

(3) Y. Li, C. J. Stevens, C. W. T. Chan, “Waveguide,” (Patent), WO2015033168 A1, PCT/GB2014/052716, Filing date: Sept 9, 2014.

(4) Y. Li, C. J. Stevens, "Capacitor Connected Grids for Wireless Power Transfer", IEEE Wireless Power Transfer Conference (WPTC), pp.122-125, Jeju, Korea, 2014,

(5) Y. Li, C. W. T. Chan, and C. J. Stevens, “Two-Dimensional Capacitor-Connected Grids Metamaterial Waveguide for UWB Contactless Data Transfer Channels,” 2013 Internal Conference on Electromagnetics in Advanced Applications, pp. 1437–1441, Torino, Italy, 2013.

(6) Y. Li, C.W. T. Chan, and C. J. Stevens, “Capacitor-Connected Grids as One-Dimensional UWB Data Transfer Channels,” 7th International Congress on Advanced Electromagnetic Materials in Microwaves and Optics, pp. 19-21, Bordeaux, France, 2013.

(7) Y. Li, C.W. T. Chan, and C. J. Stevens, “Dispersion Characteristics of Two-dimensional Capacitor-connected Grids,” 7th International Congress on Advanced Electromagnetic Materials in Microwaves and Optics, pp. 337-339, Bordeaux, France, 2013.

TABLE OF CONTENTS

CHAPTER 1

INTRODUCTION

1.1 Background to and Motivation for the Study

Electronic devices typically require physical internal electrical connections for power and data transfer via large numbers of soldered pins and wires. Technology convergence has continued to increase the number of chips that can be integrated onto printed circuit boards (PCBs), while reducing the size of electronic devices in each succeeding generation. The conventional PCB assembly method can no longer meet the growing need for high-density packaging techniques with large numbers of power and signal lines.

Recently, contactless data and power transfer via an inductive link [1] has been proposed as an alternative power and communication channel, in which the number of soldered pins can be greatly reduced, thereby producing more space for other components in the system. Previous studies have investigated contactless data and power links on both PCB-chip levels and package levels [2], [3] under similar schemes. Such contactless links are sequences of relay coils [1] coupled to one another via their mutual inductance so that the power and data are wirelessly supplied via magnetic field resonance coupling between source and receiver coils [4].

Stevens [5] offers a new view on relay coil sequences from a metamaterial [6] perspective. It was shown that relay coil sequences are essentially identical structures to magneto-inductive waveguides (MIWs), a novel metamaterial waveguide proposed by Shamonina *et al*. [7] in 2002. In particular, relay coil sequences transfer data and power via the propagation of magneto-inductive (MI) waves in the same way as MIWs. Given the knowledge gained about the physical properties of MIWs, Stevens *et al*. [5], [8] – [11] have exploited the potential of MIWs as one-dimensional (1-D) and two-dimensional (2-D) contactless near-field data and power transfer channels.

A strongly coupled MIW structure, by its very nature, offers low loss and wide bandwidth data transfer, while at the same time being also perfectly prepared for efficient power transfer. In order to build a more efficient data and power transfer channel, extensive efforts have been made to enhance magnetic coupling strength in MIWs, including adjusting inter-element separations and orientations [12], redesigning element shapes [13], introducing positional shifts between elements [14] and improving fabrication methods [15]. However, the magnetic coupling strength is limited by magnetic flux conservation.

Given this limit of magnetic coupling, the key research question addressed by this thesis is: can we make use of the electric coupling to enhance the overall coupling strength of metamaterial waveguides, overcoming the limit of magnetic coupling? This question could be answered by introducing additional electric coupling into conventional MIW structures and observing how the electric coupling interacts with the magnetic coupling and contributes to the overall coupling strength of metamaterial waveguides.

1.2 Overview of the Study

This study is mainly concerned with the investigation of a new variant of metamaterial waveguide – the Capacitor-Connected Grid (CCG) – which incorporates both magnetic coupling and electric coupling. By its very nature, the magnetic coupling strength in a CCG waveguide is fixed once the geometry of the resonators is determined, while the electric coupling can be readily varied by choosing different values of the coupling capacitors.

This study aims to analyse, both theoretically and experimentally, the dispersion properties of 1-D and 2-D CCG metamaterial waveguides, to better understand the coupling mechanisms of CCGs by describing the interactions between magnetic coupling and electric coupling, and to explore the potential for CCG metamaterial waveguides to be applied as contactless near-field data and power transfer channels.

The major challenges of this study are as follows:

1. **Characterization of 1-D CCG metamaterial waveguides**

   It is essential to characterize the dispersion properties of a 1-D CCG structure, both theoretically and experimentally, as they determine the physical behaviours of such a waveguide and its transmission properties. Other properties such as geometric dimensions, propagation loss, group velocity, bandwidth and propagation modes are also very important when exploring the potential applications of this waveguide, and therefore they will be carefully investigated in this study.

   The characterization of 1-D CCG structures can lead to a discussion on the coupling mechanism of this waveguide, describing the interactions between magnetic coupling and electric coupling. The coupling mechanism of CCG waveguides can be generalized to many different metamaterial waveguides that may be constructed based on the same principle.

2. **Derivation of a mixed coupling model**

   A CCG structure is an example of mixed coupling metamaterial waveguides which incorporate both magnetic and electric coupling. The next step in this study is to find a method for calculating inter-element mixed coupling coefficients for arbitrarily configured CCG waveguides. By separately evaluating the electric and magnetic contributions to the mixed coupling coefficient, one is able to readily adapt the design of many mixed coupling waveguides to different requirements.

3. **Dimensional extension to 2-D CCG metamaterial waveguide surfaces**

   The dimensional extension from 1-D to 2-D has proven to offer an increased bandwidth and a reduced loss in the study of conventional MIWs [9], [13]. This study of CCGs follows the same route to explore the behaviours of a 2-D CCG metamaterial waveguide surface. The frequency-dependent current distribution over a 2-D CCG surface will be examined in order to identify the available transmission paths. The dispersion properties of selected transmission paths on the 2-D surface will be analysed, both theoretically and experimentally, along with other important features, including propagation loss, group velocity, bandwidth, and propagation modes.

4. **Exploration of the potential of CCG waveguides for use in contactless data and power transfer**

   The potential for using CCG devices as 1-D or 2-D data transfer channels to link near-field coupled devices at high bandwidth and low loss will be discussed, along with the characterization of these structures. This study will also explore the potential of 1-D CCG waveguides to be used as contactless power transfer channels, focusing on terminal optimizations with a view to offering maximized power transfer efficiency.

1.3 Thesis Structure

Chapter 2 reviews a brief history of metamaterials and serves as an introduction to the basic concepts and equations of metamaterial waveguides. An overview of the two types of slow waves propagating along metamaterial waveguides: magneto-inductive (MI) waves and electro-inductive (EI) waves is given, followed by a discussion of the potential of metamaterial waveguides to be used in contactless near-field data and power transfer applications.

Chapter 3 proposes the design of 1-D CCG metamaterial waveguides with the aid of a quasi-static mesh circuit model. The dispersion equation of a 1-D CCG device is derived based on Kirchhoff's Voltage Law, followed by an analysis of the dispersion and attenuation properties calculated for a given demonstration structure. Other properties, including group velocity, bandwidth and propagation modes, are carefully investigated, along with a discussion of the potential of this structure for use in contactless near-field data transfer. The characterization of the 1-D CCG waveguide leads to a discussion on its coupling mechanism, which describes the interaction between magnetic and electric coupling.

In addition, Chapter 3 reviews the state-of-the-art model [16] which calculates inter-element mixed coupling coefficient for split-ring resonators. This existing model is adjusted to CCG structures based on the difference between spilt-ring resonators and CCG structures. The adjusted coupling model allows separate evaluation of the electric and magnetic contributions to the mixed coupling coefficient. This adjusted coupling model also allows direct derivation of the dispersion equations and impedance matrix based on the values of the self-impedance and mutual impedance of a metamaterial waveguide. When analysing structures with complex electrical circuits, this model helps to reduce the effort in applying Kirchhoff's Voltage Law to mesh circuit models and allows the design of many mixed coupling waveguides to be readily adapted to different requirements.

Chapter 4 presents a simple experiment conducted to verify the analytical analysis of 1-D CCG devices. The experimental dispersion characteristics are extracted from the measurements by two different methods and the extracted dispersion characteristics are compared with analytical predictions.

Chapter 5 advances the study of CCG devices to their 2-D extension and the proposed 2-D CCG waveguide surfaces. The frequency-dependent current distribution over a 2-D CCG surface is examined in order to identify the available transmission paths. The dispersion properties of selective transmission paths on the 2-D surface are analysed both theoretically and experimentally, along with other important features, including propagation loss, group velocity, bandwidth and propagation modes. This chapter also discusses the potential of a 2-D CCG waveguide surface to be exploited in a multipath and multi-terminal contactless near-field data transfer medium.

Chapter 6 investigates the potential of 1-D CCG structures to be used as contactless power transfer devices, focusing on terminal optimizations with a view to offering maximized power transfer efficiency. The optimal terminal design is derived under the reflectionless matching condition, which states that a non-reflective waveguide can be formed by inserting a terminating impedance that behaves as a semi-infinite line and gives to a finite structure the input property of an infinite line. A simple experiment is conducted which proves that the proposed optimal terminal design can successfully absorb all the incident power at the line end.

Chapter 7 presents the conclusions drawn from the research carried out for this thesis, along with ideas for future work in the field of metamaterial waveguides, with a view to further developing their potential in contactless near-field data and power transfer applications.

CHAPTER 2

LITERATURE REVIEW

For the convenience of later discussions on CCG metamaterial waveguides, this chapter reviews a brief history of metamaterials and serves as an introduction to the basic concepts and equations of metamaterial waveguides. This chapter also contains an overview of previous studies exploring the potential of metamaterial waveguides for use in contactless near-field data and power transfer applications.

2.1 Brief Introduction to Metamaterials

All materials in nature are composites, consisting of atoms and molecules, which determine the electromagnetic (EM) properties of a material. A number of desirable EM properties appear to be lacking in natural materials, even though there are no physical laws preventing the existence of such properties [6]. The exploration of artificial materials, in which atoms and molecules are replaced by macroscopic, synthetic elements, offers the possibility of realizing novel EM properties. By tailoring individual elements as well as their interactions, the propagation of EM waves within a material can be manipulated to allow it to exhibit exceptional EM properties that have not been readily observed in nature. One can generally divide artificial materials into two categories: when the wavelength is comparable with element dimensions, the Bragg Effect [17] comes into play, giving rise to photonic bandgap materials [18] – [22]; when the wavelength is much larger than element dimensions, the effective-medium approximation applies, giving rise to metamaterials [23] – [30].

The most famous example of building metamaterials for non-natural properties refers to 'left-handed material' (LHM), in which both the permittivity (ε) and the permeability (μ) are negative. This idea was originally proposed by Viktor G. Veselago [31], namely, that one may be able to make a substance with $\varepsilon < 0$ and $\mu < 0$ simultaneously, in which the three vectors, the electric field, the magnetic field and the wave vector ($\vec{E}, \vec{H}, \vec{k}$) constitute a left-handed set. Propagation of EM waves described by the wave vector $\vec{k}$ is contrary to the direction of energy flux, resulting in backward wave propagation in LHM. This can lead to various unusual phenomena, such as the reversal of the Doppler Effect, the reversal of Snell's Law and the reversal of the Valilov-Cherenkov Effect. In [31], Veselago then proceeded from the phenomenon of negative refraction to show that a lens with plane parallel boundaries could bring a diverging beam emitted on one side of the lens to a focus on the other side [32]. Veselago's work was ignored for a long time, until Pendry designed the first realization of LHM. Pendry's initial idea was that metallic wires aligned along the direction of wave propagation could provide a metamaterial with negative permittivity [33], [34] and that split ring resonators (SRRs) with their axis similarly aligned could achieve negative permeability [35]. Smith *et al*. [36] demonstrated the first experimental evidence for LHM, which consisted of a bulky combination of metal wires and SRRs disposed in alternating arrows. The proof of negative refraction came shortly afterwards by Shelby *et al*. [37], [38]. Meanwhile, Pendry [39] further developed Veselago's plane parallel lens, showing that it was capable of subwavelength imaging and calling it 'the perfect lens'.

This early pioneering work on LHM opened the floodgates on metamaterial research. Since then, researchers have achieved a variety of exceptional EM properties by tailoring individual metamaterial elements as well as the interactions between them [40] – [55]. Possible applications range from electronics and telecommunications to sensing, biomedical instrumentation, aerospace and data storage.

2.2 Coupling Mechanism Between Metamaterial Elements

Many metamaterial structures are composed of periodic arrays of identical coupled resonators. The properties of these structures depend not only on the parameters describing individual resonators but also on the mutual couplings between them.

There are two types of mutual coupling that exist between metamaterial elements: magnetic coupling and electric coupling. The definitions of the two types of coupling are introduced in Sections 2.2.1 and 2.2.2, respectively. Section 2.2.3 reviews the coupling mechanism between metamaterial elements, describing the interaction between the two types of coupling [56].

2.2.1 Magnetic coupling and mutual inductance

In the case that only magnetic coupling is concerned, an equivalent lumped-element circuit model as shown in Fig. 2-1 can be used to represent a pair of inductors.

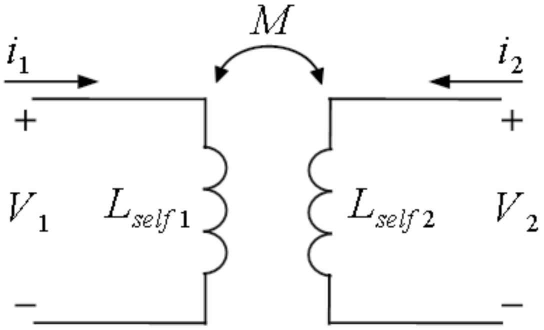

Fig. 2-1 *Circuit representation of magnetic coupling effect*

The interaction between the two inductors is described from the terminal on the left hand side by Eq. (2.1), where i_1, i_2 and v_1, v_2 are circulating currents and total voltage in the 1^{st} and 2^{nd} loops, $L_{self\,1}$ and $L_{self\,2}$ and are self-inductances in the 1^{st} and 2^{nd} loops, and M is the mutual inductance.

$$V_1 = L_{self\,1}\frac{di_1}{dt} + M\frac{di_2}{dt} \tag{2.1}$$

The mutual inductance can be defined as follows: A current carrying loop sets up a magnetic flux in space. A second open circuited loop couples some of the flux and a voltage is developed across the terminals. This definition of mutual inductance can be expressed as Eq. (2.2):

$$M = \frac{\Phi_2}{i_1} \tag{2.2}$$

That is to say it is the magnetic flux coupling the second loop relative to the current that produced that flux in the original loop.

If the magnetic field generated by one loop is in the same direction at the centre of the other loop, the mutual inductance is positive, $M > 0$; if they are in the opposite direction, the mutual inductance is negative, $M < 0$.

Assuming the two loops are identical, one can have $L_{self\,1}=L_{self\,2}=L_{self}$. The magnetic coupling coefficient k_m can be expressed as Eq. (2.3), which is the ratio between mutual inductance and self-inductance.

$$k_m = \frac{2M}{L_{self}} \tag{2.3}$$

2.2.2 Electric coupling and mutual capacitance

In the case that only electric coupling is concerned, an equivalent lumped-element circuit model as shown in Fig. 2-2 can be used to represent a pair of capacitors.

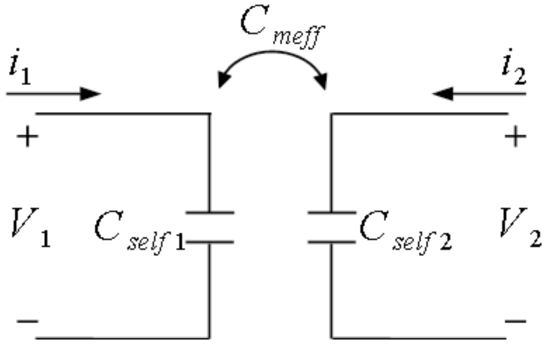

***Fig. 2-2** Circuit representation of electric coupling effect*

The interaction between the two capacitors is described from the terminal on the left hand side by Eq. (2.4), where i_1, i_2 and V_1, V_2 are circulating currents and total voltage in the 1^{st} and 2^{nd} loops, $C_{self\,1}$ and $C_{self\,2}$ and are self-inductances in the 1^{st} and 2^{nd} loops, and C_{meff} is the mutual capacitance.

$$i_1 = C_{self\,1}\frac{dV_1}{dt} + C_{meff}\frac{dV_2}{dt} \tag{2.4}$$

The mutual capacitance can be defined as follows: A voltage across two conductors sets up a electric field and a corresponding electric flux. A second capacitor consisting again of two conductors is placed within this electric field. The second capacitor's two conductors are short circuited and the amount of electric flux that couples the composite conductor is equal to the charge that is induced on it. This definition of mutual capacitance can be expressed as Eq. (2.5):

$$C_{meff} = \frac{q_2}{V_1} \tag{2.5}$$

That is to say the mutual capacitance is the ratio of coupled electric flux relative to the voltage that produced that flux in the first capacitor.

If the charge generated across one loop has the same sign as the charge across the other loop, the mutual capacitance is positive, $C_{meff} > 0$; if they have the opposite signs, the mutual capacitance is negative, $C_{meff} < 0$.

Assuming the two loops are identical, one can have $C_{self\,1}=C_{self\,2}=C_{self}$. The electric coupling coefficient k_e can be expressed as Eq. (2.6), which is the ratio between mutual inductance and self-inductance.

$$k_e = \frac{2C_{meff}}{C_{self}} \tag{2.6}$$

2.2.3 Coupling Mechanism between Metamaterial Elements

The coupling mechanism between metamaterial resonators depends on the frequency range applied, as discussed in [57]. It has been experimentally verified that the coupling between metamaterial resonators operating at MHz frequencies is nearly purely magnetic [58], and magnetic coupling is always negative for a coplanar case and positive for a coaxial case. In the GHz range, the coupling contains a significant electric component [59], [16], [60] and a strong coupling anisotropy arises [16].

Depending on the relative orientations between resonators in a plane, in the GHz range magnetic and electric coupling may take either a positive or a negative sign, and therefore the two may reinforce or counteract each other [59], [16]. This implies that the overall coupling can be dominated by either magnetic or electric coupling, which then leads to completely different dispersion relationships, and there can be configurations in which the two components of the coupling factor compensate for each other to eliminate coupling. A further increase in frequency to the THz range gives rise to effects related to the kinetic inductance [16].

Metamaterial structures can affect not only the propagation of transverse EM waves but can also support two types of slow longitudinal waves, magneto-inductive (MI) waves [7] and electro-inductive (EI) waves [61]. Slow waves are those whose phase velocities are much smaller than the light velocity. The propagation of MI waves comes as a consequence of magnetic coupling between metamaterial resonators, while EI waves owe their existence to electric coupling between resonators.

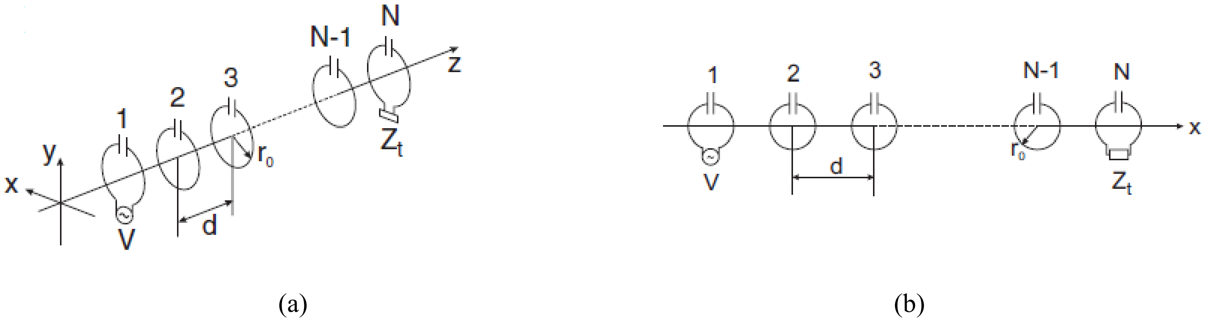

(a) (b)

Fig. 2-3 *Schematic representation of (a) a coaxial array; (b) a coplanar array of capacitively loaded loops of radius* r_0 *placed at distance d from each other. This figure is taken from* [62].

2.3 Magneto-inductive Waves

In 2002, Shamonina *et al.* [7] first proposed the magneto-inductive waveguide (MIW), a magnetically coupled chain of one-dimensional (1-D) metamaterial resonators, as a medium for supporting the propagation of MI waves. The dispersion characteristics of MI waves have been analysed both theoretically and experimentally [62] – [64].

The simplest realization of an MIW element is a capacitively loaded loop [65]. An MIW could be modelled as a simple series of RLC resonators [66] which are coupled together via mutual inductance. Schematic presentations of two configurations of MIW are shown in

Fig. 2-3, where a finite array (N elements) of capacitively loaded loops of radius r_0 is placed (a) coaxially and (b) coplanarly at a distance d from each other [62].

When considering a finite length of 1-D MIW (N elements), its impedance matrix $\boldsymbol{Z}$ can be described by an N×N square matrix as given by Eq. (2.7).

$$\boldsymbol{Z} = \begin{pmatrix} Z_0 & j\omega M & 0 & \dots & \dots & \dots & 0 \\ j\omega M & Z_0 & j\omega M & 0 & \dots & \dots & \vdots \\ 0 & j\omega M & Z_0 & j\omega M & 0 & \dots & \vdots \\ \vdots & \ddots & \ddots & \ddots & \ddots & \ddots & \vdots \\ \vdots & \dots & 0 & j\omega M & Z_0 & j\omega M & 0 \\ \vdots & \dots & \dots & 0 & j\omega M & Z_0 & j\omega M \\ 0 & \dots & \dots & \dots & 0 & j\omega M & Z_0 \end{pmatrix} \tag{2.7}$$

where the impedance of a single element, Z_0, is positioned along the leading diagonal, and the coupling term $\boldsymbol{j\omega M}$ is on the off diagonals.

The magnetic fields threading two neighbouring elements are in the same direction in the coaxial case (M>0), while they are in the opposite directions in the coplanar case (M<0) [29].

When considering a two-dimensional (2-D) structure, a new coupling term representing the magnetic coupling between diagonally adjacent elements M_{diag} needs to be taken into account. For an M×N 2-D array (M rows and N columns), one can obtain an M×M impedance matrix as given by Eq. (2.8):

$$\boldsymbol{Z} = \begin{pmatrix} \boldsymbol{A} & \boldsymbol{B} & 0 & \dots & \dots & 0 \\ \boldsymbol{B} & \boldsymbol{A} & \boldsymbol{B} & 0 & \dots & \vdots \\ 0 & \boldsymbol{B} & \ddots & \ddots & \ddots & \vdots \\ \vdots & \ddots & \ddots & \ddots & \boldsymbol{B} & 0 \\ \vdots & \dots & 0 & \boldsymbol{B} & \boldsymbol{A} & \boldsymbol{B} \\ 0 & \dots & \dots & 0 & \boldsymbol{B} & \boldsymbol{A} \end{pmatrix} \tag{2.8}$$

where matrix $\boldsymbol{A}$ describes couplings inside a row and matrix $\boldsymbol{B}$ describes inter-row couplings. The size of both $\boldsymbol{A}$ and $\boldsymbol{B}$ is N×N. $\boldsymbol{A}$ and $\boldsymbol{B}$ are as defined in Eqs. (2.9) and (2.10), respectively:

$$\boldsymbol{A} = \begin{pmatrix} Z_0 & j\omega M & 0 & \dots & \dots & \dots & 0 \\ j\omega M & Z_0 & j\omega M & 0 & \dots & \dots & \vdots \\ 0 & j\omega M & Z_0 & j\omega M & 0 & \dots & \vdots \\ \vdots & \ddots & \ddots & \ddots & \ddots & \ddots & \vdots \\ \vdots & \dots & 0 & j\omega M & Z_0 & j\omega M & 0 \\ \vdots & \dots & \dots & 0 & j\omega M & Z_0 & j\omega M \\ 0 & \dots & \dots & \dots & 0 & j\omega M & Z_0 \end{pmatrix} \tag{2.9}$$

$$\boldsymbol{B} = \begin{pmatrix} j\omega M & j\omega M_{diag} & 0 & \dots & \dots & \dots & 0 \\ j\omega M_{diag} & j\omega M & j\omega M_{diag} & 0 & \dots & \dots & \vdots \\ 0 & j\omega M_{diag} & j\omega M & j\omega M_{diag} & 0 & \dots & \vdots \\ \vdots & \ddots & \ddots & \ddots & \ddots & \ddots & \vdots \\ \vdots & \dots & 0 & j\omega M_{diag} & j\omega M & j\omega M_{diag} & 0 \\ \vdots & \dots & \dots & 0 & j\omega M_{diag} & j\omega M & j\omega M_{diag} \\ 0 & \dots & \dots & \dots & 0 & j\omega M_{diag} & j\omega M \end{pmatrix} \tag{2.10}$$

The excitation is assumed to be a voltage V of frequency $\boldsymbol{\omega}$ in the first loop. The dispersion relationship can be obtained by applying Kirchhoff's Voltage Law to the $\boldsymbol{n^{th}}$ element and can be written as Eq. (2.11). The nearest-neighbour coupling approximation, which was validated in [63], is applied here for simplicity.

$$k_m \cosh(\gamma d) = \frac{{\omega_0}^2}{\omega^2} - 1 + \frac{j}{Q}\frac{\omega_0}{\omega} \tag{2.11}$$

where $\omega_0 = \frac{1}{\sqrt{L_{MIW}C_{MIW}}}$ is the resonant frequency, $Q = \frac{\omega_0 L_{MIW}}{R}$ is the quality factor, L_{MIW}, C_{MIW} and R_{MIW} are the inductance, capacitance and resistance of a capacitively loaded loop, respectively, d is the lattice period of the structure, the propagation constant $\gamma = \alpha + j\beta$, where β and α are the wave number and attenuation coefficient, respectively. According to the definition in Eq. (2.3), the magnetic coupling coefficient of the MIW is given by Eq. (2.12):

$$k_m = \frac{2M}{L_{MIW}} \tag{2.12}$$

If the frequencies of interest are near enough to ω_0 such that $\frac{\omega_0}{\omega} \approx 1$, one can omit the term $\frac{\omega_0}{\omega}$ in Eq. (2.11).

If the omhic loss is negligible in which case $Q \rightarrow \infty$, the dispersion equation of MIWs in Eq. (2.11) can be simplified to Eq. (2.13).

$$\frac{{\omega_0}^2}{\omega^2} - 1 = k_m \cosh(\gamma d) \tag{2.13}$$

Using a similar analysis for a coplanar 2-D array [63], where the lattice period d is the same for both the x and y directions, one arrives at the dispersion equation for 2-D MIWs, as given by Eq. (2.14):

$$\frac{{\omega_0}^2}{\omega^2} - 1 = k_m(\cosh(\gamma_x d) + \cosh(\gamma_y d)) \tag{2.14}$$

where γ_x and γ_y are propagation constants in the x and y directions, respectively. Using Eqs. (2.13) and (2.14), one can deduce that MI waves only propagate in a narrow passband centred on the resonant frequency ω_0, as given by Eq. (2.15). One consequence of this expression is that a 2-D MIW will have significantly greater bandwidth than a 1-D device.

$$\frac{1}{\sqrt{1 + \eta_x |k_m|}} \leq \frac{\omega}{\omega_0} \leq \frac{1}{\sqrt{1 - \eta_x |k_m|}} \tag{2.15}$$

$$\text{where } \eta_x = \begin{matrix} 2 \text{ for a 2-D MIW} \\ 1 \text{ for a 1-D MIW} \end{matrix}$$

The dispersion characteristics of a coaxial 1-D MIW and a coplanar 1-D MIW can be seen by representing its dispersion equation (Eq. (2.13)) in Fig. 2-4 (a) and (b), respectively.

In Fig. 2-4 (a), the coaxial case, positive magnetic coupling carries forward waves, of which the group velocity ($v_g = \frac{\partial \omega}{\partial \beta}$) and phase velocity ($v_p = \frac{\omega}{\beta}$) are in the same direction. In

Fig. 2-4 (b), the coplanar case, negative magnetic coupling results in the propagation of backward waves with group velocity and phase velocity in opposite directions.

The magnetic coupling coefficient k_m is limited by flux conservation and can be expressed as $|k_m| \leq 2$. It is worth mentioning that infinite bandwidth can be achieved when $|k_m| > 1$ [29]. There would still be a lower cut-off frequency, but the upper boundary of the passband extends to arbitrarily high frequencies with an asymptote, as in Eq. (2.16). The infinite bandwidth and the asymptote are illustrated in Fig. 2-5.

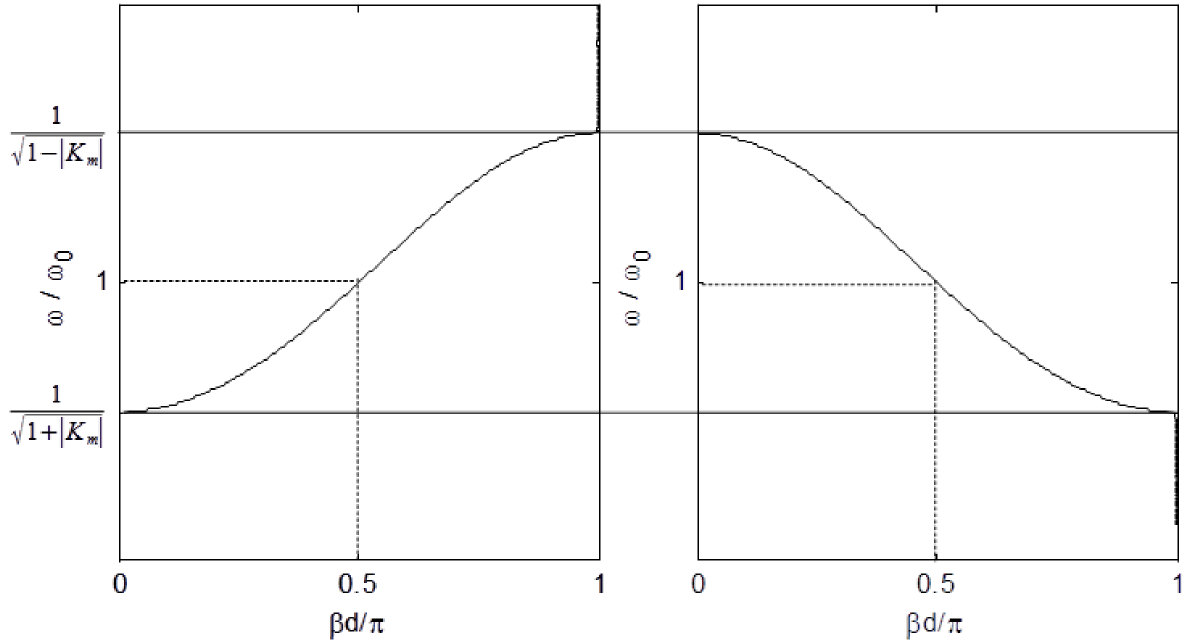

(a) (b)

Fig. 2-4 *Dispersion curve for (a) a coaxial array with k_m>0; and (b) for a coplanar array with k_m<0 under the lossless assumption, where R = 0, and the nearest-neighbour approximation.*

$$\beta d = arccos^{-1}\left(-\frac{1}{k_m}\right) \qquad (2.16)$$

Due to their wave-guiding property, MIWs can be considered as transmission lines. For all transmission lines, a terminating impedance at the line end absorbs all the incident power. The terminating impedance Z_{T-MIW} for MIWs was derived in [63] under the nearest-neighbour approximation, as given by Eq. (2.17):

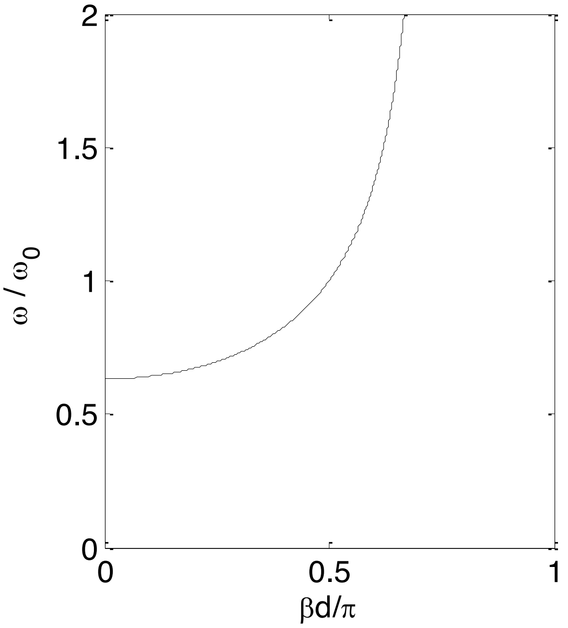

Fig. 2-5 *Dispersion curve for a coaxial MIW array with* k_m *= 1.5, which shows an arbitrarily high upper frequency limit. The limit of* $\frac{\beta d}{\pi}$ *goes to 0.73 in this case. This curve is plotted under the lossless assumption, where R = 0, and the nearest-neighbour approximation.*

$$Z_{T-MIW} = j\omega M e^{-\gamma d} \tag{2.17}$$

Previous studies have extensively characterized the behaviour and properties of MI waves, looking at retardation effects [67], coupling mechanisms [59], bi-periodic structures [68], properties of shifted coupled structures [14] and at approaches for manipulating near-field guiding properties [12].

2.4 Electro-inductive (EI) Waves

EI waves propagate on chains of electrically coupled metamaterial resonators. Metamaterial waveguides that support propagation of EI waves have come to be known as electro-inductive waveguides (EIWs). Beruete *et al*. [61] first considered a chain of electrically coupled complementary split ring resonators (CSRRs) as an EIW structure. A CSRR element [69], as shown in Fig. 2-6 (a), can be obtained from a conventional SRR (Fig. 2-6 (b)) by inversion of constituent materials, with metal being replaced by a dielectric, and vice versa, according to the Babinet Principle [70].

The equivalent circuit for a unit cell of CSRR is shown in Fig. 2-7, where L_C is the CSRR self-inductance, C_G is the capacitance to ground in the chain of CSRRs and C_M is the mutual capacitance between adjacent complementary split-ring resonators. Assuming C_C, the CSRR self-capacitance as defined in [69], then one can have $C_C = 2C_M + C_G$ under the nearest-neighbour approximation.

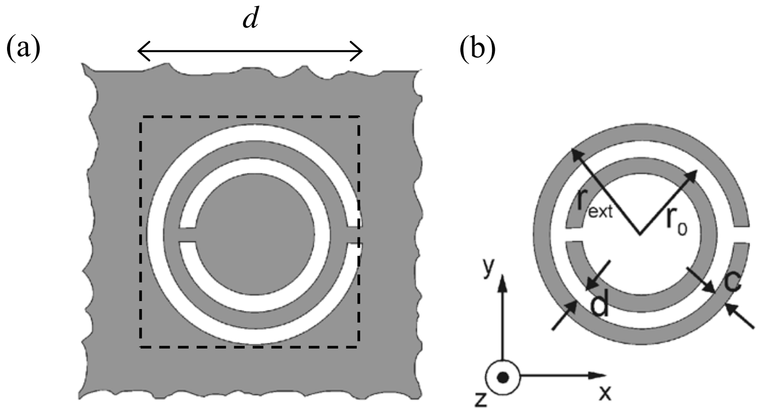

Fig. 2-6 *Topologies of (a) CSSR and (b) SRR, in which grey zones represent the metalization. The figure is taken from* [69].

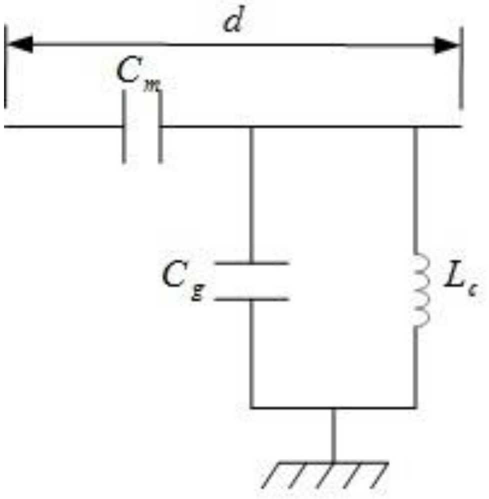

Fig. 2-7 *Equivalent circuit for a CSRR element. This figure is taken from* [61].

The dispersion relationship can be obtained by applying Kirchhoff voltage analysis to the $\boldsymbol{n^{th}}$ element and can be written as Eq. (2.18):

$$\frac{\omega^2}{{\omega_0}^2} = 1 + 2\omega^2 C_M L_C \cosh(\gamma d) \tag{2.18}$$

where the resonant frequency $\omega_0 = \frac{1}{\sqrt{L_C(2C_M + C_G)}}$, the propagation constant $\gamma = \alpha + j\beta$, where α and β are the attenuation coefficient and the wave number, respectively. According to the definition in Eq. (2.6), the electric coupling coefficient of the CSRR can be expressed in Eq. (2.19):

$$k_e = \frac{2C_M}{C_C} \tag{2.19}$$

Under the assumption of narrow bandwidth, where $\omega \approx \omega_0$, the dispersion equation for a lossless EIW can be simplified to Eq. (2.20):

$$\frac{\omega^2}{{\omega_0}^2} \approx 1 + k_e \cosh(\gamma d) \tag{2.20}$$

The width of the passband is proportional to the electric coupling strength, as given by Eq. (2.21), which is a dual form of Eq. (2.15):

$$\sqrt{1 - |k_e|} \leq \frac{\omega}{\omega_0} \leq \sqrt{1 + |k_e|} \tag{2.21}$$

In a similar manner to MIWs, the bandwidth performance of EIWs is limited by the inter-element electric coupling strength that can be achieved in practice. The electric coupling, which is determined by the geometric mutual capacitance C_M, is limited by the practical inter-element spatial proximity and the area size of parallel plates from adjacent resonators, which is limited by the thickness of the metal tracks.

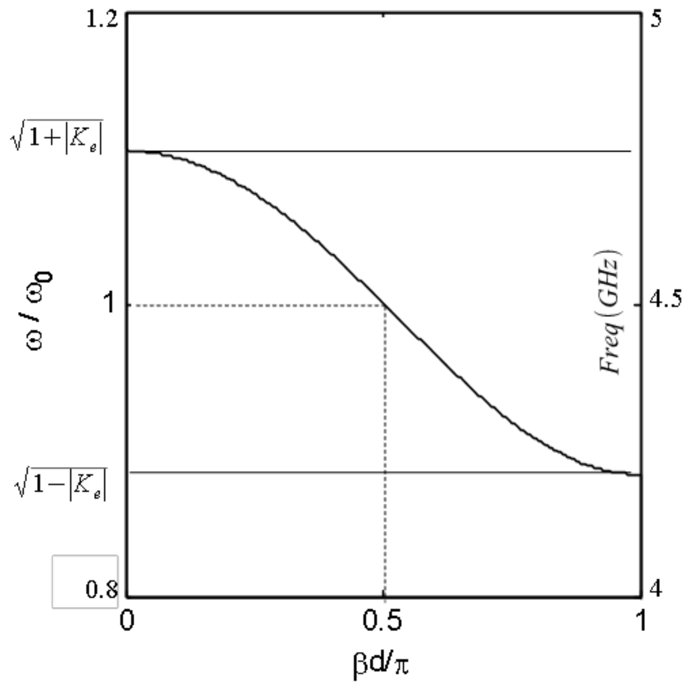

Fig. 2-8 *Dispersion curve for a chain of electrically coupled CSRRs with* k_e *= 0.22 and* f_0 *= 4.5 GHz under the lossless assumption.*

In the experiments described in [61], efforts were made to reduce ohmic losses and to increase the electric coupling strength for an EIW structure made of a chain of electrically coupled complementary squared split ring resonators (CSSRRs) [71]. The resulting EIW in [61] exhibits a passband roughly between 4 and 5 GHz. The dispersion relation of this CSSRR EIW structure can be reproduced as shown in Fig. 2-8 when k_e = 0.22 and f_0 = 4.5 GHz. It can be seen that a passband centred at ω_0 for EI wave propagation is achieved as described by Eq. (2.21).

The dispersion relation for MIWs as given by Eq. (2.13) can be further simplified to Eq. (2.22) under the weak coupling assumption, where $k_m \ll 1$, in order to observe its duality with the dispersion relation for EIWs given by Eq. (2.20):

$$\frac{\omega^2}{{\omega_0}^2} \approx 1 - k_m \cosh(\gamma d) \tag{2.22}$$

The dispersion relations given by Eqs. (2.20) and (2.22) coincide if the resonant frequencies ω_0 of the CSRRs and SRRs are the same. It is worth mentioning that ω_0 changes with varying electric coupling coefficient k_e as they are both a function of C_M in CSRRs, while ω_0 stays the same when varying magnetic coupling coefficient k_m in SRRs. In summary, EIWs propagate EI waves in the same manner as MIWs propagate MI waves [61].

2.5 Applications of Magneto-inductive Waveguides

Apart from the applicability of designing metamaterials with non-natural properties, there has been a surge of interest in exploring the magnetic guiding properties of metamaterials. Experimental studies with a metamaterial made of 'Swiss rolls' [72] have shown that the resulting metamaterial exhibits a high permeability, being capable of guiding magnetic flux, with potential applications in magnetic resonance imaging (MRI).

MI waves can be equally responsible for such guiding effects [7], [73], and have great potential in applications mainly on account of their versatility and simplicity of design, also helped by the ease with which they can be produced, the relatively simple mathematical description of their operation, and the vast frequency range (from the MHz to the THz region) in which they can operate [73]. Such waves may exist in one-, two- and three-dimensional lattices [63], and they exhibit all the relevant wave phenomena, such as refraction, reflection and diffraction [29]. Therefore, MIWs have the potential to be applied as a variety of near-field subwavelength manipulating devices, as proposed in [7], [62], [71], [73]–[80], such as waveguides, mirrors, Fabry-Perot resonators, tapers, reflectors, power dividers, directional couplers, phase shifters, delay lines and near-field lenses.

Stevens *et al*. [8], [9] explored the potential of MIWs to be applied as contactless near-field data transfer channels and subsequently showed that such channels can operate in both 1-D

MIWs (Fig. 2-9 (a)–(b)) [9] and 2-D MIWs (Fig. 2-9 (c)) [8] with good data capacities. It has been experimentally demonstrated that the 1-D coplanar MIW data transfer channel [9] can achieve a data capacity of ~60 Mbps (for an assumed input signal-to-noise ratio (SNR) of 10^4), and the 2-D MIW data transfer channel [8] can achieve a data capacity of ~305 Mbps (for an assumed SNR of 100). It was found that the data exchange within 2-D MIWs is not limited to the direct signal path [8], which implies that network flexibility and usability could be further improved by involving multiple terminal connections and allowing multipath data transfer channels.

Wireless power transfer (WPT) is an old research topic [81] that has generated much current research interest in the context of metamaterials. The original work described in [1] first demonstrated long-range power transfer with low radiated losses and 40~50% transfer efficiency via self-resonant strongly coupled coils. Since then a number of methods have been employed to extend the range of efficient power transfer, notably the use of passive, resonant relay coils to increase the oscillating magnetic flux at the receiving coil [82]–[86]. Alongside this there has been a surge in research interests in applying relay coils in near-field wireless power transfer applications, particularly for charging small electronic devices [87]–[90].

Stevens *et al*. [5] offered an insight into relay coil systems by understanding them as MI metamaterial waveguides and characterizing them by means of the properties of MI waves. A 1-D MIW metamaterial power surface has been proposed for efficient near-field power transfer, with further work on developing an optimal receiver to increase the transfer efficiency [10], [11]. Compared with conventional relay coil systems that use high-quality factors to achieve high power transfer efficiency, MIW metamaterial waveguides exhibit much higher coupling strengths, which gives them the potential to satisfy the needs of both efficient near-field power transfer and high data bus speeds at the same time.

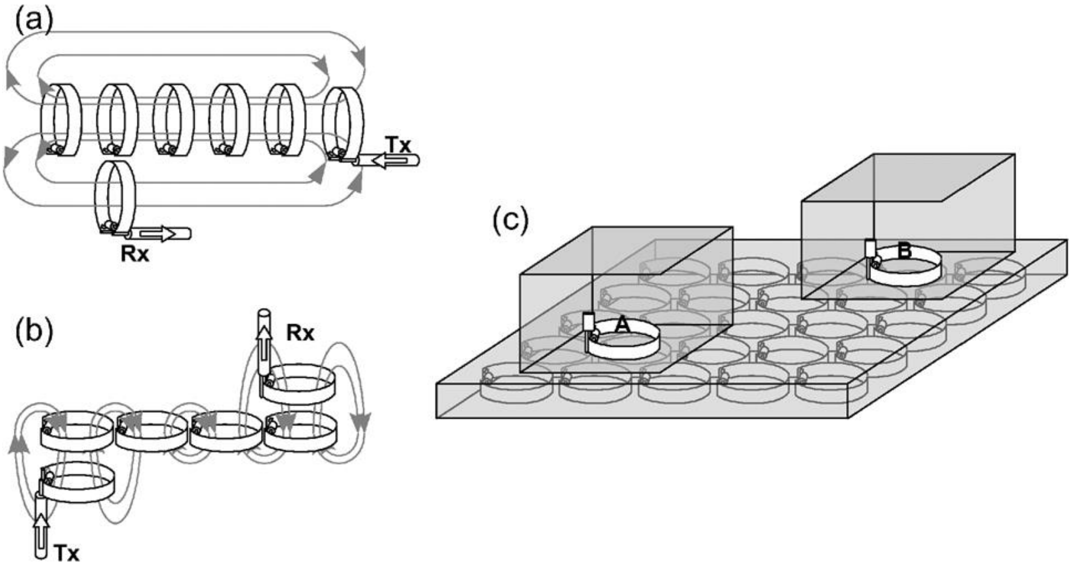

Fig. 2-9 *Configurations of a magneto-inductive wave-based contactless data channel based on (a) a 1-D coaxially coupled channel with plane-coupled terminals; (b) a 1-D coplanarly coupled channel with axial-coupled terminals; (c) a planar 2-D array with two terminal devices A and B, where A and B represent two mobile devices which are using the 2-D array to exchange data. This figure is taken from* [81].

Previous work in [9] proposed the idea that a metamaterial waveguide surface has the potential to be used as track-free data buses in electronic systems with the possibility for inter-chip communications if the silicon integrated circuits (ICs) in such systems are capable of launching and detecting MI and EI waves. It could also be applied in body area networking (BAN) applications, such as linking up patient monitors, saving alarms and headphones, through clothes embedded with such metamaterial waveguides.

CHAPTER 3

ONE-DIMENSIONAL CAPACITOR-CONNECTED GRIDS

The objective of this study is to build a more strongly coupled metamaterial waveguide with the aid of additional electric coupling, overcoming the limit of coupling strength in conventional, almost purely magnetically coupled, MIWs, and by this means produce more efficient contactless data and power transfer channels.

Significant effort has been devoted to enhance magnetic coupling strengths in MIWs, via adjusting inter-element separations and orientations [12], redesigning element shapes [13], introducing positional shifts between elements [14] and improving fabrication methods [15]. However, the maximum magnetic coupling strength can never exceed the limit of magnetic flux conservation.

With the attempt to overcome the limit of coupling strength in conventional MIWs, Stevens *et al*. [91] considered the ultimate limit of reducing the inter-element separations, in which the individual resonators have coalesced to form a coplanar 1-D ladder circuit called a CapGrid. A CapGrid structure does not lead to a large increase in mutual inductance and available bandwidth, compared with what can be readily achieved with conventional MIWs. However, this attempt to use an interlinked continuous structure to enhance coupling strength in metamaterial waveguides provides the basic inspiration for the following study.

This study considers a new variant of the metamaterial waveguide: the Capacitor-Connected Grid (CCG), as shown in Fig. 3-1 (a), which is a continuous circuit mesh formed by connecting coupling capacitors over the inter-element gaps between capacitively loaded metallic loops in traditional coplanar MIWs (Fig. 3-1 (b)). The aim of designing CCG structures is to build a more strongly coupled metamaterial waveguide by introducing additional electric coupling into conventional, purely magnetically coupled, MIWs.

In Section 3.1, the structure of the 1-D CCG will be investigated, and its equivalent quasi-static RLC circuit model will be developed. The circuit model will lead to the derivation of its dispersion equation and passband frequency bounds in Section 3.2. In Section 3.3, the experimental demonstration structure of a 1-D CCG will be given, along with its dimensional details. In Section 3.4, the structure's dispersion characteristics will be analysed, leading to a discussion of the coupling mechanism of the CCG in Section 3.5. In Section 3.6, a mixed coupling model will be derived based on the state-of-the-art and presented in comparison with previous work. This mixed coupling model will be verified and applied in the dispersion analysis of 1-D CCG structures in Section 3.7.

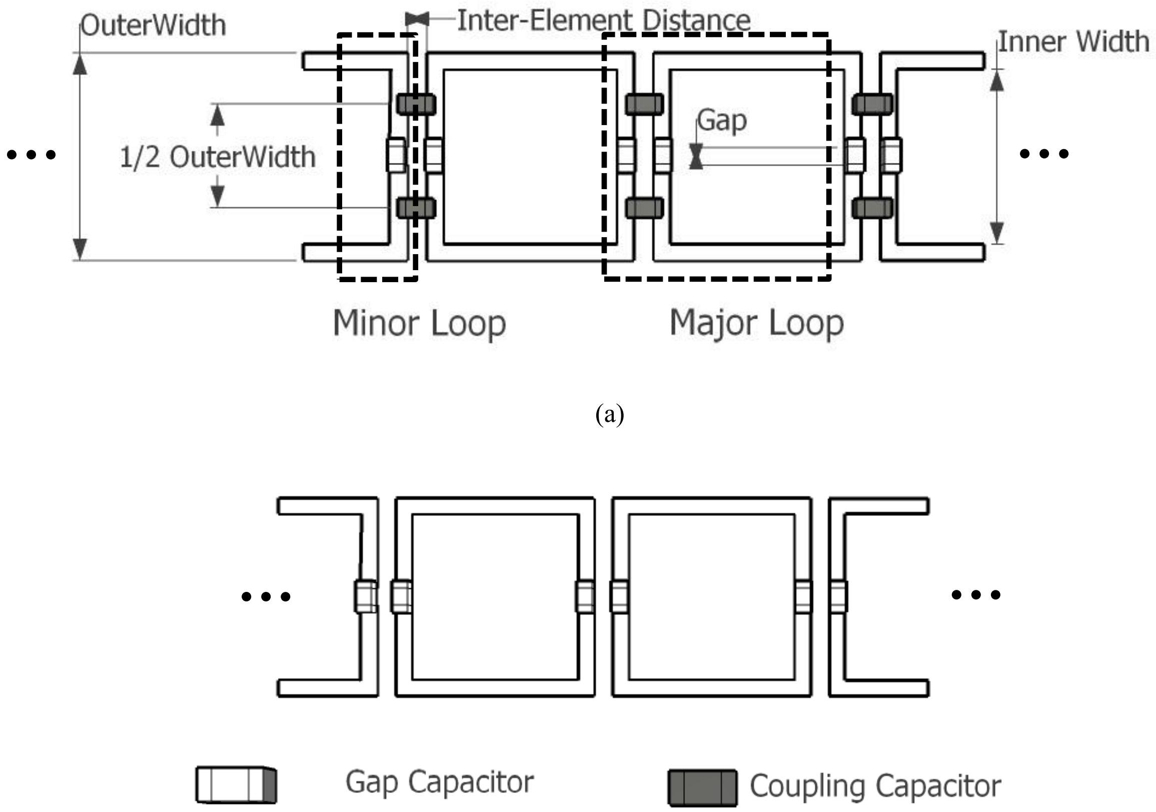

(a)

(b)

Fig. 3-1 *Structure of (a) adjacent resonators from 1-D CCGs; (b) adjacent resonators from conventional MIWs, which are made of metallic loops loaded with gap capacitors. In (a) additional coupling capacitors are connected over the inter-element gaps; gap capacitors are shared between newly formed minor loops and adjacent major loops, which are conventional MIW resonators.*

3.1 Circuit Model of 1-D CCGs

The structures of 1-D CCG waveguides are illustrated in Fig. 3-1 (a) to compare them with the structures of conventional MIW devices as shown in Fig. 3-1 (b). In this section, an analytical equivalent circuit model of the CCG will be built based on quasi-static circuit analysis.

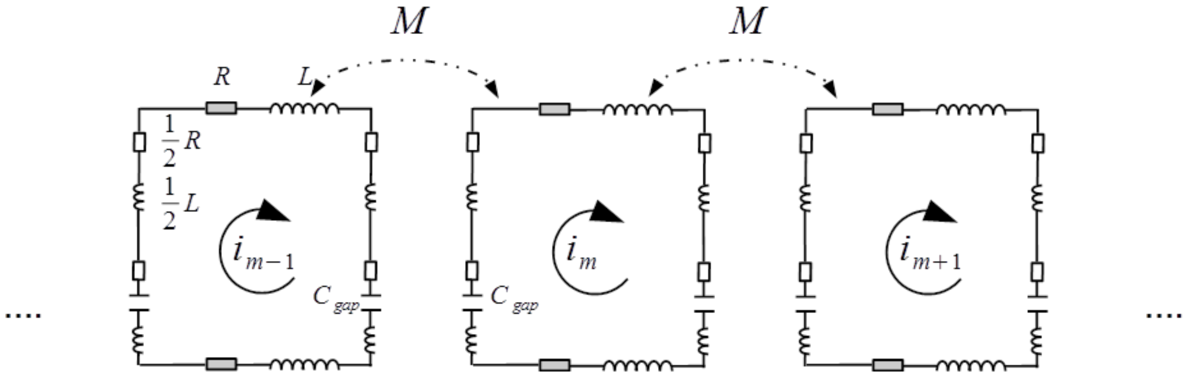

Fig. 3-2 *Circuit model of a coplanar 1-D MIW structure.*

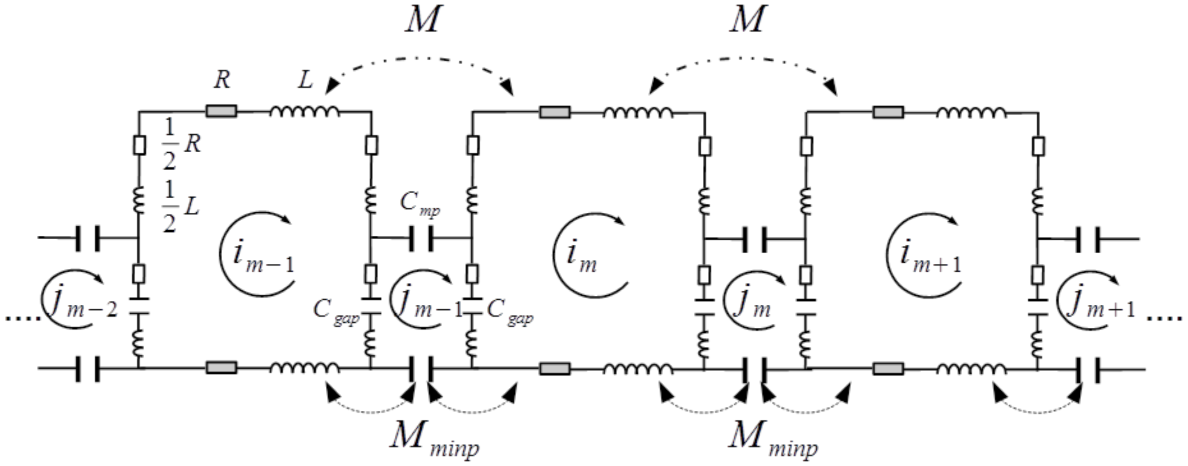

Fig. 3-3 *Circuit model of a coplanar 1-D CCG structure.*

Fig. 3-2 shows the circuit model of a 1-D MIW structure, which is made of electrically isolated, purely magnetically coupled, capacitively loaded metallic loops. Assuming that the resonant frequency of individual elements corresponds to a free-space wavelength much larger than the element size, the structure can be well described by a quasi-static approximation [92]. This approximation can also be applied when exploring wave propagation in CCG structures.

Fig. 3-3 presents the circuit model of a 1-D CCG structure, which can be considered as a continuous circuit mesh consisting of alternating *major loops* and *minor loops*. Major loops are the same kind of RLC resonant circuits as conventional MIW elements, which are interlinked by C_{mp}, i.e. coupling capacitors soldered over the inter-element gaps in a parallel configuration. Between adjacent major loops, there is not only magnetic coupling, in much the same way as in conventional coplanar 1-D MIWs, but also electric coupling with the aid of C_{mp}. Each major loop is loaded with two gap capacitors (C_{gap}), one over each of the two gaps on common branches with adjacent, newly formed, smaller RLC resonant circuits, which are referred to as minor loops. The soldered joints of the coupling capacitors are one quarter of the way from both the top and the bottom of the shared branches, so approximately only half of the inductance and resistance associated with one arm of the major loop is actually included in the minor loop.

Differing from conventional, almost purely magnetically coupled, MIWs, CCG waveguides incorporate both magnetic and electric coupling. The electric coupling between major loops is introduced by the coupling capacitance C_{mp}. There are two magnetic coupling terms, M and M_{minp}. The first term, M, describes magnetic coupling between adjacent major loops, while the second term, M_{minp}, describes magnetic coupling between a pair of adjacent major and minor loops.

Fig. 3-4 (a) and (b) shows simplified circuit models illustrating the coupling mechanisms corresponding to M and M_{minp}, respectively. The two magnetic coupling terms, M and M_{minp}, can be calculated independently, as shown in Section 3.3, and they contribute jointly to the overall magnetic coupling strength based on the principle of superposition. More specifically, when considering the $m+1^{th}$ major loop in Fig. 3-4 (a) and (b), the e.m.f. induced by M and M_{minp} can be summed up when applying Kirchhoff's Voltage Law to this loop, as shown in Section 3.2.

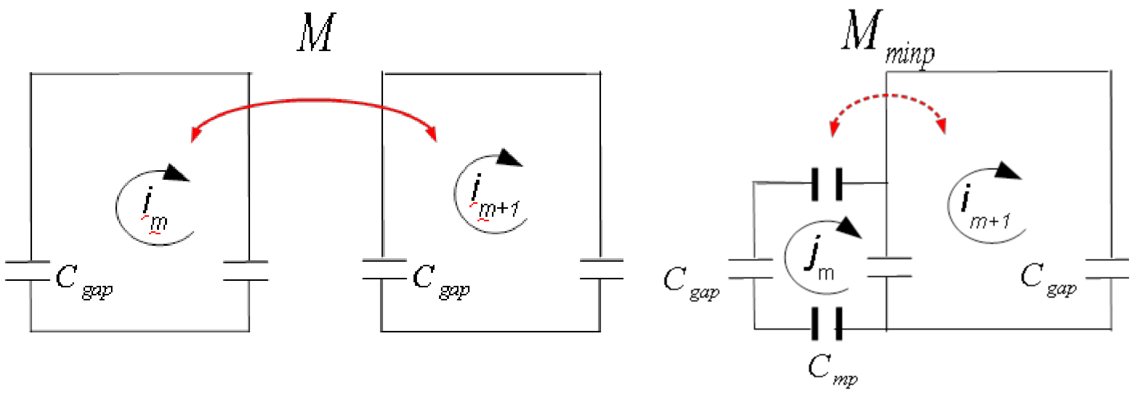

(a) (b)

Fig. 3-4 *Simplified circuit model illustrating the coupling mechanism of magnetic coupling between adjacent major loops in (a); magnetic coupling between adjacent major and minor loops in (b). The simplified model replaces the illustration of R and L with straight lines, while the parallel coupling capacitors* C_{mp} *and the gap capacitor* C_{gap} *are retained. The currents circulating in the major and minor loops are represented by i and j, respectively.*

3.2 Derivation of Dispersion Equation for CCGs

The dispersion equation of 1-D CCG structures can be derived by applying Kirchhoff's Voltage Law to the circuit model, as shown in Fig. 3-3. The circuit analysis of 1-D CCGs begins by considering the current circulating in the m^{th} major loop and the m^{th} minor loop. The nearest-neighbour approximation [63] is applied here for simplicity, in which only couplings with nearest neighbours are considered. The total potentials of the two elements are expressed by Eqs. (3.1) and (3.2):

$$\begin{gathered} Z_{maj} i_m + j\omega M(i_{m-1} + i_{m+1}) + j\omega M_{minp}(j_m + j_{m-1}) \\ - X_{share}(j_m + j_{m-1}) = 0 \end{gathered} \tag{3.1}$$

$$Z_{minp} j_m + j\omega M_{minp}(i_m + i_{m+1}) - X_{share}(i_m + i_{m+1}) = 0 \tag{3.2}$$

where Z_{maj} is the impedance of a major loop, and is given by $Z_{maj} = 4R + 4j\omega L + \frac{2}{j\omega C_{gap}}$, R and L are the resistance and the inductance, respectively, associated with each side of a major loop, ω is the angular frequency of wave propagation, X_{share} is the impedance of the common branch shared between adjacent major and minor loops, and is given by $X_{share} = \frac{R}{2} + \frac{j\omega L}{2} + \frac{1}{j\omega C_{gap}}$, Z_{minp} is the impedance of a minor loop, and is given by $Z_{minp} = R + j\omega L + \frac{2}{j\omega C_{gap}} + \frac{2}{j\omega C_{mp}}$, the current in the m^{th} major loop is given by i_m, while the current in the m^{th} minor loop is given by j_m; C_{gap}, C_{mp}, M and M_{minp} are as defined in Section 3.1.

In order to explore the response, one now assumes a wavelike current excitation of the form expressed by Eqs. (3.3) and (3.4):

$$i_m = I_0 e^{-\gamma m d} \tag{3.3}$$

$$j_m = J_0 e^{-\gamma m d} \tag{3.4}$$

where I_0 and J_0 are the current amplitudes at the first major loop and the first minor loop, respectively, d is the period of the structure, which is the distance between the centres of a pair of adjacent major loops; the propagation constant is expressed by Eq. (3.5):

$$\gamma = \alpha + j\beta \tag{3.5}$$

where α and β are, respectively, the attenuation constant and the wave number. Substituting Eqs. (3.3) and (3.4) into Eqs. (3.1) and (3.2), one can derive the dispersion equation Eq. (3.6):

$$cosh\,\gamma d = -\frac{Z_{maj} - \frac{2\left(j\omega M_{minp} - X_{share}\right)^2}{Z_{minp}}}{2(j\omega M - \frac{\left(j\omega M_{minp} - X_{share}\right)^2}{Z_{minp}})} \tag{3.6}$$

which can be transformed into the dispersion equation for conventional 1-D MIWs, which is $\cosh\gamma d = \frac{Z_{maj}}{-2j\omega M}$ [29], by eliminating all extra terms Z_{minp}, M_{minp} and X_{share}.

Finally, one can rewrite the dispersion relation Eq. (3.6) as a function of attenuation and wave number, as expressed by Eq. (3.7):

$$(\alpha + j\beta\,)d = \cosh^{-1} - \frac{Z_{maj} - \dfrac{2\big(j\omega M_{minp} - X_{share}\big)^2}{Z_{minp}}}{2\Big(j\omega M - \dfrac{\big(j\omega M_{minp} - X_{share}\big)^2}{Z_{minp}}\Big)} \tag{3.7}$$

The available bandwidth can be found by assuming a lossless propagation case $\alpha \to 0$, whereupon a cosh function becomes a cosine function, and one may inspect the limits where $|\cos(\beta d)| = 1$ [91], which gives the upper and lower bounds of the passbands as Eqs. (3.8)–(3.11):

$$f_{L1} = \frac{1}{2\pi}\sqrt{\frac{-b + \sqrt{b^2 - 4ac}}{2a}} \tag{3.8}$$

$$f_{L2} = \frac{1}{2\pi}\sqrt{\frac{1}{C_{gap}(2L - M)}} \tag{3.9}$$

$$f_{H1} = \frac{1}{2\pi}\sqrt{\frac{-b - \sqrt{b^2 - 4ac}}{2a}} \tag{3.10}$$

$$f_{H2} = \frac{1}{2\pi}\sqrt{\frac{2}{C_{gap}L} + \frac{2}{C_{mp}L}} \tag{3.11}$$

where the coefficients *a*, *b* and *c* are defined by Eqs. (3.12)–(3.14):

$$a = -\big(3L^2 + 2LM - 4{M_{minp}}^2 + 4M_{minp}L\big) \tag{3.12}$$

$$b = \frac{6L}{C_{gap}} + \frac{8L}{C_{mp}} + \frac{8M_{minp}}{C_{gap}} + \frac{4M}{C_{gap}} + \frac{4M}{C_{mp}} \tag{3.13}$$

$$c = -\frac{4}{C_{gap}C_{mp}} \tag{3.14}$$

A 1-D CCG structure is a continuous chain of inter-coupled alternating major and minor loops, and therefore can essentially be considered as a bi-atomic metamaterial structure [93] which displays two distinct passbands defined by Eqs. (3.8)–(3.11) as a direct consequence of bi-atomicity that is well known in solid-state physics [94].

The two passbands of CCGs, defined in Eqs. (3.8)–(3.11), are determined by L and C, which in turn determine the resonant frequency of CCGs and variables related to couplings, including M, M_{minp} and C_{mp}. Among them, only the parallel coupling capacitance C_{mp} can be readily varied by using capacitors of different values, while factors relating to magnetic coupling are fixed once the geometry of the loops is determined. Therefore, the dispersion behaviours and the coupling mechanism of CCG structures can be explored with different electric coupling strengths by varying the value of C_{mp}.

3.3 Demonstration Structure of 1-D CCGs

In order to characterize the dispersion behaviours of 1-D CCGs (Fig. 3-1 (a)), one can consider a simple demonstration structure, which is constructed by interlinking a chain of metallic loops (Fig. 3-1 (b)) by parallel coupling capacitors C_{mp} soldered across inter-element gaps. The metallic loops are constructed of fixed dimensions, as specified in Table 3-1.

Table 3-1 *Dimensions of metallic loops used to build the 1-D CCG demonstration structure*

Dimensions	**Length/mm**
Inner Width	8.000
Outer Width	9.500
Track Width	0.750
Gap Width	0.800
Inter-Width of Minor Loop	0.900
Copper Layer Thickness	0.035

The 1-D CCG demonstration structure can be well described by parameters calculated based on the dimensional information given in Table 3-1. A previous study [13] on equivalent-sized MIWs verified experimentally that the effective resistance and inductance of each metallic loop were 0.2 Ω and 20.48 nH, respectively, so the quarter resistance and inductance associated with each side of the loop are R = 0.05 Ω and L = 5.12 nH. The gap capacitor (C_{gap}) is chosen as 220 pF, while the value of the parallel coupling capacitance (C_{mp}) is open to change.

The mutual inductance, M and M_{minp}, can also be calculated independently using the integral of the vector potential along the closed path of one conductor from a current in another [92] as Eq. (3.15).

$$M_{12} = \frac{1}{I_2} \oint_1 A_2 \cdot dl_1 \tag{3.15}$$

where the vector potential A_2 generated by a current I_2 flowing in the 2^{nd} conductor is integrated along the closed path of the 1^{st} conductor, and gives the mutual inductance between the 1^{st} and the 2^{nd} conductor M_{12}.

There is an implicit condition behind the use of Eq. (3.15): the first and second conductors are not connected. However, as illustrated in Fig. 3-4 (b), there is a shared conductor between adjacent major and minor loops. Therefore, when applying this approach to the calculation of M_{minp}, one may assume that the contribution from the shared branch between adjacent major and minor loops can be neglected, in the sense that the circulating currents in the two adjacent loops cancel each other, so the net circulating current in the shared branch becomes nearly zero. This assumption was first proposed and verified by Stevens [91] in the case of a similar structure, the ladder-like CapGrid waveguide.

The calculation result shows that $M = -1.19$ nH and $M_{minp} = 0.127$ nH. It is worth noting that M_{minp} has a positive sign, which is opposite to the negative sign of M. The reason for the occurrence of positive magnetic coupling between coalesced loops has been discussed in [91] and can be attributed to the removal of the major negative contribution to the overall mutual inductance integral as the net circulating current in the shared branch is assumed to be nearly zero.

One can see that the value of M_{minp} is negligible relative to M. This is as expected from careful inspection of the geometries of major and minor loops. Therefore, M_{minp} is not considered in the following discussion.

The aforementioned parameters of the demonstration structure are summarized in Table 3-2.

Table 3-2 *Inductive, resistive and capacitive parameters of the 1-D CCG demonstration structure*

Parameters	**Values**
M	–1.19 nH
M_{minp} (negligible)	0.127 nH
R	0.05 Ω
L	5.12 nH
C_{gap}	220 pF

3.4 Dispersion Characteristics Analysis

The dispersion characteristics of 1-D CCG structures can be explored by varying the coupling capacitance C_{mp} from 1 pF up to 1 μF, which explores a large range of electric coupling strengths.

One can first consider how the frequency bounds of the two passbands defined by Eqs. (3.8)–(3.11) change with varying C_{mp}, as presented in Fig. 3-5. Among the two passbands, the lower one has a frequency bound f_{L2} given by Eq. (3.9), which approximately equals the resonant frequency of the major loops $f_{maj} = \frac{1}{2\pi}\sqrt{\frac{1}{2C_{gap}L}}$ when M is much smaller than L; the upper passband has a frequency bound f_{H2} given by Eq. (3.11), which approximately equals the resonant frequency of the minor loops $f_{min} = \frac{1}{2\pi}\sqrt{\frac{2}{C_{gap}L}}$ when C_{mp} takes a much larger value than C_{gap}.

Fig. 3-5 shows the frequency boundaries of the two passbands of the CCG structure defined in Table 3-2. It shows that the available bandwidth of the lower passband keeps expanding as C_{mp} increases after the intersection between f_{L1} and f_{L2}, while the two frequency bounds of the upper passband tend to converge towards the resonant frequency f_{min}, and so cannot reflect much of the change in electric coupling. The largest fractional bandwidth ($FBW = \frac{2(f_{L1} - f_{L2})}{f_{L1} + f_{L2}}$) achieved by the lower passband is up to 192.4% when C_{mp} = 1 μF, which closely approaches the 200% bandwidth limit and exceeds the 20% requirement of an ultra-wideband (UWB) channel [95] by a factor of 9.6; however, the FBW of the upper passband has never exceeded the 20% value. Therefore, the following discussion concentrates only on the performance of the lower passband, exploring how it reacts depending on parallel coupling capacitance C_{mp}.

Before investigating the performance of the lower passband, it is worth having a brief discussion about the upper passband. The frequency boundaries for the upper passband at $C_{mp} = 1$ pF is from 3.16 GHz to 3.64 GHz. The free space wavelength ($\lambda_0 = \frac{c}{f}$) corresponding to the upper boundary is 82.4 mm. The lattice period of the demonstration CCG structure is 10.4mm (include a major loop and a minor loop) as given in Table 3-1. In this case, the quasi-static approximation made in the circuit analysis breaks down due to the retardation effect [67]. The radiation loss of the upper passband is higher than the lower passband, because the radiation loss increases as frequency increases based on loop antenna theory [29].

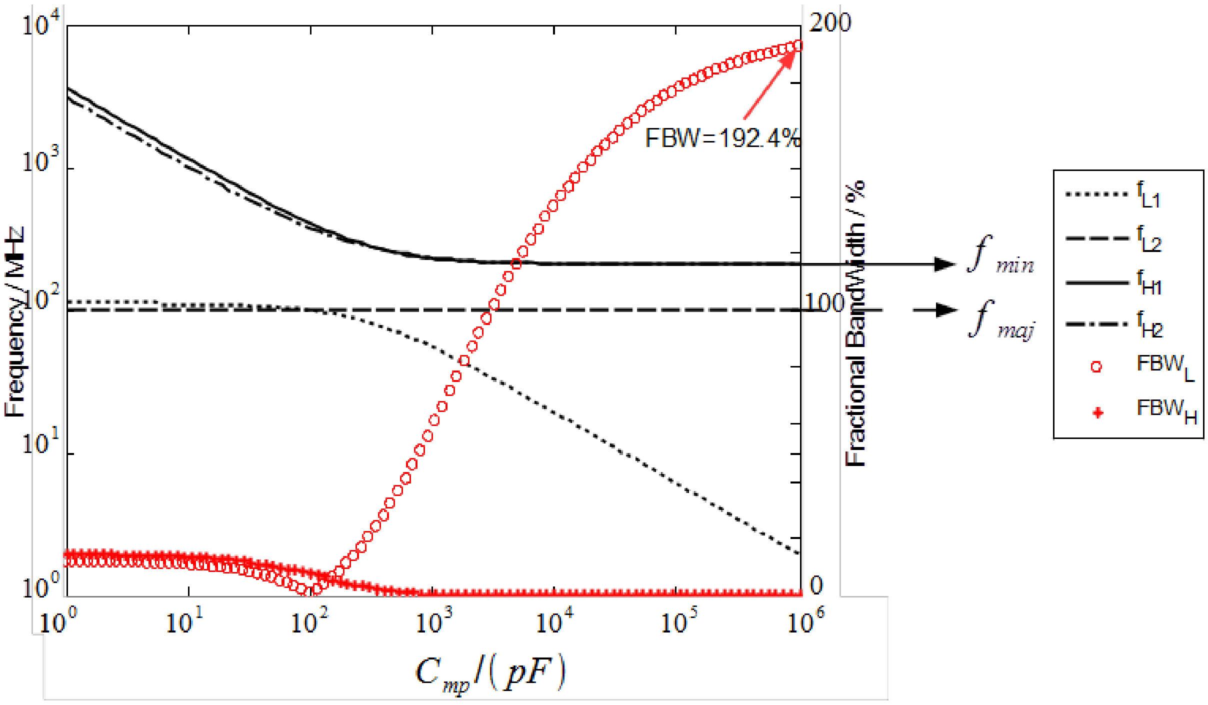

Fig. 3-5 *Frequency bounds and FBWs of the upper and lower passbands of 1-D CCG structures with* C_{mp} *ranging from 1 pF to 1 μF, with the resonant frequencies of the major loop and the minor loop marked in the figure; both axes are plotted on logarithmic scales.*

When considering the lower passband, one can see that the ordering between f_{L1} and f_{L2} changes when C_{mp} goes above a critical value, as shown in Fig. 3-5. The value of C_{mp} at which f_{L1} and f_{L2} intersect, noted as C_{cross}, can be found by equating f_{L1} (Eq. (3.8)) and f_{L2} (Eq. (3.9)), as expressed in Eq. (3.16). For 1-D CCG structures with C_{mp} < C_{cross}, f_{L1} >f_{L2}, while for C_{mp} > C_{cross}, f_{L1} <f_{L2}. For completeness, Eq. (3.16) contains the term M_{minp} which is proven to be negligible in this study.

$$C_{cross} = \frac{(-8C_{gap})(2LM - M^2)}{9L^2 + 12LM_{minp} - 8M_{minp}M + 4M_{minp}^2 - 4M^2} \tag{3.16}$$

Given that M_{minp} is proven to be negligible in Section 3.3, the value of C_{cross} of the demonstration structure, based on the parameters given in Table 3-2, is found to be $C_{cross} =$ 99.42 pF.

One can now consider how the components of the propagation constant, i.e. the attenuation constant α and the wave number β, change with the parallel coupling capacitance C_{mp} under the lossless propagation assumption, as shown in Fig. 3-6 (a) and (b), respectively. The frequency bounds of the lower passbands f_{L1} and f_{L2} calculated from Eqs. (3.8) and (3.9) are plotted as the blue lines.

In Fig. 3-6, one can see that C_{cross} delimits the two different propagation regions. In the region where $C_{mp} < C_{cross}$, the available bandwidth of the lower passband keeps shrinking as C_{mp} increases. At the crossover point, where $C_{mp} = C_{cross}$, there is a no propagation along the waveguide as the passband reduces to zero when $f_{L1} = f_{L2}$. In the region where $C_{mp} > C_{cross}$, the available bandwidth of the lower passband becomes increasingly wider as C_{mp} increases.

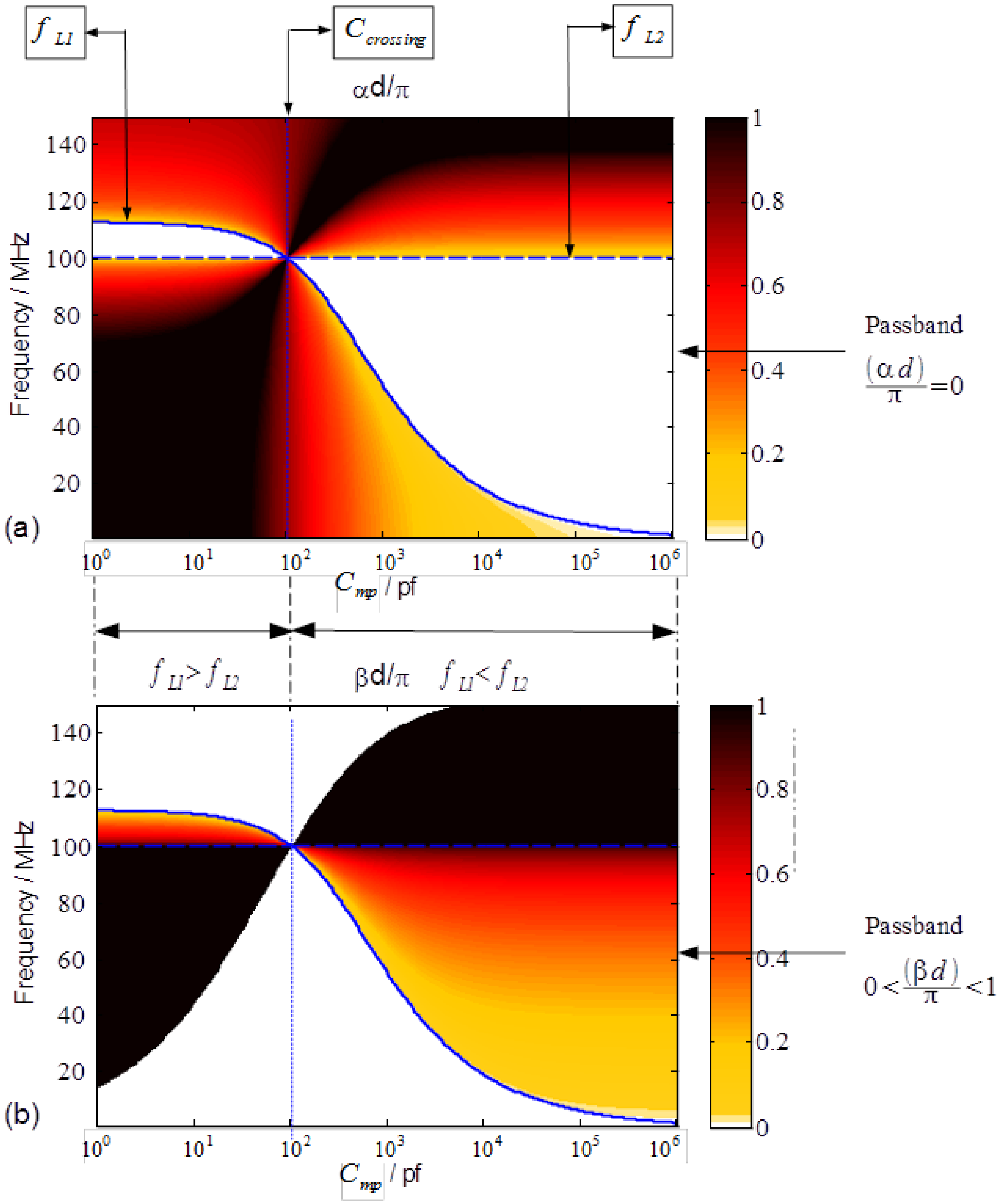

Fig. 3-6 *Dispersion relationship of CCGs with the lossless assumption (R = 0; other parameters are given in Table 3-2);* C_{mp} *ranges from 1 pF to 1 μF on the logarithmic scale; variation of (a) the wave number β and (b) the attenuation constant α as* C_{mp} *increases.*

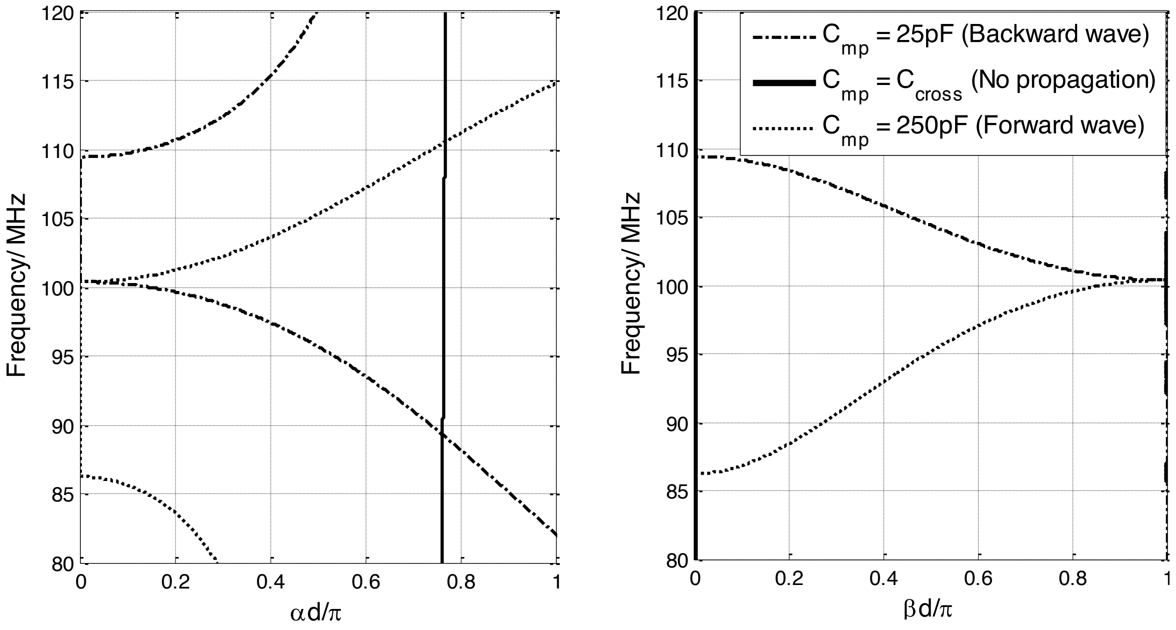

(a) (b)

Fig. 3-7 (a) Attenuation constant α and (b) wave number β calculated with $C_{mp} = 25$ pF, $C_{mp} = C_{cross} = 99.42$ pF *and* $C_{mp} = 250$ pF *under the lossless assumption R = 0.*

To better illustrate the dispersion characteristics in the two distinct propagation regions and at the intersection under the lossless assumption, Fig. 3-7 shows the dispersion curves corresponding to three different values of C_{mp}, among which C_{mp}= 25 pF is taken from the forward wave propagation mode; C_{mp} = 250 pF is taken from the forward wave propagation mode; and $C_{mp} = C_{cross}$ = 99.42 pF is taken exactly at the intersection. It shows that the 1-D CCG waveguide built with C_{mp} = 25 pF supports backward wave propagation, of which the group velocity ($v_g = \frac{d\omega}{d\beta}$) and phase velocity ($v_p = \frac{\omega}{\beta}$) are in opposite directions; the 1-D CCG waveguide built with C_{mp}= 250 pF supports forward wave propagation, of which v_g and v_p are in the same direction, and there is no wave solution at the intersection where $C_{mp} = C_{cross} = 99.42$ pF.

One can now consider how α and β change with the parallel coupling capacitance C_{mp} when taking resistance R = 0.2 Ω into account, as shown in Fig. 3-8 (a) and (b), respectively.

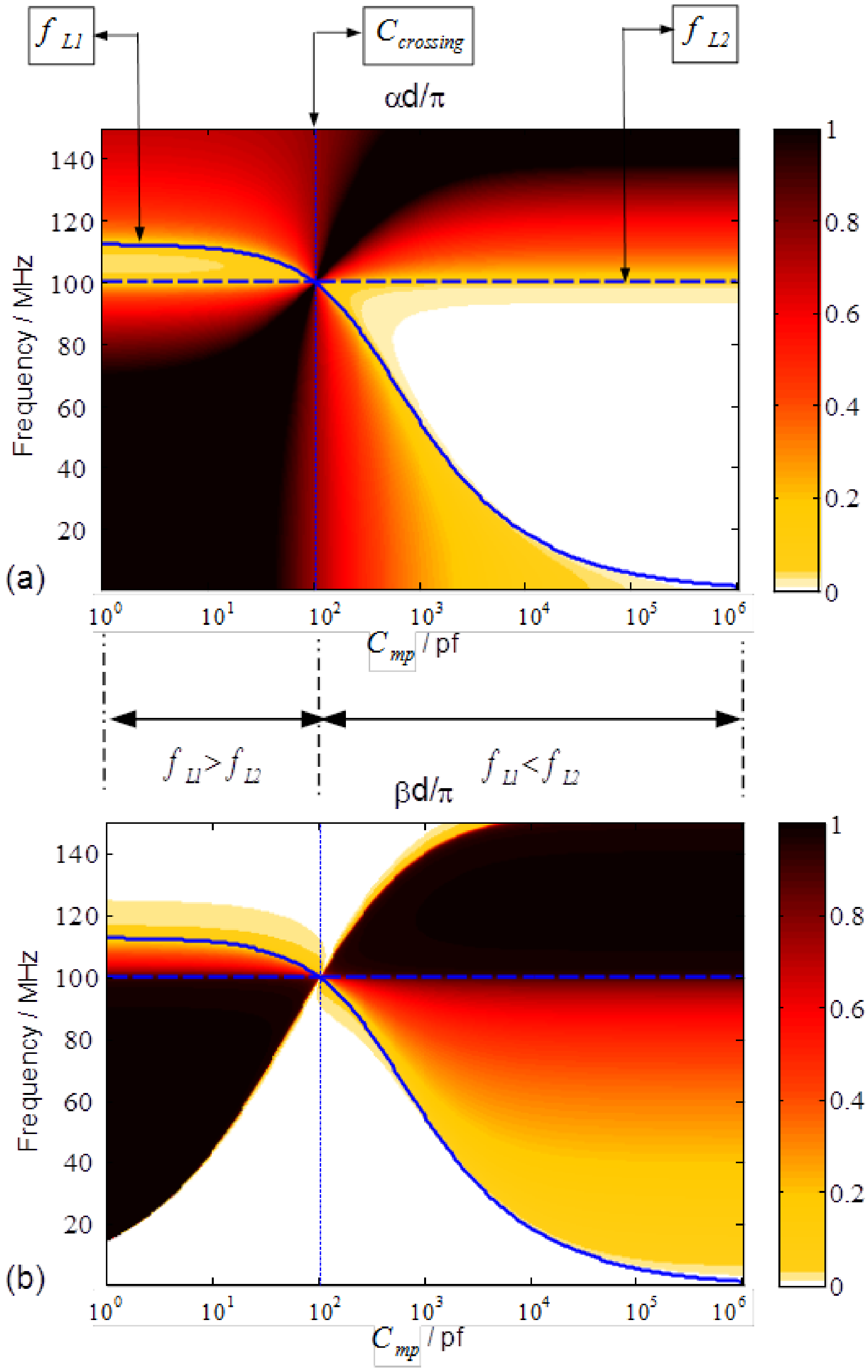

Fig. 3-8 Dispersion relationship of CCGs, with parameters R = 0.2 Ω and other parameters as given in Table 3-2, and C_{mp} ranging from 1 pF to 1 µF on the logarithmic scale; variation in (a) the wave number β and (b) the attenuation constant α as C_{mp} increases

.

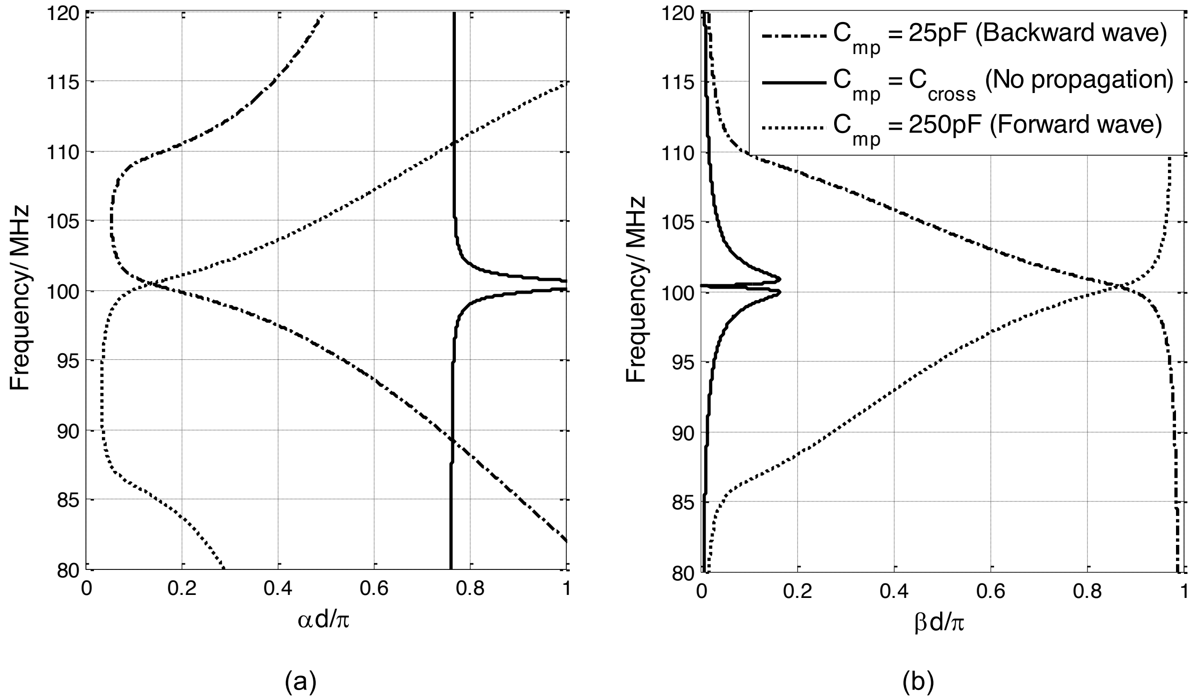

Fig. 3-9 *(a) Attenuation constant α and (b) wave number β calculated with* $C_{mp} = 25\,pF,\ C_{mp} = C_{cross} = 99.42\,pF$ *and* $C_{mp} = 250\,pF$ *when R = 0.2 Ω.*

Comparing this to the lossless case shown in Fig. 3-6, the values of α and β plotted in Fig. 3-8 are smoothed around the frequency bounds defined by f_{L1} and f_{L2}. One can see that the attenuation in the passband is no longer zero, and the passband presented by $0 < \frac{\beta d}{\pi} < 1$ spreads outside of the original boundaries of the lower passband in the lossless case.

The corresponding dispersion curves with $R = 0.2\ \Omega$ are plotted in Fig. 3-9 with the same C_{mp} values (25 pF, 250 pF and 99.42 pF) as used in Fig. 3-7. Compared with the lossless case in Fig. 3-7, the attenuation constant α is no longer zero over the passband of both forward and backward wave propagation, and gradually increases at the edges of the passband, while, correspondingly, v_g gradually decreasing at the edges. At the intersection where $C_{mp} = C_{cross}$, instead of seeing a constant high-valued α in the lossless case, there is a spike in the value of α, indicating maximal attenuation is achieved at the frequency where $f_{L1} = f_{L2}$. Instead of seeing no wave propagation in the lossless case, there is a lip-shaped β curve around the frequency where $f_{L1} = f_{L2}$, presenting a backward wave solution at the lower lip side and a forward wave solution at the upper lip side. Instead of cancelling each other out in the lossless situation, the forward wave and backward solutions coexist and interfere with each other for a restricted range of β. This can be considered as evidence for competition between positive and negative coupling, with negative coupling marginally winning at the lower lip side and positive coupling marginally winning at the upper lip side. Due to the existence of very high attenuation, the propagation around this lip-shaped area is not very useful for any applications.

When considering CCG waveguides as potential candidates for data-carrying devices it is important to consider the effects of dispersion on modulated signals. Using the dimensional parameters as given in Table 3-2, one can calculate the group velocity dispersion for 1-D CCG waveguides built with four different values of C_{mp} and for an equivalent-sized 1-D coplanar MIW device of identical period. One can choose C_{mp}= 50 pF from the backward wave propagation mode ($C_{mp} < C_{cross}$), and the other three C_{mp}= 1 nF, 10 nF and 1 μF from the forward wave propagation mode ($C_{mp} > C_{cross}$). Fig. 3-10 shows the group velocity dispersion and attenuations of the four 1-D CCG cases in comparison with the equivalent-sized 1-D coplanar MIWs.

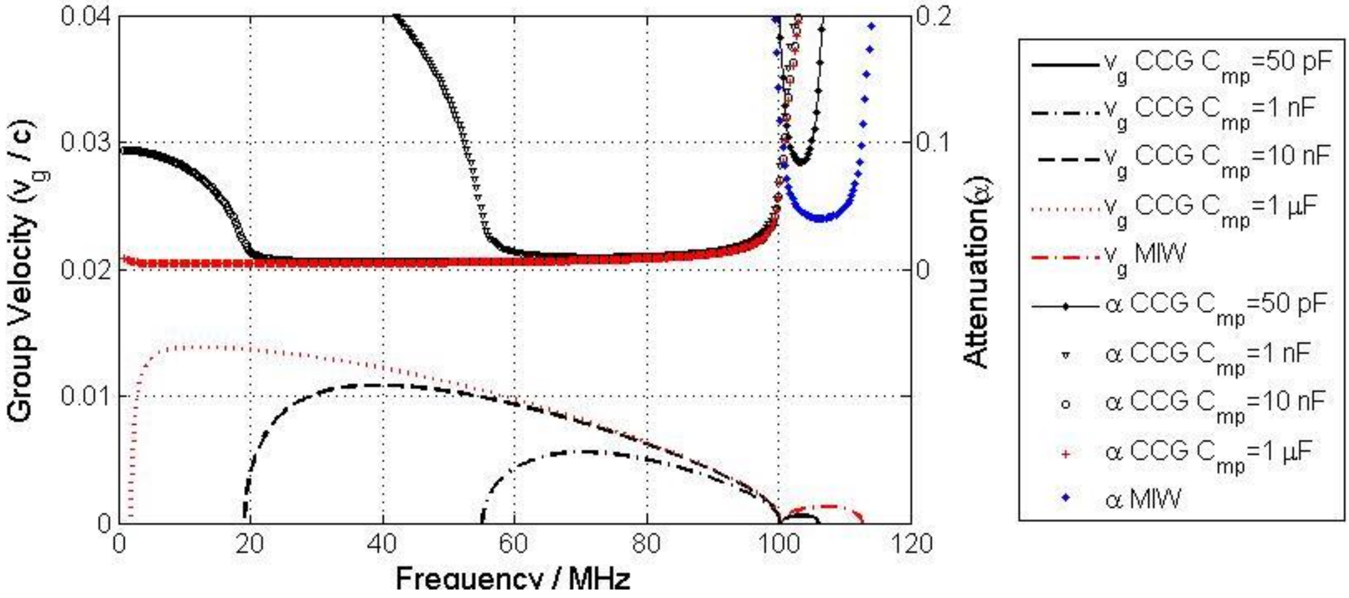

Fig. 3-10 *Comparison of the group velocity dispersion and attenuation for 1-D CCG structures built with four different values of* C_{mp} *(50 pF, 1 nF, 10 nF and 1 µF) and an equivalent-sized coplanar 1-D MIW.*

Table 3-3 shows the peak group velocity v_{gpeak} relative to the speed of light c and the bandwidth over a less dispersive frequency range defined by $1 \geq \frac{v_g}{v_{gpeak}} \geq 0.9$ for the four CCG cases and the equivalent-sized MIW illustrated in Fig. 3-10.

Table 3-3 *Comparison of the group velocity dispersion relative to the speed of light c and the bandwidth over a less dispersive frequency range defined by* $1 \geq \frac{v_g}{v_{gpeak}} \geq 0.9$ *for a 1-D CCG waveguide built with* C_{mp}*= 50 pF, 1 nF, 10 nF and 1 µF and an equivalent-sized MIW as given in Table 3-2*

C_{mp}	**Peak Group Velocity (v_{gpeak}/c)**	**Bandwidth with $1 \geq \frac{v_g}{v_{gpeak}} \geq 0.9$ (MHz)**
C_{mp} = 50 pF	0.0006	2.4
C_{mp} = 1 nF	0.0056	14.67
C_{mp} = 10 nF	0.0109	28.89
C_{mp} = 1 µF	0.0138	34.92
Equivalent-sized MIW	0.0014	4.6

***Table 3-4** Comparison of the minimum attenuation and bandwidth defined by the –3 dB half power point for a 1-D CCG waveguide built with C_{mp}= 50 pF, 1 nF, 10 nF and 1 μF and an equivalent-sized MIW as given in Table 3-2.*

C_{mp}	**Minimum Attenuation (α_{min})**	**–3 dB Bandwidth/MHz**
C_{mp} = 50 pF	0.0839	5.7
C_{mp} = 1 nF	0.0103	38.40
C_{mp} = 10 nF	0.0055	66.84
C_{mp} = 1 μF	0.0044	83.22
Equivalent-sized MIW	0.0400	11.2

Table 3-4 shows the minimum attenuation values $\alpha_{\min}$ and bandwidth defined by the –3 dB half power points for the four CCG cases and the equivalent-sized MIW illustrated in Fig. 3-10.

Compared with equivalent-sized MIW devices, a 1-D CCG waveguide with $C_{mp} < C_{cross}$ has a narrower bandwidth, lower peak group velocity and a higher minimum attenuation. When the value of C_{mp} exceeds the value at the intersection C_{cross}, the bandwidth and peak group velocity of the 1-D CCG waveguide increases, and the minimum attenuation becomes lower as C_{mp} increases. The bandwidth defined over the range $1 \geq \frac{v_g}{v_{gpeak}} \geq 0.9$ and the −3 dB bandwidth expands as C_{mp} increases. The peak group velocity of the 1-D CCG waveguide with C_{mp} = 1 μF is nearly ten times larger than an equivalent-sized MIW device, and the minimum attenuation of this 1-D CCG waveguide is only one tenth of the loss of the equivalent-sized MIW. Such dispersion behaviour offers 1-D CCGs significant potential in terms of data capacity and speed, but at the expense of somewhat greater dispersion and fuller band group delay. 1-D CCG waveguides have the potential to offer very large bandwidths, such as that with C_{mp} = 1 μF, which gives 192.4% FBW, as shown in Fig. 3-5, implying that channelization can be used in order to get several sub-channels with less dispersion and group delay.

3.5 Coupling Mechanism of 1-D CCGs

There are three different sources of coupling that coexist and interfere with each other in 1-D CCG structures: (i) negative magnetic coupling between adjacent major loops in much the same way as in a purely magnetic MIW, (ii) magnetic coupling between a pair of adjacent major and minor loops, which has been proved to be positive [91], and (iii) electric coupling between major loops introduced by C_{mp}.

M_{minp} is proven to be negligible relative to M in Section 3.3; however for completeness, the role it plays in the coupling mechanism of CCG waveguides will still be addressed in the following discussion.

A simplified circuit model as shown in Fig. 3-11 is used to illustrate the interaction between the three types of coupling in 1-D CCG structures. This model interprets 1-D CCG structures as bi-atomic metamaterials [93], showing two adjacent CCG elements (the m^{th} and the $m+1^{th}$ elements), each of which consists of two distinct atoms – a major loop and a minor loop.

In this model, ε_{maj} represents the e.m.f. induced in the $m+1^{th}$ major loop through its negative magnetic coupling with the m^{th} major loop, and can be expressed as Eq. (3.17), where i_m is the circulating current in the m^{th} major loop:

$$\varepsilon_{maj} = j\omega M i_m \tag{3.17}$$

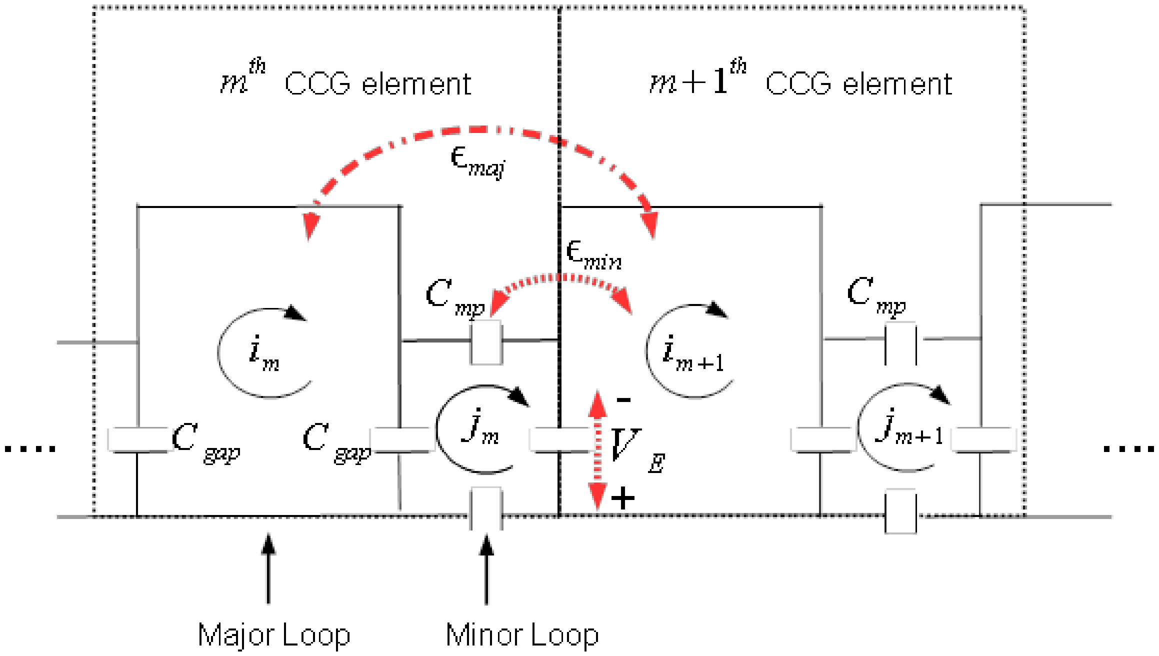

Fig. 3-11 *The bi-atomic circuit model is simplified from Fig. 3-3 by only showing the* m^{th} *and* $m+1^{th}$ *CCG elements: each element consists of a major loop and a minor loop, and R and L are replaced in the illustration by straight lines. Only the parallel coupling capacitors* C_{mp} *and the gap capacitor* C_{gap} *are kept to represent the source of electric coupling. The voltage reference direction of this model is marked in the figure.*

The e.m.f. induced in the $m+1^{th}$ major loop through its positive magnetic coupling with the m^{th} minor loop is represented by ε_{min}, and can be expressed as Eq. (3.18), where j_m is the circulating current in the m^{th} minor loop:

$$\varepsilon_{min} = j\omega M_{minp} j_m \tag{3.18}$$

V_E is the voltage passed to the $m+1^{th}$ major loop through its electric coupling with the m^{th} major loop, and can be expressed as Eq. (3.19):

$$V_E = -\frac{j_m}{j\omega C_{gap}} \tag{3.19}$$

The coupling mechanism of 1-D CCG structures can be expressed as Eqs. (3.20) and (3.21):

$$V_{total} = \varepsilon_M + V_E \tag{3.20}$$

$$\varepsilon_M = \varepsilon_{maj} + \varepsilon_{min} \tag{3.21}$$

where the total voltage induced in the $m + 1^{th}$ major loop is denoted by V_{total}, which is contributed by two components, a magnetic one, ε_M, and an electric one, V_E. The total e.m.f. induced by magnetic coupling is represented by ε_M, which is the sum of ε_{maj} and ε_{min}.

Assuming that M_{minp} is negligible, as verified in Table 3-2, one can simplify the expression for the total coupling-induced e.m.f. to Eq. (3.22):

$$V_{total} = \varepsilon_M + V_E = \left(j\omega M i_m - \frac{j_m}{j\omega C_{gap}} \right) \tag{3.22}$$

The magnetic and electric coupling both may take either positive or negative signs, and therefore the two may reinforce or counteract each other [59], [16]. Section 3.4 discusses the competition between positive and negative coupling in a 1-D CCG waveguide. The magnetic coupling of a CCG waveguide was proven to be negative in Section 3.3, so one knows that its electric coupling is positive.

The coupling mechanism of CCG structures can be described as the competition between the negative magnetic coupling between adjacent major loops and the positive electric coupling introduced by the parallel coupling capacitors C_{mp}. The crossover point appears when the positive and negative coupling contributors exactly cancel each other, which can be expressed as Eq. (3.23):

$$\left| -\frac{j_m}{j\omega C_{gap}} \right| = |j\omega M i_m| \tag{3.23}$$

There are two distinct propagation modes, which result in completely different dispersion behaviours. A negative magnetic coupling-dominated CCG structure, built with $C_{mp} < C_{cross}$, supports the backward MI wave propagation mode, in much the same way that a purely magnetic MIW does. A positive electric coupling-dominated CCG structure, built with $C_{mp} > C_{cross}$, on the other hand supports the forward EI wave propagation mode. Positive electric and negative magnetic coupling exactly cancel each other when a 1-D CCG structure is built with coupling capacitors $C_{mp} = C_{cross}$.

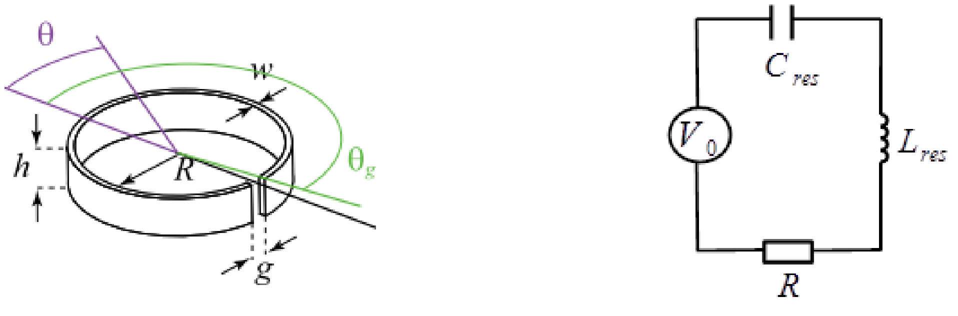

(a)

(b)

Fig. 3-12 *(a) Single split ring resonator; (b) equivalent circuit model for a single split ring, where* L_{res} *and* C_{res} *are the resonance inductance and capacitance, respectively, and* R_0 *is the resistance.*

3.6 The Mixed coupling model

The next step in this study is to find a method for calculating inter-element mixed coupling coefficients for arbitrarily configured CCG waveguides. By separately evaluating the electric and magnetic contributions to the mixed coupling coefficient, one is able to readily adapt the design of many mixed coupling waveguides to different requirements.

There is a rich literature [16] deriving an analytical model to work out the mixed coupling coefficient between arbitrarily positioned and oriented split-ring resonators. A brief review of these prior studies is given here before adjusting this model to CCG structures.

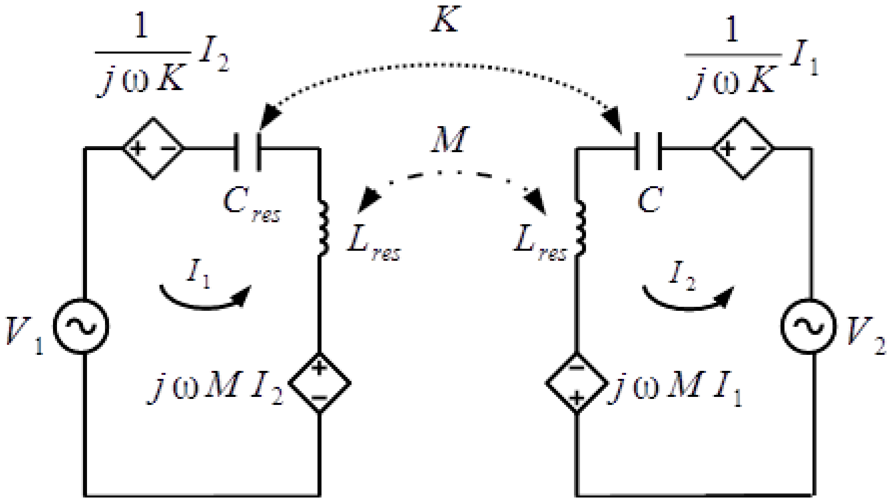

Fig. 3-13 *Equivalent circuit model for a pair of split metal rings with both magnetic and electric coupling, with mutual capacitance K and mutual inductance M assumed.*

The structure of the single split metal ring used in [16] is shown in Fig. 3-12 (a), where R is the inner radius, w is the wall thickness, h is the wall height, and g is the gap width; its corresponding equivalent RLC circuit model is shown in Fig. 3-12 (b). The resonant frequency of a single split ring is $\omega_0 = \frac{1}{\sqrt{L_{res}C_{res}}}$, where L_{res} is the resonance inductance and C_{res} is the resonance capacitance.

The equivalent circuit model for a pair of coupled split metal rings with mutual inductance M and mutual capacitance K is shown in Fig. 3-13, under the lossless assumption where the resistive term R is eliminated for simplicity.

When applying Kirchhoff's Voltage Law to the pair of coupled split rings in Fig. 2-12, the impedance matrix can be derived and expressed as Eq. (3.24):

$$\begin{bmatrix} V_1 \\ V_2 \end{bmatrix} = \begin{bmatrix} Z_0 & Z_m \\ Z_m & Z_0 \end{bmatrix} \cdot \begin{bmatrix} I_1 \\ I_2 \end{bmatrix} \tag{3.24}$$

where Z_0 is the self-impedance of a single ring as expressed by Eq. (3.25) and Z_m is the mutual impedance term as expressed by Eq. (3.26):

$$Z_0 = j\omega L_{res} + \frac{1}{j\omega C_{res}} \tag{3.25}$$

$$Z_m = j\omega M + \frac{1}{j\omega K} \tag{3.26}$$

The total coupling coefficient k_{total} is defined in Eq. (3.27).

$$k_{total} = k_m - k_e \frac{{\omega_0}^2}{\omega^2} \tag{3.27}$$

where the magnetic coupling coefficient k_m and the electric coupling coefficient k_e are defined as Eq. (3.28) and Eq. (3.29).

$$k_m = \frac{2M}{L_{res}} \tag{3.28}$$

$$k_e = \frac{2C_{res}}{K} \tag{3.29}$$

If the frequencies of interest are near enough to ω_0 such that $\frac{\omega_0}{\omega} \approx 1$, one can omit the term $\frac{\omega_0}{\omega}$ in Eq. (3.27) and have a simplified expression of the total coupling coefficient as Eq. (3.30)

$$k_{total} = k_m - k_e \tag{3.30}$$

The approximate values of the resonance capacitance C_{res} and the resonance inductance L_{res} were calculated as Eqs. (3.31) and (3.32), for which all geometric variables were given in Fig. 3-12 (a).

The definition of magnetic coupling in Eq. (3.28) is consistent with the one defined by Eq. (2.3). The only difference is that the self-inductance L_{self} in Eq. (2.3) is renamed as L_{res} in Eq. (3.28) in order to keep consistency with the naming convention of C_{res}.

The definition of electric coupling in Eq. (3.29) is consistent with the one defined by Eq. (2.6). The consistency will be proved by the later discussed adjusted model.

$$C_{res} = \varepsilon_0[\frac{(w+g)(h+g)}{g} + \frac{2(h+w)}{\pi} ln\frac{4R}{g}] \tag{3.31}$$

$$L_{res} = \mu_0 R(ln\frac{8R}{h+w} - \frac{1}{2}) \tag{3.32}$$

The values of the mutual capacitance K and the mutual inductance M are mainly determined by the configuration and the relative orientation of the two split rings. In the absence of retardation, K and M can be calculated by integrating over the perimeter of the ring, as Eqs. (3.33) and (3.34), respectively:

$$K^{-1} = \frac{1}{4\pi\varepsilon_0} \iint \frac{\rho_{n1}(\vec{r_1}) \cdot \rho_{n2}(\vec{r_2})}{|\vec{r_1} - \vec{r_2}|} ds_1 ds_2 \tag{3.33}$$

$$M = \frac{\mu_0}{4\pi} \iint \frac{\overrightarrow{I_{n1}}(\vec{r_1}) \cdot \overrightarrow{I_{n2}}(\vec{r_2})}{|\vec{r_1} - \vec{r_2}|} ds_1 ds_2 \tag{3.34}$$

where ε_0 is the free-space permittivity, μ_0 is the free-space permeability, ρ_{nl} is the normalized line charges of the l^{th} ring, $\overrightarrow{I_{nl}}$ is the normalized filament current of the l^{th} ring, $\vec{r_l}$ is the position vector of the l^{th} ring, and ds_l is the line element along the filament of the l^{th} ring.

This model calculates the four parameters C_{res}, L_{res}, K and M based on the geometry of the split rings and therefore allows calculation of the inter-element coupling coefficients k_m, k_e and k_{total} for arbitrarily positioned and oriented split rings.

In order to apply this model to CCG structures, one should first analyse the difference between split-ring structures and CCG structures:

(1) The resonance capacitance C_{res} and the mutual capacitance K are calculated based on the geometry of split-ring structures in [16]. However, in a CCG structure, these two

terms are determined by the passive components used in the circuit. This geometry-based approach can no longer be applied to the study of CCG structures.

(2) The model described in [16] calculates the resonance capacitance C_{res} of split-ring structures for one isolated split ring. In fact, the value of C_{res} of a ring changes if this ring is electrically coupled to another ring, as in CCG structures. The approach used in [16] is only valid in weakly electrically coupled cases and therefore cannot be directly applied to CCG structures.

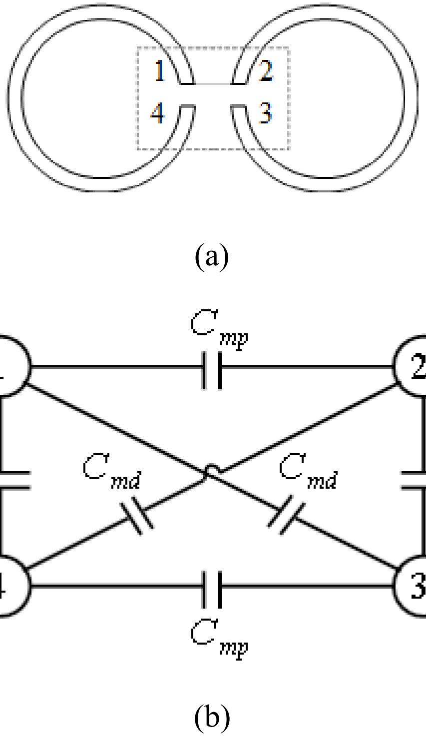

Fig. 3-14 *(a) Illustration of a pair of coupled split metal rings with the four metal plates over the gaps labelled, under the approximation that only the four metal pieces in close proximity from the two rings are taken into account; (b) Equivalent circuit for a four-electrode model; Note that the numbers labelled on the four electrodess in (a) and (b) correspond to each other.*

For the two reasons given above, the aim of the following study is to redefine K and C_{res} used in the existing analytical model in Fig. 3-13 in order to adjust this model to cases with strong electric coupling, such as CCG structures.

One can study the electric coupling device with the aid of a four-electrode model, as given in Fig. 3-14 (b), with the approximation that only the four metal pieces in close proximity to the two coupled split metal rings are taken into account, as shown in Fig. 3-14 (a).

Each pair of the four electrodes can be linked by a conventional geometric capacitor. Gap capacitors C_{gap} are formed by a pair of electrodes on the same ring on each side of the gap; parallel coupling capacitors C_{mp} are formed by a pair of electrodes located on adjacent rings along the parallel direction; diagonal coupling capacitors C_{md} are formed by a pair of electrodes located on adjacent rings along the diagonal direction. For CCG structures, the values of C_{gap}, C_{mp} and C_{md} can exceed the limits of geometry-dependent capacitances, by using capacitive components of arbitrarily large values.

Based on Fig. 3-14 (b), the admittance matrix for the four electrode consists of the self-capacitance C_{self} and the effective mutual capacitance C_{meff} and may be expressed as Eq. (3.35):

$$\begin{bmatrix} i_1 \\ i_2 \end{bmatrix} = \begin{bmatrix} j\omega C_{self} & j\omega C_{meff} \\ j\omega C_{meff} & j\omega C_{self} \end{bmatrix} \cdot \begin{bmatrix} V_1 \\ V_2 \end{bmatrix} \tag{3.35}$$

where V_1 and V_2 are the capacitance-induced voltages across the first and second split metal rings, respectively; the values of C_{self} and C_{meff} were found as functions of C_{gap}, C_{mp} and C_{md} in [96] from circuit analysis, as given by Eqs. (3.36) and (3.37):

$$C_{self} = C_{gap} + \frac{C_{mp} + C_{md}}{2} \tag{3.36}$$

$$C_{meff} = \frac{C_{md} - C_{mp}}{2} \tag{3.37}$$

The impedance matrix can easily be found by taking the inverse of the admittance matrix in Eq. (3.35), as given by Eq. (3.38):

$$\begin{bmatrix} V_1 \\ V_2 \end{bmatrix} = \begin{bmatrix} \frac{C_{self}}{j\omega({C_{self}}^2 - {C_{meff}}^2)} & \frac{C_{meff}}{j\omega({C_{self}}^2 - {C_{meff}}^2)} \\ \frac{C_{meff}}{j\omega({C_{self}}^2 - {C_{meff}}^2)} & \frac{C_{self}}{j\omega({C_{self}}^2 - {C_{meff}}^2)} \end{bmatrix} \cdot \begin{bmatrix} i_1 \\ i_2 \end{bmatrix} \tag{3.38}$$

Here one considers a lossless case where the resistive term can be ignored. The impedance matrix in Eq. (3.35) may then be separated into magnetic and electric parts, as given by Eq. (3.39):

$$\begin{bmatrix} Z_0 & Z_m \\ Z_m & Z_0 \end{bmatrix} = \left(\underbrace{\begin{bmatrix} \frac{1}{j\omega C_{res}} & \frac{1}{j\omega K} \\ \frac{1}{j\omega K} & \frac{1}{j\omega C_{res}} \end{bmatrix}}_{\text{(Electric part)}} + \underbrace{\begin{bmatrix} j\omega L_{res} & j\omega M \\ j\omega M & j\omega L_{res} \end{bmatrix}}_{\text{(Magnetic part)}} \right) \tag{3.39}$$

C_{res} and K may be redefined by comparing the impedance matrix in Eq. (3.38) and the electric part of the impedance matrix in Eq. (3.39). The newly defined C_{res} and K may be expressed as Eqs. (3.40) and (3.41), respectively:

$$C_{res} = \frac{C_{self}^2 - C_{meff}^2}{C_{self}} \tag{3.40}$$

$$K = \frac{C_{self}^2 - C_{meff}^2}{C_{meff}} \tag{3.41}$$

One can therefore define the electric coupling coefficient k_e as a ratio between K and C_{res}, as expressed by Eq. (3.42). This definition shows consistency with the original definition of electric coupling coefficient as expressed in Eq. (2.6).

$$k_e = \frac{2C_{res}}{K} = \frac{2C_{meff}}{C_{self}} \tag{3.42}$$

One can see from Eq. (3.40) that the resonance capacitance C_{res} will vary with the value of C_{meff}. It shows that the resonant frequency of a mixed coupling ring $\omega_0 = \frac{1}{\sqrt{C_{res} L_{res}}}$ changes when varying electric coupling. This coupling-induced shift of resonant frequency has been reported in previous work [97].

One can substitute the redefined C_{res} and K into the original definitions, Eqs. (3.27) (3.28) (3.29), to find the magnetic coupling coefficient k_m, the electric coupling coefficient k_e and the total coupling coefficient k_{total}.

In conclusion, there are two adjustments made in order to apply the existing model proposed in [16] to CCG structures - (i) the resonance capacitance and the mutual capacitance are no longer calculated based on the geometry of structures, instead they are expressed as functions of capacitive component values used in CCG structures; (ii) the calculation of the resonance capacitance is no longer based on an isolated resonator, instead it considers the fact that the electric coupling between two resonators will affect the value of the resonance capacitance C_{res}.

The main contribution of the first adjustment is to understand the formation of the resonance capacitance C_{res} and the mutual capacitance K. The respective contribution of parallel and diagonal coupling capacitances is investigated. Although only parallel capacitance is used in this study, based on this understanding, future studies could explore various ways to introduce additional electric couplings into waveguides similar to CCGs, for example, a structure built with only diagonal coupling capacitances, and a structure built with both diagonal and parallel coupling capacitances.

The second adjustment extends the original model to cases where the effect of electric coupling on the value of resonance capacitance is not negligible. This method is easily adjustable to metamaterial elements of arbitrary shape, if, instead of relying on component values, geometry-based values are used.

The dispersion equation for waveguides composed of mixed coupling resonators can be derived by applying Kirchhoff's Voltage Law to the circuit model shown in Fig. 3-15. This circuit model presents the same coupling mechanism as that shown in Fig. 3-13, but includes an infinite number of elements rather than just two of them in order to derive the dispersion equation.

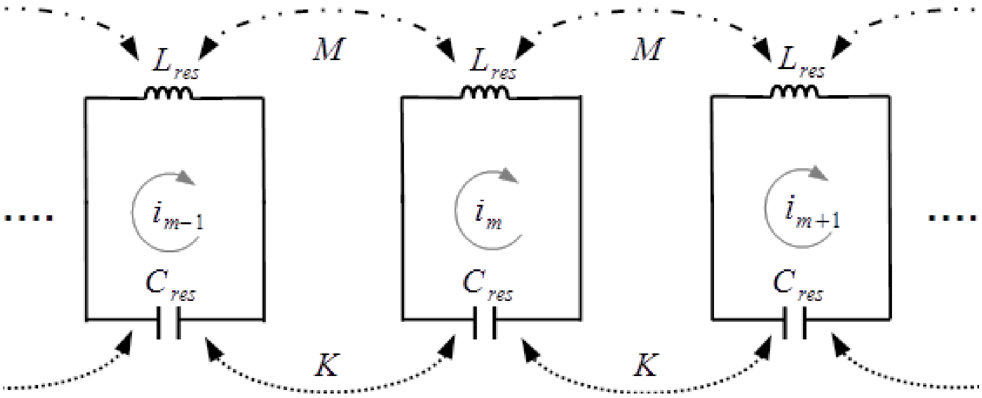

Fig. 3-15 *Circuit model for mixed coupling resonators.*

The total potentials of the m^{th} element are given by Eq. (3.43):

$$Z_0 i_m + Z_m(i_{m-1} + i_{m+1}) = 0 \tag{3.43}$$

where Z_0 and Z_m are the self-impedance and mutual impedance as defined by Eqs. (3.25)(3.26), and i_m is the circulating current in the m^{th} element as defined by Eq. (3.3). The dispersion equation can be derived as Eq. (3.44):

$$cosh(\gamma d) = -\frac{Z_0}{2Z_m} \tag{3.44}$$

The dispersion equation given by Eq. (3.44) directly relates the dispersion characteristics with self-impedance and mutual impedance, which can easily be evaluated once the configurations and components used in the CCG structures are decided. This relationship allows the design to be readily adjusted to suit the conditions and requirements of various dispersion characteristics.

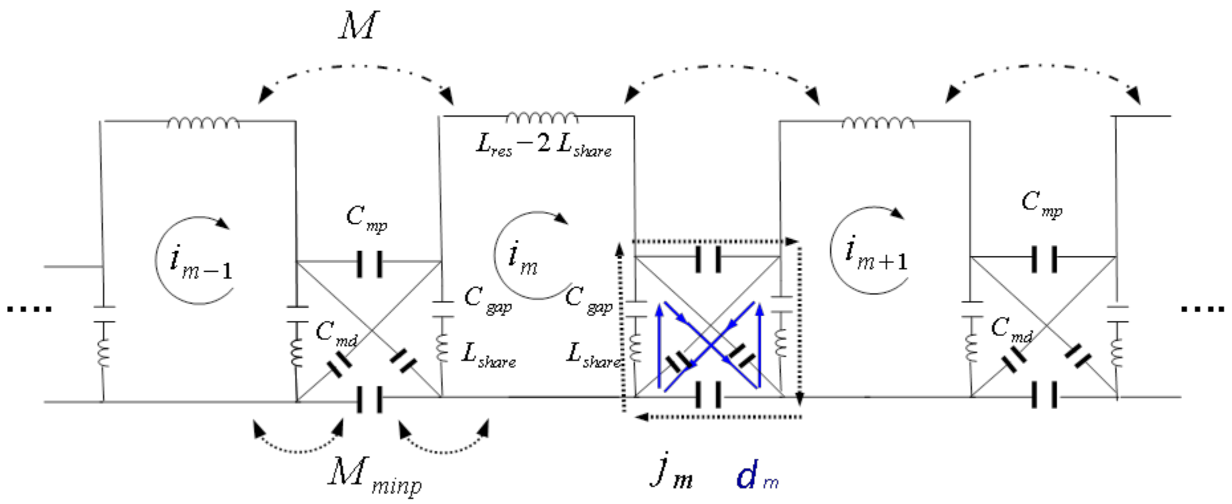

Fig. 3-16 *Complete equivalent circuit for 1-D CCG structures.*

3.7 Application of the Mixed Coupling Model in CCGs

One can assess this newly derived mixed coupling model by applying it to CCG structures and comparing the dispersion equation derived from it with the one derived from circuit analysis.

The dispersion equation of 1-D CCGs with only parallel coupling capacitors C_{mp} was derived via circuit analysis in Eq. (3.6) (see Section 3.2). In order to take all the electric interactions into account, as shown in Fig. 3-14, both parallel coupling capacitors C_{mp} and diagonal coupling capacitance C_{md} should be taken into account in circuit analysis, which needs a complete equivalent circuit for the CCG structure shown in Fig. 3-16. This circuit model is constructed based on the one in Fig. 3-3 by including an additional diagonal coupling capacitance C_{md}. A lossless case is considered here for simplicity; therefore no resistive component is included into this circuit model.

This complete circuit model for 1-D CCG structures includes three kinds of loops, namely, major loops, parallel-configured minor loops formed by C_{mp} and diagonal-configured minor loops formed by C_{md}. The circulating current in the m^{th} major loop is represent by i_m, j_m is the current circulating in the m^{th} parallel-configured minor loop, with C_{mp} represented by the black dashed line in Fig. 3-16, and d_m is the current circulating in the m^{th} diagonal-configured minor loop, with C_{md} represented by the blue line.

Based on this complete circuit model, one can derive the dispersion equation of CCG structures by applying Kirchhoff's Voltage Law to the three types of loops to get the expression given by Eq. (3.45).


(a)

(b)

Fig. 3-17 *Illustration of two adjacent major loops interlinked by parallel low-loss coupling capacitors on two different positions, with r = 0 in (a) and r =* $\frac{1}{4}$ *in (b). The size of the capacitor components is very small, so the inductance contributed by the components is negligible.*

$$cosh(\gamma d) = -\frac{Z_{maj} - \frac{2\left(X_{share} - j\omega M_{minp}\right)^2}{Z_{minp}} - \frac{2(X_{share} - j\omega M_{mind})^2}{Z_{mind}}}{2(j\omega M - \frac{\left(X_{share} - j\omega M_{minp}\right)^2}{Z_{minp}} + \frac{(X_{share} - j\omega M_{mind})^2}{Z_{mind}})} \qquad (3.45)$$

where the impedance of the major loop $Z_{maj} = j\omega L_{res} + \frac{2}{j\omega C_{gap}}$, the resonance inductance of the major loop $L_{res} = 4L$, recalling that L is defined as the inductance associated with each side of a major loop; X_{share} is the impedance of the common branch shared between adjacent major and minor loops, and is given by $X_{share} = j\omega L_{share} + \frac{1}{j\omega C_{gap}}$, where $L_{share} = r * L_{res}$, the variable r represents how much L_{res} is shared between major and minor loops, with a range of $0 \leq r \leq \frac{1}{4}$, with $r = 0$ representing the case when there is no common metal branch between the major and minor loops (Fig. 3-17 (a)) and $r = \frac{1}{4}$ indicating that the entire side branch is shared between the two square-shaped loops (Fig. 3-17 (b)), the value of r is $\frac{1}{8}$ in the demonstration structure presented in Fig. 3-1 (a), Z_{minp} is the impedance of the minor loop formed with C_{mp}, and is given by $Z_{minp} = 2j\omega L_{share} + \frac{2}{j\omega C_{gap}} + \frac{2}{j\omega C_{mp}}$; Z_{mind} is the impedance of the minor loop formed with C_{md}, and is given by $Z_{mind} = 2j\omega L_{share} + \frac{2}{j\omega C_{gap}} + \frac{2}{j\omega C_{md}}$; C_{gap}, C_{mp}, C_{md}, M, M_{minp} and M_{mind} are as defined previously.

When looking back at the dispersion equation derived from the mixed coupling model in Eq. (3.44), one can expand it as Eq. (3.46):

$$cosh(\gamma d) = -\frac{Z_{maj} - \frac{2(X'_{share})^2}{Z_{minp}} - \frac{2(X'_{share})^2}{Z_{mind}}}{2(j\omega M - \frac{(X'_{share})^2}{Z_{minp}} + \frac{(X'_{share})^2}{Z_{mind}})} \tag{3.46}$$

where the definition of Z_{maj}, Z_{minp}, Z_{mind} and M are unchanged and the shared impedance is $X'_{share} = \frac{1}{j\omega C_{gap}}$.

The dispersion equation derived from circuit analysis (Eq. (3.45)) would become equivalent to that derived from the mixed coupling model (Eq. (3.46)) with the following two approximations:

(1) The magnetic couplings between the major loop and two kinds of minor loop, M_{minp} and M_{mind}, are negligible;

(2) There is no inductance included in the electric coupling device (r = 0). In practice, there must be some inductance included in the electric coupling devices due to the space taken up by capacitor components and soldering joints.

The first approximation (negligible M_{minp} and M_{mind}) was quantitatively verified, as given in Table 3-2. When M_{minp} and M_{mind} are taken into account, 1-D CCGs can be considered as bi-atomic structures, consisting of alternating major and minor loops. With this approximation, the original minor loops are functioning only as electric coupling devices interlinking adjacent major loops, making 1-D CCGs mono-atomic structures.

The validity of the second approximation (r = 0) can be assessed with the aid of two extreme cases, in which $C_{md} = 0$ and $C_{mp} = 0$. Under these two conditions, Eq. (3.45) can be expressed as Eqs (3.47) and (3.48), respectively:

$$\mathit{If}\ C_{md} = 0, \qquad \cosh\gamma d = -\frac{j\omega L + \dfrac{2(C_{gap} + \frac{C_{mp}}{2})}{j\omega(C_{gap}^2 + C_{gap}C_{mp})}}{j\omega L_m + \dfrac{-\frac{C_{mp}}{2}}{j\omega(C_{gap}^2 + C_{gap}C_{mp})}} \tag{3.47}$$

$$\mathit{If}\ C_{mp} = 0, \qquad \cosh\gamma d = -\frac{j\omega L + \dfrac{2(C_{gap} + \frac{C_{md}}{2})}{j\omega(C_{gap}^2 + C_{gap}C_{md})}}{j\omega L_m + \dfrac{\frac{C_{md}}{2}}{j\omega(C_{gap}^2 + C_{gap}C_{md})}} \tag{3.48}$$

Based on the dispersion equations derived from the mixed coupling model (Eqs. (3.47) and (3.48) ($r = 0$)), the frequency bounds f_{L1} and f_{L2} of the available bandwidth can be found in the same way as was used to derive Eqs. (3.8)–(3.11). The frequency bounds f_{L1} and f_{L2} of the passband and its FBW were calculated with C_{mp} and C_{md} both ranging from 1 pF to 1 μF, as shown by the red lines in Fig. 3-18. These variables were also calculated for cases where $r = \frac{1}{8}$ and the extreme case where $r = \frac{1}{4}$, using the dispersion equation derived from circuit analysis (Eq. (3.45)) and presented for comparison with the black and blue lines, respectively, in Fig. 3-18.

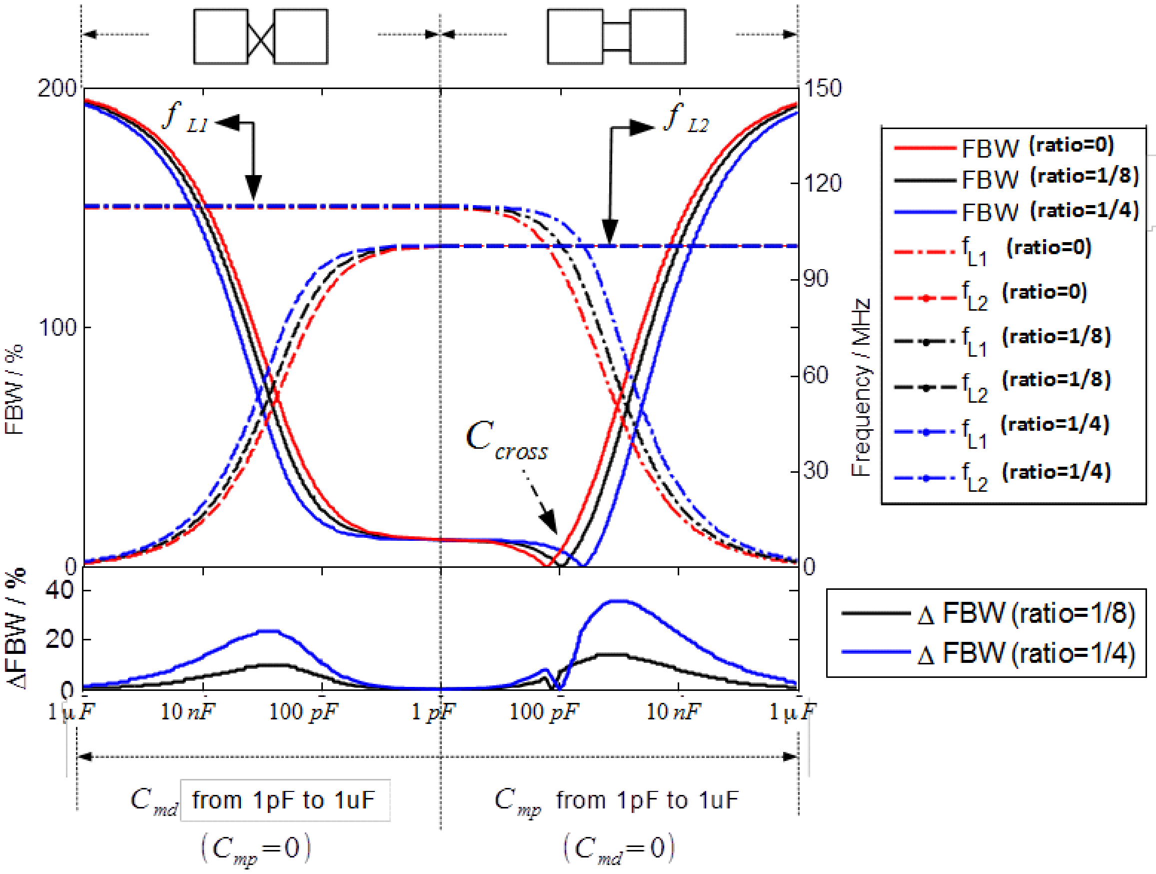

Fig. 3-18 The upper part of the diagram shows the frequency bounds of the passband and its FBW of 1-D CCG structures with C_{mp} and C_{md} both ranging from 1 pF up to 1 μF when r = 0, 1/8 or 1/4; the bottom part shows the FBW difference between the case where r = 0 and the case where r = 1/4 or 1/8.

The upper part of Fig. 3-18 shows that the frequency bounds f_{L1} and f_{L2} calculated from circuit analysis and the mixed coupling model display the same variation trends when C_{md} and C_{mp} change. For convenience, the two study regions in Fig. 3-18 are named as the C_{mp}

region, where $C_{md} = 0$ and 1 pF $\leq C_{mp} \leq$ 1 μF on the right-hand side, and the C_{md} region, where $C_{mp} = 0$ and C_{md} has the same range on the left-hand side. One recalls from the analysis of the C_{mp} region in Section 3.4 that the ordering between f_{L1} and f_{L2} changes when C_{mp} goes above the intersection at which f_{L1} and f_{L2} intersect and the passband disappears. When $C_{mp} < C_{cross}$, 1-D CCGs support backward wave propagation as $f_{L1} > f_{L2}$, while for $C_{mp} > C_{cross}$, 1-D CCGs support forward wave propagation as $f_{L1} < f_{L2}$. One can find that 1-D CCGs support backward wave propagation as $f_{L1} > f_{L2}$ over the entire C_{md} region.

A 1-D CCG structure with electric coupling devices made of C_{mp} only can be considered as the symmetric twist of the one made of C_{md} of the same value. The electric coupling devices made of C_{md} provide negative electric coupling, which reinforces negative coplanar magnetic coupling. One can see that the passband keeps expanding as C_{md} increases over the entire C_{md} region. As the counterpart of C_{md}, electric coupling devices made of C_{mp} provide positive electric coupling, which offsets negative coplanar magnetic coupling. Positive coupling exactly cancels negative coupling at the intersection where $C_{mp} = C_{cross}$, and results in the disappearance of the passband. Negative coupling wins in the region where $C_{mp} < C_{cross}$, so that the waveguide supports backward wave propagation, while positive coupling wins in the region where $C_{mp} > C_{cross}$, so that the waveguide supports forward wave propagation.

The bottom part of Fig. 3-18 presents the values of ΔFBW, which is the difference between FBW calculated with $\frac{1}{8}$ (black line) or $\frac{1}{4}$ (blue line) based on the circuit analysis model of Eq. (3.45) and FBW calculated with the mixed coupling model under the $r = 0$ approximation using Eqs. (3.47) and (3.48). One can see that the approximation error reaches its maximum value around the value of 1 nF in both the C_{mp} and C_{md} regions, and tends to converge when C_{mp} or C_{md} keeps increasing after the maximum point. Here, 10% of the circuit analysis results would be considered an acceptable level of error in the approximation in the mixed coupling model. In the case where $r = \frac{1}{4}$, the acceptable level of approximation error can only be achieved when $C_{mp} > 30$ nF or $C_{md} > 10$ nF. When the shared inductance is reduced to $r = \frac{1}{8}$, the acceptable error threshold comes down to $C_{mp} > 3$ nF or $C_{md} > 1.5$ nF. As this study is aimed at expanding the available bandwidth with high values of either C_{mp} or C_{md}, it is perfectly reasonable to apply the mixed coupling model to predict the dispersion behaviour of 1-D CCG structures.

One can now explore the values of C_{mp} and C_{md} required to obtain a certain amount of available bandwidth by 1-D CCGs with varying values of r. Here, one takes FBW = 150% as an example to illustrate how the required C_{mp} and C_{md} change over the full range $0 \leq r \leq \frac{1}{4}$, as shown in Fig. 3-19. One finds that a certain value of FBW can be achieved with the penalty of increasing C_{mp} and C_{md} when the value of r increases.

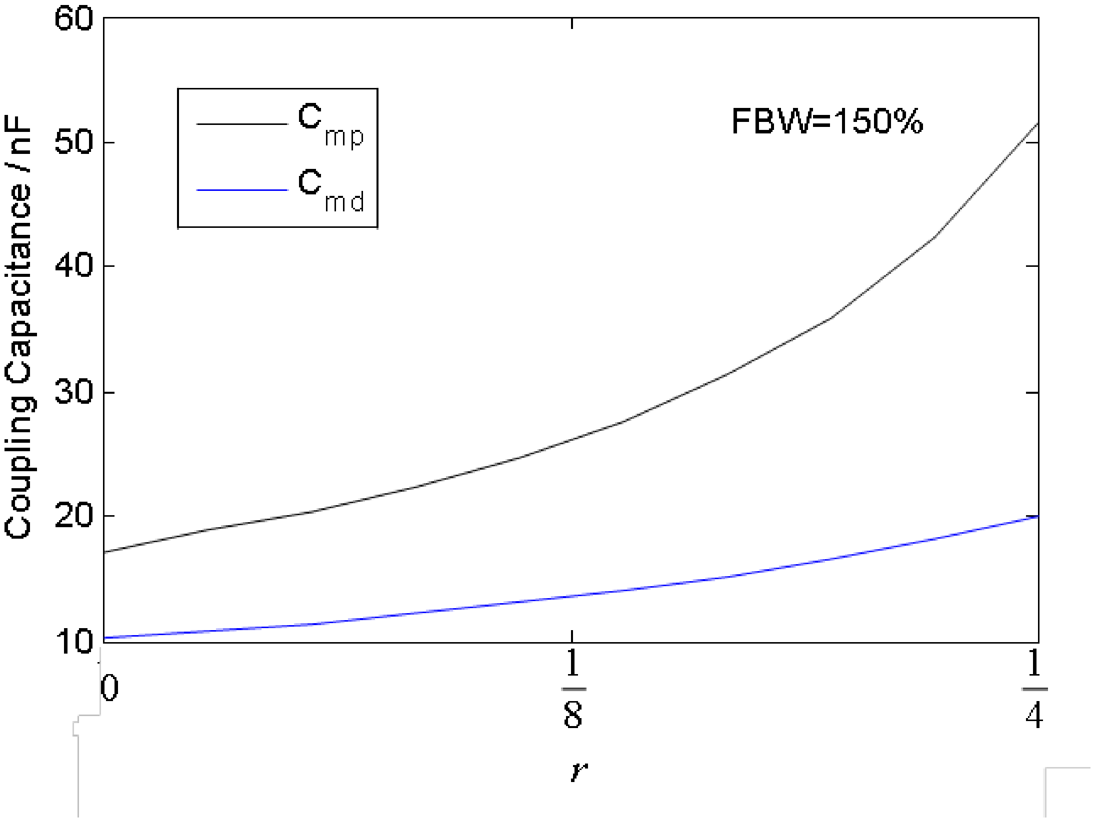

Fig. 3-19 Required values of C_{mp} *and* C_{md} *to achieve FBW = 150% over the full range of* $0 \leq r \leq \frac{1}{4}$.

3.8 Impedance Matrix Derived from the Mixed Coupling Model

In the mixed coupling model a 1-D CCG structure can be considered as a ladder circuit of major loops interlinked by electric coupling devices which were originally named minor loops. This model essentially allows a bi-atomic CCG structure to be considered as a mono-atomic structure, just like MIWs.

When considering a finite 1-D CCG consisting of N major loops, its impedance matrix **Z** can be described by an N×N square matrix, as given by Eq. (3.49):

$$\boldsymbol{Z} = \begin{pmatrix} Z_0 & Z_m & 0 & \dots & \dots & \dots & 0 \\ Z_m & Z_0 & Z_m & 0 & \dots & \dots & \vdots \\ 0 & Z_m & Z_0 & Z_m & 0 & \dots & \vdots \\ \vdots & \ddots & \ddots & \ddots & \ddots & \ddots & \vdots \\ \vdots & \dots & 0 & Z_m & Z_0 & Z_m & 0 \\ \vdots & \dots & \dots & 0 & Z_m & Z_0 & Z_m \\ 0 & \dots & \dots & \dots & 0 & Z_m & Z_0 \end{pmatrix} \tag{3.49}$$

where the self-impedance $Z_{\mathbf{0}}$ and the coupling impedance Z_m are defined by the mixed coupling model as given by Eq. (3.39).

When expanding to a 2-D structure, a new coupling term, the magnetic coupling between diagonally adjacent elements M_{diag}, needs to be taken into account. Recall the matrix transformation applied to derive the impedance matrix of the 2-D MIW (see Section 2.3). Following the same method, one can obtain an M×M impedance matrix for an M×N 2-D CCG array (*M* rows and *N* columns), as given by Eq. (3.50):

$$\boldsymbol{Z} = \begin{pmatrix} \boldsymbol{A} & \boldsymbol{B} & \boldsymbol{0} & \dots & \dots & \boldsymbol{0} \\ \boldsymbol{B} & \boldsymbol{A} & \boldsymbol{B} & \boldsymbol{0} & \dots & \vdots \\ \boldsymbol{0} & \boldsymbol{B} & \ddots & \ddots & \ddots & \vdots \\ \vdots & \ddots & \ddots & \ddots & \boldsymbol{B} & \boldsymbol{0} \\ \vdots & \dots & \boldsymbol{0} & \boldsymbol{B} & \boldsymbol{A} & \boldsymbol{B} \\ \boldsymbol{0} & \dots & \dots & \boldsymbol{0} & \boldsymbol{B} & \boldsymbol{A} \end{pmatrix} \tag{3.50}$$

where matrix $\boldsymbol{A}$ describes couplings inside a row and matrix $\boldsymbol{B}$ describes inter-row couplings. $\boldsymbol{A}$ and $\boldsymbol{B}$ are both N×N matrices and are defined by Eqs. (3.51) and (3.52):

$$\boldsymbol{A} = \begin{pmatrix} Z_0 & Z_m & 0 & \dots & \dots & \dots & 0 \\ Z_m & Z_0 & Z_m & 0 & \dots & \dots & \vdots \\ 0 & Z_m & Z_0 & Z_m & 0 & \dots & \vdots \\ \vdots & \ddots & \ddots & \ddots & \ddots & \ddots & \vdots \\ \vdots & \dots & 0 & Z_m & Z_0 & Z_m & 0 \\ \vdots & \dots & \dots & 0 & Z_m & Z_0 & Z_m \\ 0 & \dots & \dots & \dots & 0 & Z_m & Z_0 \end{pmatrix} \tag{3.51}$$

$$\boldsymbol{B} = \begin{pmatrix} Z_m & j\omega M_{diag} & 0 & \cdots & \cdots & \cdots & 0 \\ j\omega M_{diag} & Z_m & j\omega M_{diag} & 0 & \cdots & \cdots & \vdots \\ 0 & j\omega M_{diag} & Z_m & j\omega M_{diag} & 0 & \cdots & \vdots \\ \vdots & \ddots & \ddots & \ddots & \ddots & \ddots & \vdots \\ \vdots & \cdots & 0 & j\omega M_{diag} & Z_m & j\omega M_{diag} & 0 \\ \vdots & \cdots & \cdots & 0 & j\omega M_{diag} & Z_m & j\omega M_{diag} \\ 0 & \cdots & \cdots & \cdots & 0 & j\omega M_{diag} & Z_m \end{pmatrix} \tag{3.52}$$

Knowing **V**, the M×N matrix representing the voltage applied to each element, and the impedance matrix $\boldsymbol{Z}$, it is possible to calculate currents circulating in each element of a finite 1-D or 2-D CCG array as expressed by Eq. (3.53):

$$\mathbf{I} = \mathbf{Z}^{-1} \cdot \mathbf{V} \tag{3.53}$$

3.9 Conclusions

In this chapter a new variant of the metamaterial waveguide, the CCG, has been proposed, which incorporates additional electric coupling into traditional purely magnetically coupled MIWs, and hence could improve coupling performance, reduce loss and increase bandwidths compared to conventional MIWs. 1-D CCG structures are made by connecting coupling capacitors over the inter-element gaps between traditional MIW loops, and can be characterized as a continuous circuit mesh consisting of alternating major loops and minor loops.

The coupling mechanism of CCG structures can be described as the competition between the negative magnetic coupling between adjacent major loops and the positive electric coupling introduced by coupling capacitors.

CCG waveguides have a negative magnetic coupling-dominated region and a positive electric coupling-dominated region, depending on the relative significance of the two types of coupling. In the negative magnetic coupling-dominated region, CCG waveguides support backward MI wave propagation in much the same way that purely magnetically coupled waveguides do. In the positive electric coupling-dominated region, CCG waveguides support forward EI wave propagation.

In the positive electric coupling dominated region, the pass-band keeps broadening with increased electric coupling strength. The analytical dispersion analysis predicts that a 1-D CCG waveguide built with parallel coupling capacitance C_{mp}=1μF can achieve the fractional bandwidth achieved of 192.4%, which has closely approximates 200% limit of an UWB channel.

On the boundary between the two propagation modes, a no-propagation point was found where the positive and negative coupling exactly cancels each other. At this point, CCG waveguides still exhibit magnetic resonances without permitting end-to-end energy propagation. This property of CCGs could be exploited in super lens imaging applications in the future.

An existing analytical model from previous study [16] is adjusted and then applied to 1-D CCG waveguides. The adjustment made in order to apply this model to CCG waveguides includes: (i) the resonance capacitance and the mutual capacitance are no longer calculated based on the geometry of structures, instead they are expressed as functions of capacitive component values used in CCG structures; (ii) the calculation of the resonance capacitance is no longer based on an isolated resonator, instead it considers the fact that the electric coupling between two resonators will affect the value of the resonance capacitance.

The first adjustment is made based on the very nature of CCG waveguide in which electric coupling is determined by capacitive components used in CCG structures. The main contribution of this adjustment is to understand the formation of the resonance capacitance C_{res} and the mutual capacitance K. The electric coupling is analysed with the aid of a four-electrode model, including coupling capacitance included in both parallel and diagonal configurations. It is shown that the parallel coupling capacitance contributes to positive electric coupling; while the diagonal coupling capacitance contributes to negative electric coupling. Although only parallel capacitance is used in this study, based on this understanding, future studies could explore various ways to introduce additional electric couplings into waveguides similar to CCGs, for example a structure built with diagonal capacitances only and a structure includes both diagonal and parallel capacitances.

The second adjustment extends the original model to cases where the effect of electric coupling on the value of resonance capacitance is not negligible.

This adjusted analytical model is verified by comparing to the dispersion equation derived from circuit analysis. It shows that parallel coupling capacitance introduces positive electric coupling which carries forward EI waves; while diagonal coupling capacitance introduces negative electric coupling which carries backward EI waves.

When applying this adjusted model to 1-D CCGs, one can simplify the bi-atomic model to a monoatomic model, in which the original minor loops are only considered as electric coupling devices interlinking adjacent major loops. After being simplified to a monoatomic model, the derivation process of dispersion equations, impedance matrix, as well as the dimension extension to 2-D structures can be much simplified.

This adjusted model helps to evaluate the respective contributions of the magnetic and electric couplings. Therefore, it allows the design of many mixed coupling waveguides, like 1-D CCGs, to be readily adjusted to suit the conditions and requirements of various dispersion characteristics. This adjusted model is easily adjustable to metamaterial elements of arbitrary shape, if, instead of relying on component values, geometry-based values are used.

CHAPTER 4

EXPERIMENTAL DEMONSTRATION

In the previous chapter, the dispersion characteristics and coupling mechanism of 1-D CCG waveguides were studied. Their dispersion characteristics from analytical predictions show two different regimes: a negative magnetic coupling-dominated regime, supporting backward MI wave propagation, and a positive electric coupling-dominated regime, supporting forward EI wave propagation.

In this chapter, these analytical dispersion characteristics will be verified experimentally with the demonstrational structures previously introduced in Section 3.3. In Section 4.1, the experimental setup will be described. Section 4.2 will show the measured forward scattering parameter mapping against locations along the demonstrational structure. In Section 4.3, dispersion curves will be extracted from the measured standing wave amplitude pattern by two different methods and compared with analytical predictions.

4.1 Experimental Setup

A simple experiment has been conducted to verify the analytical dispersion characteristics described in the previous chapter. Four 10-element 1-D CCG demonstration structures were

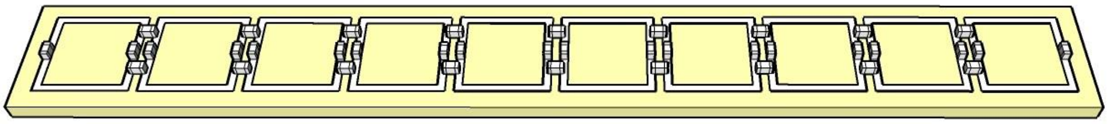

Fig. 4-1 *Sketch of a 10-element 1-D CCG waveguide demonstration structure.*

constructed using commercial printed circuit board (PCB) fabrication techniques. A sketch of a demonstration structure is shown in Fig. 4-1 and a photograph of it can be found in Fig. 4-2.

1-D CCG arrays consisting of ten square copper loops of dimensions given in Table 3-1 were fabricated by PWCircuits Ltd [98] on an FR4 substrate using photolithography. Each square copper loop had an outer dimension of 9.5×9.5 mm with a 0.9 mm gap between loops, as previously illustrated in Fig. 3-1 (a). Surface-mounted ceramic multilayer chip capacitors were soldered across the two gaps in each square track to complete a major loop (noted as C_{gap}) and soldered across the inter-element gaps to form a minor loop (noted as C_{mp}). The value of C_{gap} was set at 220 pF. To explore the dispersion characteristics of 1-D CCGs with different electric coupling strengths, four demonstration waveguides were built: one 1-D MIW and three 1-D CCGs with $C_{mp}$of 100 pF, 2 nF and 1 μF, respectively. The specifications of the capacitor components C_{gap} and C_{mp} used in the experiment are given in Table 4-1.

Table 4-1 *Component specifications of capacitors C_{gap} and C_{mp} used in the experiments*

Capacitance	**Component Specifications**			
	Tolerance	**Size**	**Dielectric**	**Brand**
C_{gap} (220 pF)	±10%	0603	X5R	KEMET
C_{mp} (100 pF)	±10%	0603	X5R	YAGEO
C_{mp} (2 nF)	±10%	0603	X5R	KEMET
C_{mp} (1 μF)	±10%	0603	X5R	TDK

As predicted in Fig. 3-6 (see Section 3.4), the passband given by the demonstration structure is bounded by upper frequency bounds never exceeding 120 MHz, which gives a minimal free-space wavelength of 2.5 m. The 10-element demonstration structures constructed in this experiment had a total length of 104 mm, which is much smaller than the relevant free-space wavelength. Therefore, the quasi-static approximation used to derive the circuit-based model and the mixed coupling model (see Section 3.7) is still valid for this demonstration structure.

As shown in Fig. 4-2, the measurement was made by non-resonant loop antennas, transmitter antenna T_x and receiver antenna R_x, to provide the source signal and receive the structure's response. T_x and R_x were simple, non-resonant loop probes of identical geometries, made from 9.2 cm lengths of RG402/U semi-rigid cable with an 8 mm outer diameter loop made from its 1 mm-thick inner wire. The probes were placed 6 mm away from the surface of the element's copper track, and this also took into account the 1.6 mm thickness of the PCB board. The two probes were both held in place by Perspex clamps and polytetrafluoroethylene (PTFE) rods. The R_x side was screwed into a Perspex backboard, while the T_x side was flexible and moveable as it was attached to the arm of a computer-controlled translation stage.

During the measurement, the transmitter loop antenna T_x was positioned under the PCB board, with its centre vertically aligned with the centre of the first major loop. Meanwhile, the receiver loop antenna R_x was scanned over the top with the aid of the computer-controlled translation stage mover, starting at the edge of the first major loop and then scanning 91 uniformly distributed points along the structure, until reaching the edge of the last major loop.

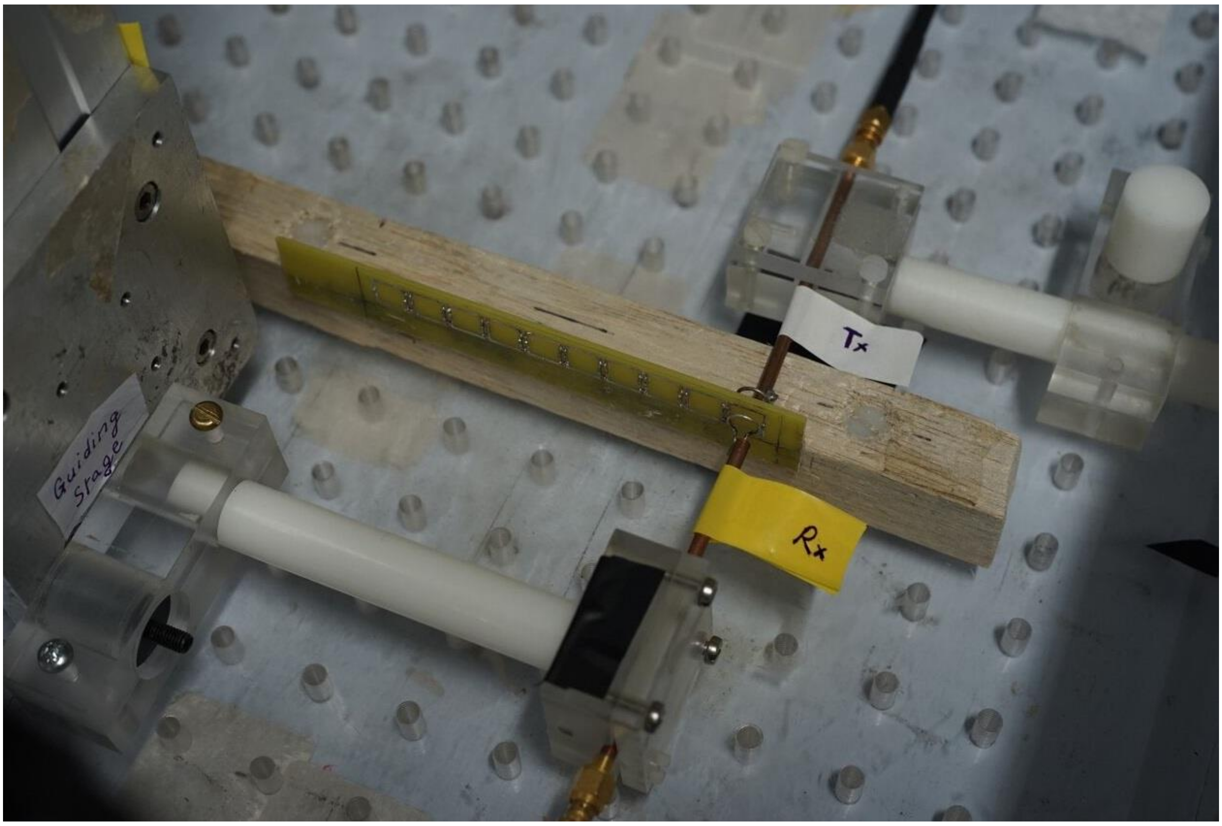

Fig. 4-2 *Photograph of the two loop probes T_x and R_x held in place by Perspex clamps and PTFE rods which were screwed into a Perspex backboard. The PCB board printed with 10-element 1-D CCGs was placed between the two probes, with the centre of the first major loop vertically aligned with the centres of both T_x and R_x.*

A schematic diagram of the experimental apparatus is presented in Fig. 4-3 with an onsite photograph shown in Fig. 4-4. The two non-resonant probe antennas, transmitter probe antenna T_x and receiver probe antenna R_x, were connected to Ports 1 and 2, respectively, on a HP 8753ES vector network analyser (VNA) via 50 Ω coaxial cables, to record the forward scattering parameter S_{21} – representing the complex magnitude ratio between wave received by the R_x antenna and the incident wave from the T_x antenna. The real and imaginary components of S_{21} were taken as the average of 16 scans of 1601 points in the frequency range 50 kHz–150 MHz. The VNA was controlled by a computer via a general purpose interface bus (GPIB) to universal serial bus (USB) interface.

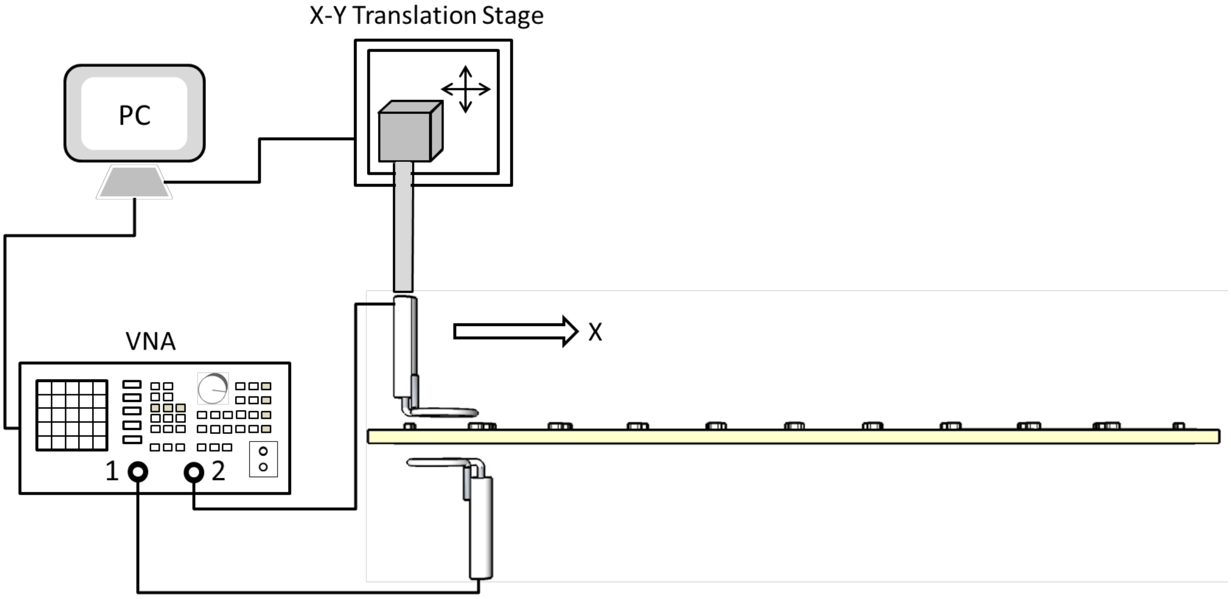

Fig. 4-3 *Experimental apparatus with the loop probes* T_x *and* R_x *connected to a vector network analyser (VNA) for measurements of the forward scattering parameter* S_{21}*. During the measurement,* T_x *was positioned below the PCB, while* R_x *scanned along the structure. The movement was controlled by a computer-controlled translation stage mover.*

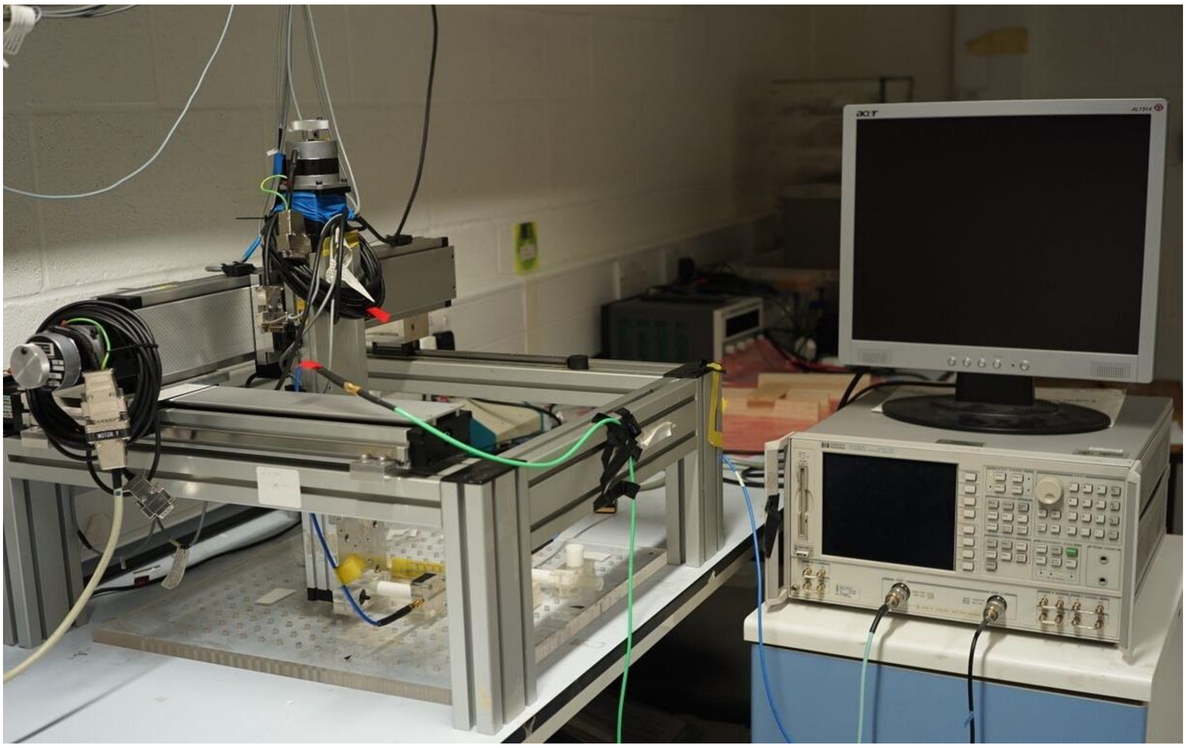

Fig. 4-4 *Photograph of the computer-controlled translation stage, configured to move in two axes at a time with a HP 8753ES VNA connected to two non-resonant probe antennas – transmitter probe antenna* T_x *and receiver probe antenna* R_x *– via 50 Ω coaxial cables.*

4.2 Experimental Results

Fig. 4-5 (a)–(d) shows the log-magnitudes of forward scattering parameters S_{21} measured across the VNA ports along the four demonstration structures with the same scale of –90 to –20 dB. The results for the 1-D MIW structure (without C_{mp}) and the 1-D CCG structures with a C_{mp} of 100 pF are presented over the frequency range 80–120 MHz, while the other two 1-D CCG structures with a C_{mp} of 2 nF and 1 μF are presented over the frequency range 50 kHz to 120 MHz.

One can see that a broadband beginning with a strong signal occurring around the first element due to the strong direct coupling between R_x and T_x, as one of them is positioned just above the other. For all later cells, a clear passband emerges. The transmission spectra show very clear minima whose positions vary with frequency. They are caused by the standing waves appearing in the structures, because of the strong reflection at the end. Note that the S_{21} spectra of the 1-D CCG with C_{mp}= 100 pF stops at the eighth element position because of damage to this PCB during the experimental process, though it did not affect the analysis based on this result.

For some frequencies, one can see that the spatial period of the standing wave varies along the structure. For example, in the spectra measured with $C_{mp} = 2$ nF at 60 MHz, the spatial period of the last standing wave pattern is larger than the first two; in the spectra measured with $C_{mp} = 2$ nF around 87 MHz, the spatial periods of the first and the third wave patterns are apparently larger than the spatial periods of the second and the fourth wave patterns.

Two reasons might account for this phenomenon:

(i) **Reflection impedance:** the four demonstration structures are constructed with 10 major loops and 9 minor loops in between. The first 9 CCG elements include one major loop and one minor loop; however, the last CCG element only has one major loop. The incomplete period at the end of the waveguide may introduce a phase shift to the reflection coefficient. A positive phase shift means that the wave is effectively reflected back from a further point than the real terminus of the line, and makes the last standing wave pattern shorter than the others. A negative phase shift means that the wave is effectively reflected back from a nearer point than the real terminus of the line, and makes the last standing wave pattern longer than the others.

This reason may account for the last standing wave pattern appearing larger as in the first example aforementioned ($C_{mp} = 2$ nF at 60 MHz).

(ii) **Capacitance tolerance:** The standard value of the gap capacitance C_{gap} is 220 pF and gives the resonant frequency of a major loop as 106.04 MHz. The capacitor component used in the four demonstration structures has a 10% tolerance and could range between 198 pF to 242 pF. This tolerance leads a variation in the resonant frequency of the major loop, ranging from 101.10 MHz - 111.77 MHz. When waves are propagating along this non-uniform waveguide, reflections not only happen at the terminus of the waveguide, but also can happen between different CCG elements [63]. The superposition between the incident wave and the waves reflected back from different elements can cause unpredictable variations of standing wave patterns.

This reason may account for the varying spatial period as in the second example aforementioned ($C_{mp} = 2$ nF around 87 MHz).

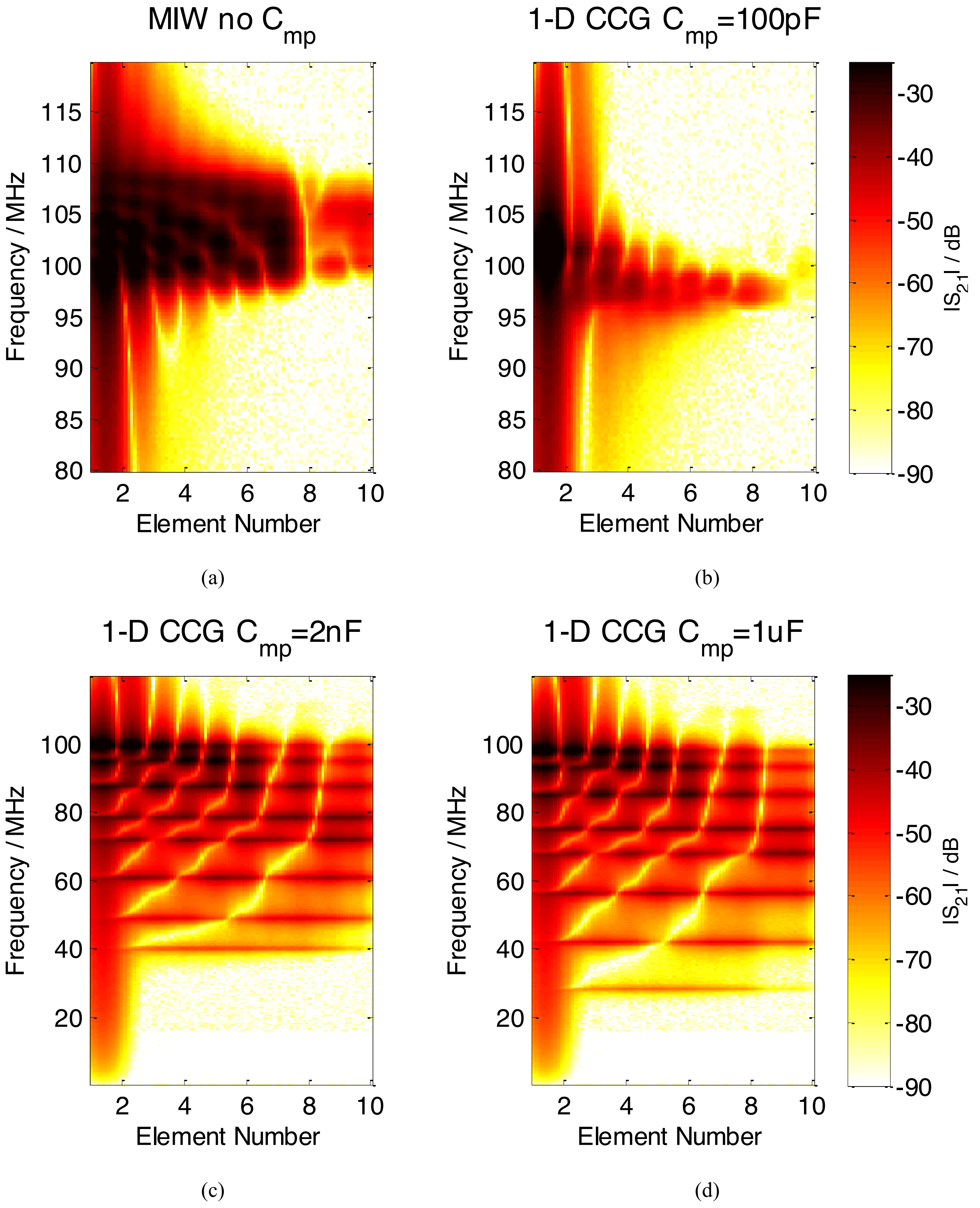

(a) (b)

(c) (d)

Fig. 4-5 *Log-magnitude of S_{21} (dB scale) measured along the four demonstration structures: (a) a 10-element MIW structure without C_{mp}; and three 10-element CCG structures with (b) C_{mp}= 100 pF; (c) C_{mp}= 2 nF; (d) C_{mp}= 1 μF, respectively. S_{21} scanning results of the CCG with C_{mp}= 100 pF stops at the eighth element position because of damage to this PCB board during the experimental process, though it did not affect the analysis based on this result.*

4.3 Dispersion Analysis

In this section, the dispersion characteristics α and β are extracted from the experimental measurements by two different methods. The first method finds the best fit between the measured and analytical waveforms, which will later be referred to as the 'waveform fitting method'; the second method established in [68] explicitly derives α and β as a function of the phase and amplitude measurements at three consecutive resonant loops, which will later be referred to as the 'explicit derivation method'.

4.3.1 Waveform Fitting Method

To extract the dispersion characteristics α and β, the magnitude and phase of the induced current in the receiver antenna probe R_x were fitted against a range of analytical test currents. The best fit found on χ^2 criteria gave the sought-after experimental dispersion characteristics.

The magnitude and phase of the induced current in R_x was measured at 91 scan points. The first 9 scan points were excluded due to the strong direct coupling between T_x and R_x, and only the remaining 82 scan points were used as measured data. The reason for this is that there was strong direct coupling between the transmitter antenna T_x and the receiver antenna R_x when the two were placed facing each other at the beginning of the scan.

This measured induced current is assumed to be proportional to the magnetic flux coupled to the receiver antenna probe R_x from its nearest major loop, and therefore proportional to the current circulating in this nearer major loop.

To better represent this measured induced current, these analytical test currents take into account two factors: (i) the wavelike current function and (ii) the probe-to-loop coupling. These two factors will be discussed in detail in the following sections.

(i) The wavelike current function

A 1-D CCG structure can essentially be considered as a bi-atomic metamaterial structure, as discussed in Section 3.2, so there are two different wavelike currents circulating in the major and minor loops, respectively. When applying the mixed coupling model derived in Section 3.7, a bi-atomic structure can be simplified to a mono-atomic model, in which only the circulating current in the major loops needs to be considered.

The analytical test current circulating in the major loops is a function of the incident wave, as well as of the reflected wave when considering that the demonstration structure has a finite length. The current circulating in the n^{th} major loop can expressed as Eq. (4.1):

$$i_n = I_0 e^{-n\gamma d} + I_r e^{-(N-n)\gamma d} \tag{4.1}$$

where I_0 is the current amplitude at the first major loop, I_r is the current amplitude at the last major loop at which the reflected wave starts to propagate, N is the total element number (N = 10 in the demonstration structures), d represents the spatial period of the structure, which is the distance between the centres of a pair of adjacent major loops, and the propagation constant is $\gamma = \alpha + j\beta$, where α and β are the attenuation constant and the wave number, respectively.

(ii) The probe-to-loop coupling effect

How much current can be induced in the receiver antenna probe R_x not only depends on the current circulating in its nearest major loop, but also on the coupling strength between R_x and this major loop. More specifically, this coupling strength reaches its maximum when R_x is positioned immediately above this major loop, and reaches its minimum when the R_x probe is positioned over the middle of two adjacent major loops. This periodic variation in the coupling strength between the receiver antenna probe R_x and its nearest major loop is later referred as the 'probe-to-loop coupling effect'.

The probe-to-loop coupling parameter $\Gamma_{probe-loop}$ can be represented by Eq. (4.2):

$$\Gamma_{probe-loop}(n) = 1 - \delta\cos(2n\pi) \tag{4.2}$$

where n is the position of the probe as in Eq. (4.1) expressed as the number of loops, n being an integer when between two loops, and δ is a value to be fitted, representing the ratio between the variation amplitude of the probe-to-loop strength and the spatial average coupling strength.

The analytical current can be expressed as a superposition of these two factors by multiplying the probe-to-loop coupling parameter $\Gamma_{probe-loop}$ (Eq. (4.2)) by the travelling wave-like current expression (Eq. (4.1)). This analytical current form i'_ncan be expressed as Eq. (4.3):

$$i'_n = (I_o e^{-n\gamma d} + I_r e^{-(N-n)\gamma d})(1 - \delta\cos(2n\pi)) \tag{4.3}$$

This superposition of the two factors can be illustrated in Fig. 4-6, where the green curve represents the probe-to-loop coupling parameter $\Gamma_{probe-loop}$ from Eq. (4.2), the blue curve is the wave-like current from Eq. (4.1) and the red curve is the resulting test analytical waveform.

For each frequency, one can extract the dispersion characteristics α and β by fitting the measured current pattern against a range of analytical patterns. The best fit is found by applying χ^2 criteria to all useful data points (85 data points in this case, as discussed at the start of Section 4.3.1) and results in the experimentally extracted dispersion characteristics.

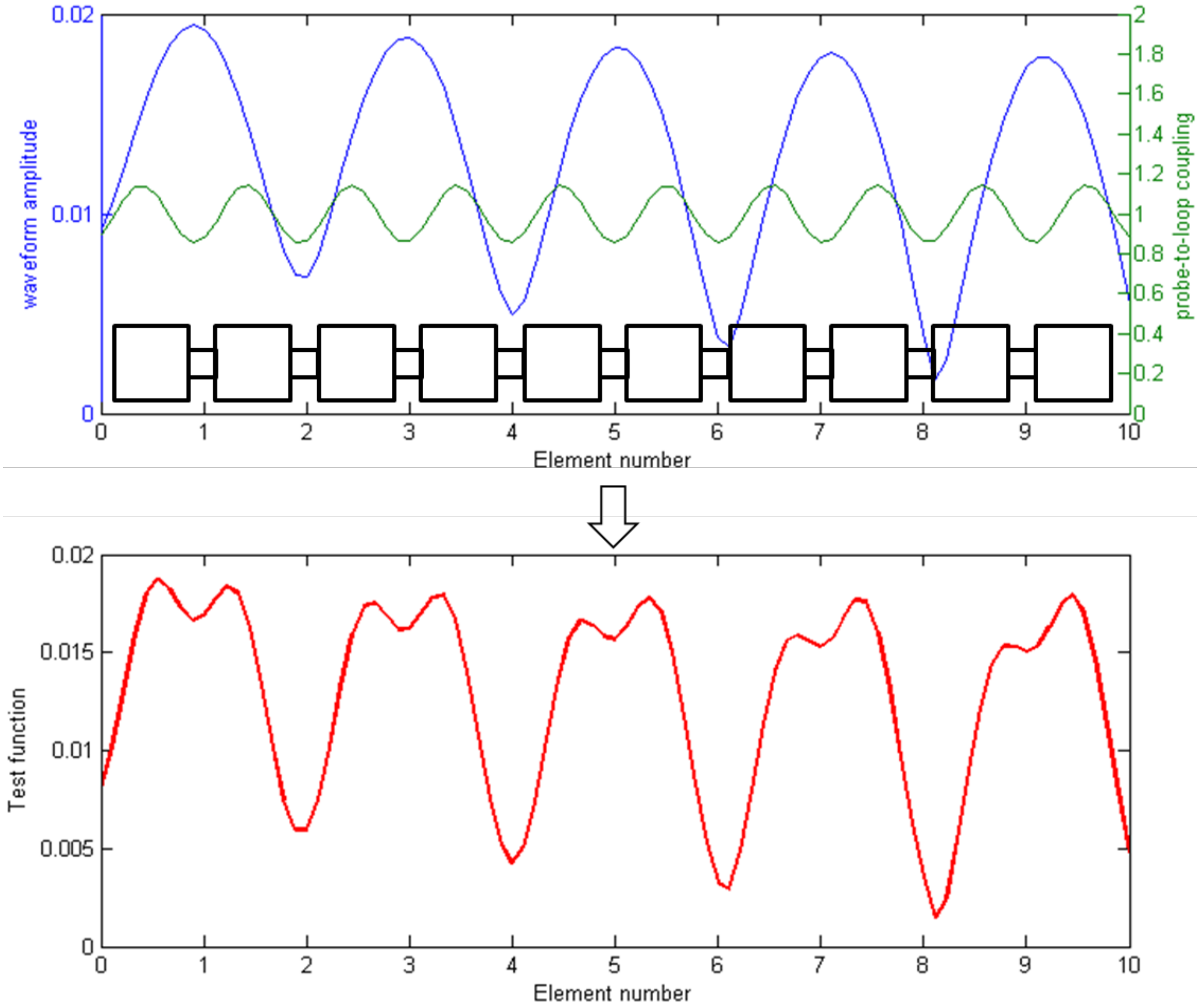

Fig. 4-6 *Construction of test function (bottom red) by the multiplication of a current waveform (blue curve) amplitude and a probe to loop coupling function (green).*

One example is given here to illustrate the use of this fitting method at one frequency. Fig. 4-7 illustrates the induced current measured with a 1-D CCG (C_{mp}= 1 μF) at 75.02 MHz fitted against the current pattern derived from Eq. (4.3). The best fit was found to be $\frac{\alpha d}{\pi} = 3 \times 10^{-3}$ and $\frac{\beta d}{\pi} = 0.48$. It is worth noting again that the fitting was only applied to the last 85 data points. (The first 20 points were not used in order to eliminate the effect of the direct coupling between R_x and T_x.)

This fitting method can be applied to every frequency by following the above procedure. However, the method suffers from very slow computational speed: the calculation at 10 frequencies requires more than 2 hours. The reason for this is that this method is based on χ^2

criteria which require one to find the error between the analytical and the measured values at every single data point (85 in total in this study). Therefore, in this study, this fitting procedure is only applied at frequencies where strong standing wave patterns appeared.

Fig. 4-8 shows the comparison between the predicted and measured dispersion curves of the four structures used as a demonstration in the experiment – three 1-D CCG waveguides with C_{mp} = 100 pF, 1 nF and 1 μF, respectively, and an equivalent-sized MIW structure. The results for the MIW structure and the CCG with C_{mp} = 100 pF are presented in the frequency range 80–120 MHz, while the results for the other two CCG structures with C_{mp} = 1 nF and 1 μF, respectively, are presented in the frequency range 50 kHz–120 MHz.

One should recall that the dispersion curve is predicted by the analytical circuit model as expressed in Eq. (3.7). The passband of the 1-D CCG waveguide shrinks to zero when C_{mp} = C_{cross}, and the value of C_{cross} was predicted to be 99.42 pF for the demonstration structures. Among the three values of C_{mp}, C_{mp} = 1 nF and 1 μF were taken from the predicted forward wave propagation mode where $C_{mp} > C_{cross}$, and C_{mp} = 100 pF was taken around the value of C_{cross}.

One can notice that the measured dispersion curves of the 1-D CCG with C_{mp} = 100 pF do not show obvious matching with the analytical curves shown in Fig. 4-8 (b). The mismatch can be attributed to two possible reasons: (i) capacitance tolerance and (ii) background noise.

(i) Capacitance tolerance

There is a 10% tolerance of the 100 pF coupling capacitor (C_{mp}) component used in the experiment as given in Table 4-1, resulting the capacitance might vary from 90 pF to 110 pF. The dispersion curves change largely with varying C_{mp} when C_{mp} is very close to the value

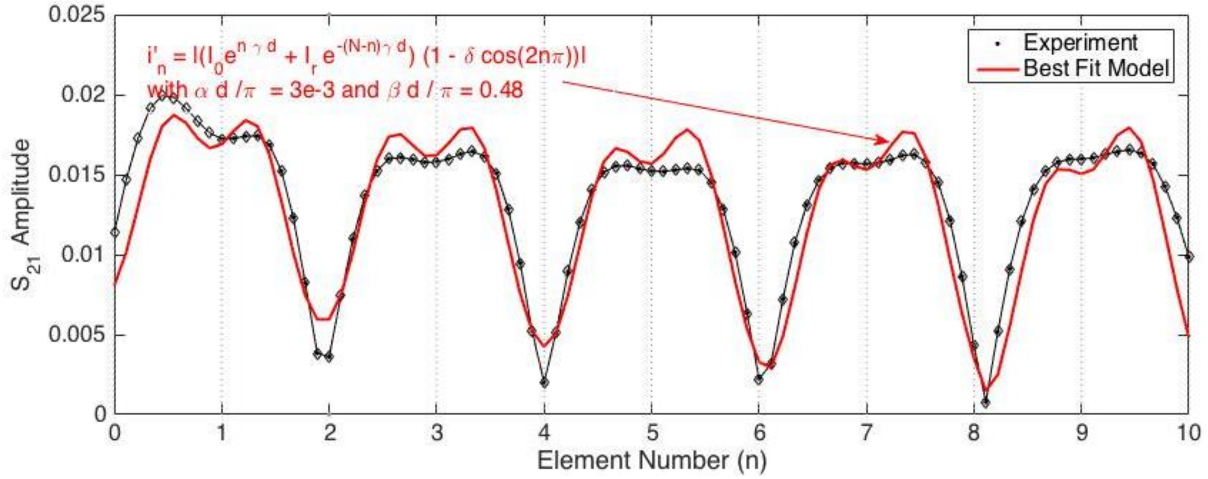

Fig. 4-7 *Best fit wave pattern ($\frac{\alpha d}{\pi}$ =3e–03 and $\frac{\beta d}{\pi}$ = 0.48) for the measured standing wave amplitude pattern in the 1-D CCG C_{mp} = 1 µF case at 75.02 MHz. The first element is represented by dashed lines in order to distinguish it from the elements (second to tenth) that are taken into account.*

of C_{cross}. The measured dispersion curve is found to match more closely with the analytical results produced with C_{mp} = 110 pF, which falls into the variation range.

(ii) Background noise

The 1-D CCG structure built with C_{mp} = 100 pF is very close to the no propagation case so the signal-to-noise ratio can be significantly lower than other cases. When analysing the experimental data, it is hard to distinguish between the wave propagation and the background noise and extract dispersion characteristics precisely.

The other three groups of measured dispersion curves show good agreement with the analytical curves derived from Eq. (3.6). The 1-D CCG waveguide without C_{mp} shows backward wave propagation, while the 1-D CCG waveguide with C_{mp} = 1 nF and 1 µF shows forward wave propagation. One can see that this fitting method provides a satisfactory understanding of the dispersion characteristics of 1-D CCG waveguides.

This method may be rather useful when the measurement set-up is rather coarse, for instance when the receiver probe is not placed above the centre of loops to be measured. This method may be less sensitive to measurement misalignments because the calculation uses all the available measured current along the line and find the best fit based on a χ^2 criteria.The disadvantage of this fitting method is that dispersion characteristics at only a limited number of frequencies can be extracted from experiments due to the constraints of computational speed.

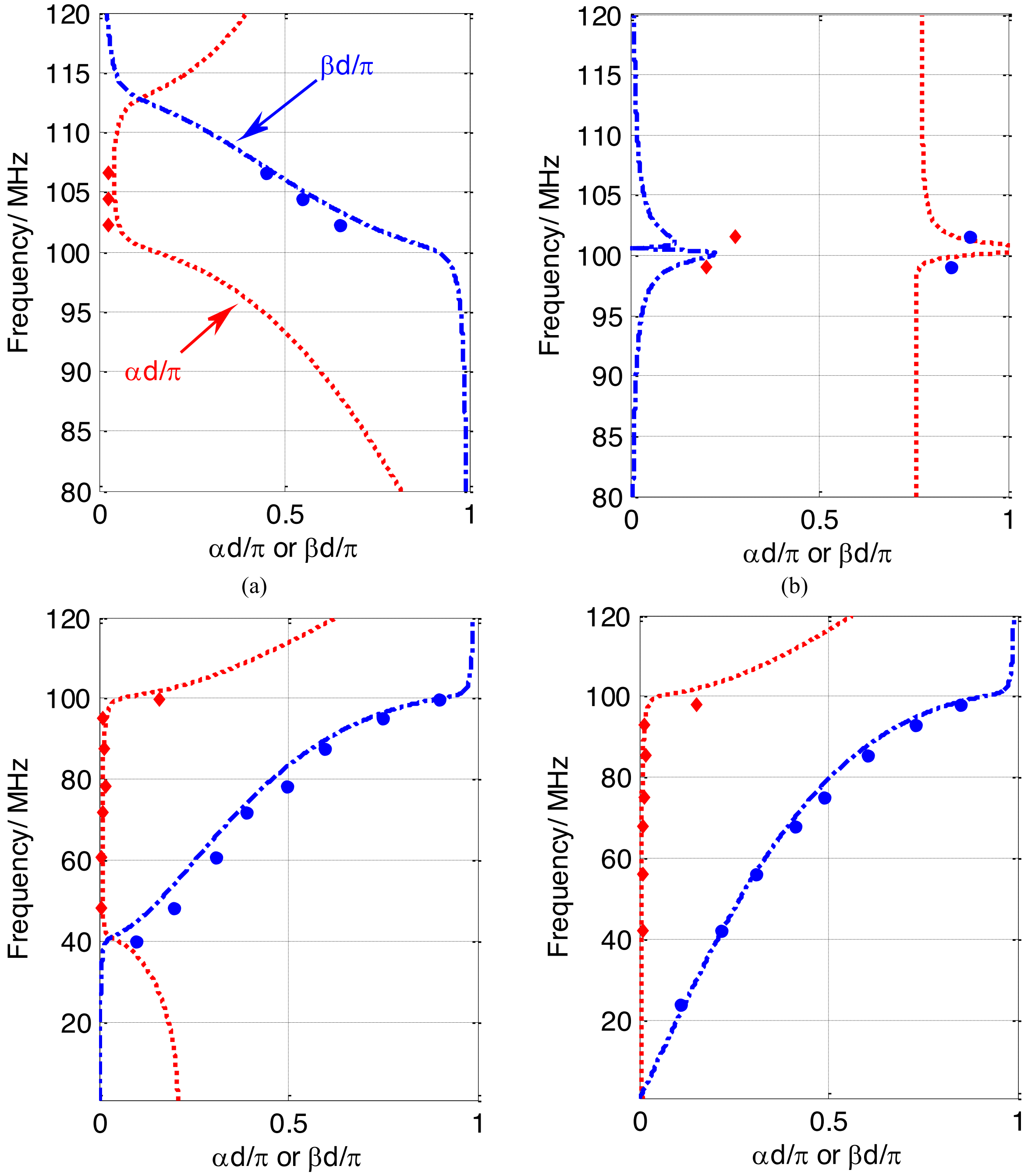

(a) (b)

(c) (d)

Fig. 4-8 *Comparisons between analytical and measured dispersion curves of an MIW in (a); and a 1-D CCG waveguide with* C_{mp} *= 100 pF, 2 nF and 1 μF in (b), (c) and (d), respectively. The predicted* $\alpha d/\pi$ *is represented by the red dotted lines and the predicted* $\beta d/\pi$ *is represented by the blue dashed-dotted lines. The dispersions extracted from the measurements are represented by dots in the corresponding colours.*

4.3.2 Explicit Derivation Method

In order to overcome the constraint of the fitting method discussed in Section 4.3.1, a different method, referred to as the 'explicit derivation method', is applied to extract dispersion characteristics from experimental data.

This explicit derivation method, established in [68], is based on an explicit relationship between the dispersion characteristics α and β and any three neighbouring currents of the 1-D waveguide. Eq. (4.4) gives a simple expression illustrating the principle of this method:

$$\cosh((\alpha + j\beta\,)d) = \frac{i_{n+1} + i_{n-1}}{2i_n} \tag{4.4}$$

where i_n, the current circulating in the n^{th} major loop, can be expressed as Eq. (4.5):

$$i_n = I_o e^{-n\gamma d} + I_r e^{-(N-n)\gamma d} \tag{4.5}$$

Compared with the fitting method described in Section 4.3.1, this explicit derivation method offers the benefits of fast computation speed since only three data points are required to get a pair of α and β at one frequency. Therefore, the dispersion characteristics α and β may be readily extracted for every frequency – there are 1601 frequency points measured in the range 50 kHz–150 MHz.

This explicit derivation method is applied to the four demonstration CCG structures – three 1-D CCG waveguides with C_{mp} = 100 pF, 1 nF and 1 µF, respectively, and an equivalent-sized MIW structure. Fig. 4-9 shows the comparison between the extracted dispersion characteristics and the analytical dispersion curves. The results for the MIW structure and the CCG with C_{mp} = 100 pF are presented in the frequency range 80–120 MHz, and the results for the remaining two CCG structures with C_{mp} = 1 nF and 1 μF are presented in the frequency range 50 kHz–120 MHz.

The extracted dispersion characteristics from the first method – the fitting method – are also shown in this figure for comparison.
The explicit derivation method offers the advantage of fast computation speed, so it is applied to extract α and β at every frequency measured in the experiment. This method allows a more detailed observation on the dispersion behaviours in the passband comparing to the fitting method. The values of α and β extracted by the two methods are plotted together for comparison in Fig. 4-9.

In Fig. 4-9 (a), one can notice that the passband extracted by the explicit derivation method shift down compared to the predicted curve, while the results from the fitting method shift up. The frequency shift toward either direction is only about 1 MHz, which is negligible comparing to the resonant frequency of 106.04 MHz. Therefore, the results from both methods can be considered correct. The difference might come from the fact that the fitting method considers an extra fact – the probe-to-loop coupling effect comparing to the explicit derivation method. There are random data points outside the passband due to low signal-to-noise ratio.

Fig. 4-9 (b) shows that both methods are not able to extract the dispersion characteristics. The two possible reasons for such a mismatch between the extracted data and the analytical prediction are given in Section 4.3.1. The dominant reason can be the low signal-to-noise ratio when no-propagation point is about to be achieved.

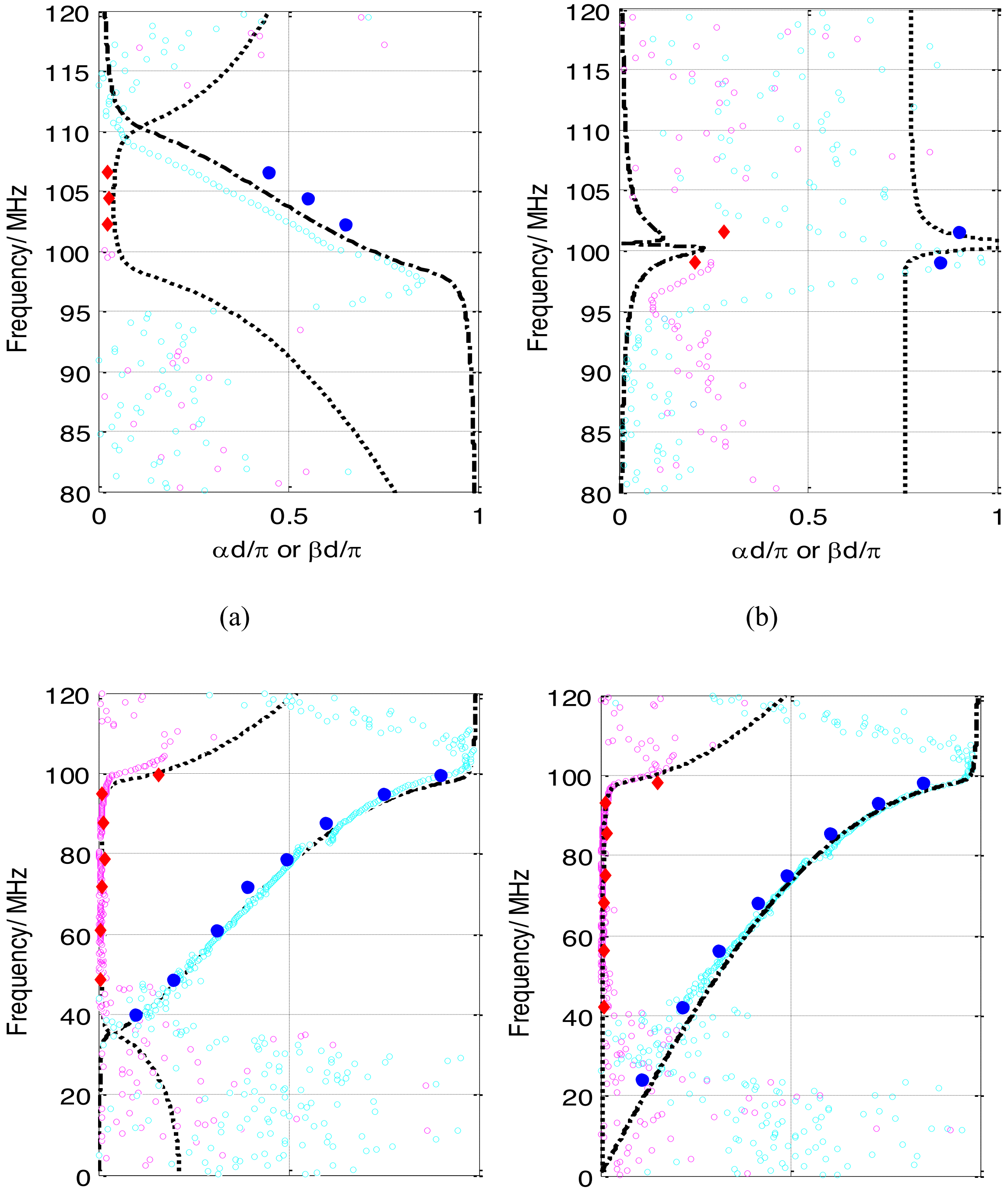

(a) (b)

(c) (d)

Fig. 4-9 *Comparisons between dispersion curves from the explicit derivation method, the waveform fitting method and the analytical value for an MIW in (a); and for a 1-D CCG waveguide with C_{mp}= 100 pF, 2 nF and 1 μF in (b), (c) and (d), respectively. The predicted $\alpha d/\pi$ is represented by the black dotted lines and the predicted $\beta d/\pi$ is represented by the black dashed-dotted lines. The results of the explicit derivation method for $\alpha d/\pi$ and $\beta d/\pi$ are represented by magenta circles and cyan circles, respectively, and the dispersion values extracted from the waveform fitting method are represented by the red diamonds and blue spheres for $\alpha d/\pi$ and $\beta d/\pi$, respectively.*

There is an important phenomenon which the fitting method fails to present but clearly presented by the explicit derivation method. In Fig. 4-9 (c) and (d), the values of α and β extracted by the explicit derivaition method does not show evidence of wave propagation in the lower parts of the predicted passbands. More specifically, for a CCG built with C_{mp}= 2 nF and 1 μF, the predicted lower edge of their passbands are 32 MHz and 2 MHz respectively; however, the experimentally extracted values of α and β show that the lower cut-off frequencies are roughly 45 MHz and 40 MHz respectively in the two cases. There are only random data points below these lower cut-off frequencies.

Why the measured passbands is narrower comparing to the analytical values? In order to answer this question, one shall examine the different between the experimental set-up and the analytical model. In the experiment, the power is injected into a CCG waveguide via magnetic coupling between the non-resonant transmitter probe T_x and the structure. The non-resonant T_x probe is connected to a VNA whose characteristic resitance is 50 Ω. The analytical model derives the dispersion equation based on the circuit model of the waveguide itself, which does not consider the T_x probe and the 50 Ω resistance it connected with.

Fig. 4-10 (a) and (b) shows the reflection coefficient between the T_x probe and CCG waveguides built with C_{mp}= 2 nF and 1 μF respectively. The reflection coefficient is the ratio between the complex magnitude of the reflected wave to that of the incident wave.

One can see from Fig. 4-10 (a) and (b) that the reflected power ratio rapidly increases as frequency decreases in the passband in both cases.

For the CCG built with C_{mp}= 2 nF, its measured lower cut-off frequency is around 45 MHz, and this frequency is about where the lowest resonance happen. One can read from

Fig. 4-10 (b) that the reflection coefficient at the lowest resonance peak is -0.05 dB. This means that 99.43% of the power is reflected back to the source.

For the CCG built with C_{mp}= 1 μF, its measured lower cut-off frequency is around 40 MHz, and this frequency is about where the second lowest resonance happen. One can read from Fig. 4-10 (a) that the return loss at the lowest resonance peak is -0.2 dB. This means that 97.72% of the power is reflected back to the source.

For frequencies lower than these measured lower cut-off frequencies, one can see that the reflection coefficient is approaching to zero as frequency decreases, so there is nearly no power injected into the waveguide due to the mismatch between the source and the waveguide. This explains why the measured passband is actually narrower than the analytical one.

The measured fractional bandwidth of the CCG waveguide built with C_{mp}= 1 μF is 85.7%. This value is much smaller than the fractional bandwidth of the analytical passband 192.4%; however it still largely exceeds the 20% requirement of UWB channels.

Fig. 4-11 (a) and (b) shows the input impedance calculated for the two CCG cases respectively. When frequency is below the measured lower cut-off frequencies, one can notice that the imaginary part of the input impedance diverge rapidly, while the real part of the input impedance stays very close to zero. The non-resonant T_x connected to a 50 Ω characteristics resistance from the VNA can only provide purely real impedance, and hence cannot achieve impedance matching with the input impedance of the waveguide, under the maximum power transfer theorem.

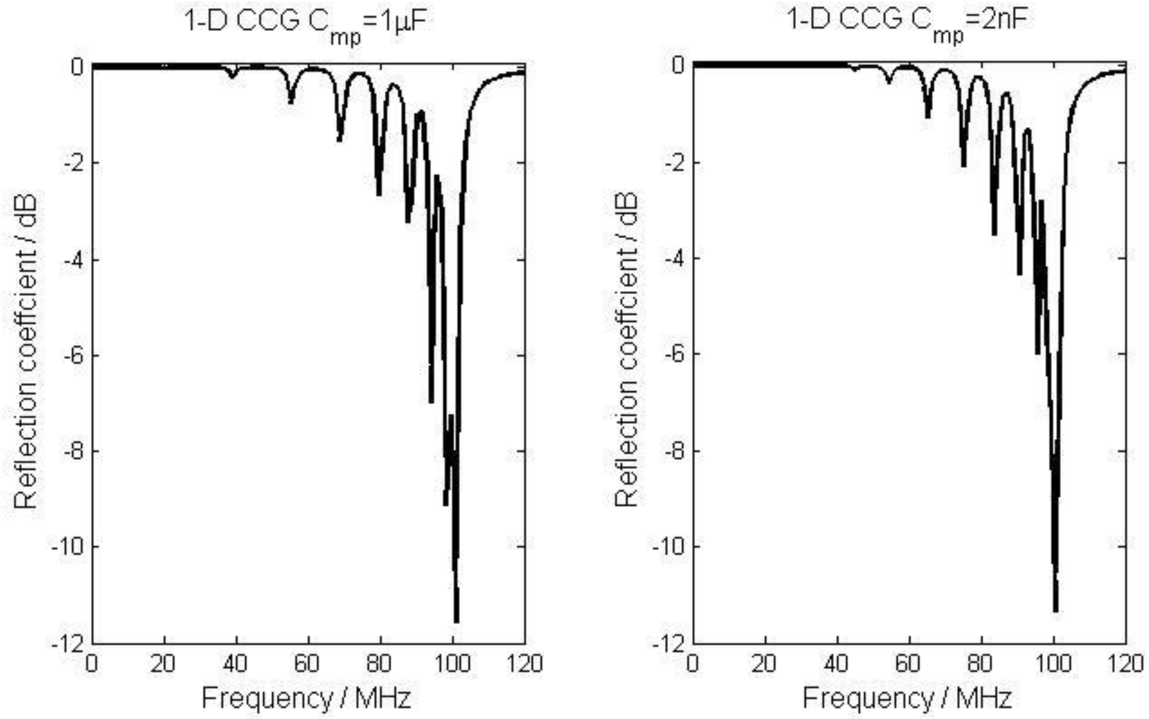

(a) (b)

Fig. 4-10 *Return loss between the Tx probe and CCG waveguides when (a) C_{mp}= 2 nF and (b) 1 μF.*

The rapid divergence of the imaginary impedance makes it difficult to design a transmitter whose impedance matches to the waveguide input impedance in the entire passband. Therefore, channelization can be applied to get multiple sub-channels and impedance matching can be achieved in each sub-channel.

This study focuses on the characterization of CCG waveguides, so there is no further discussion on the matching condition between the transmitter and the waveguide. This topic is very essential when applying CCG waveguides for contactless data transfer applications and should be addressed in future studies.

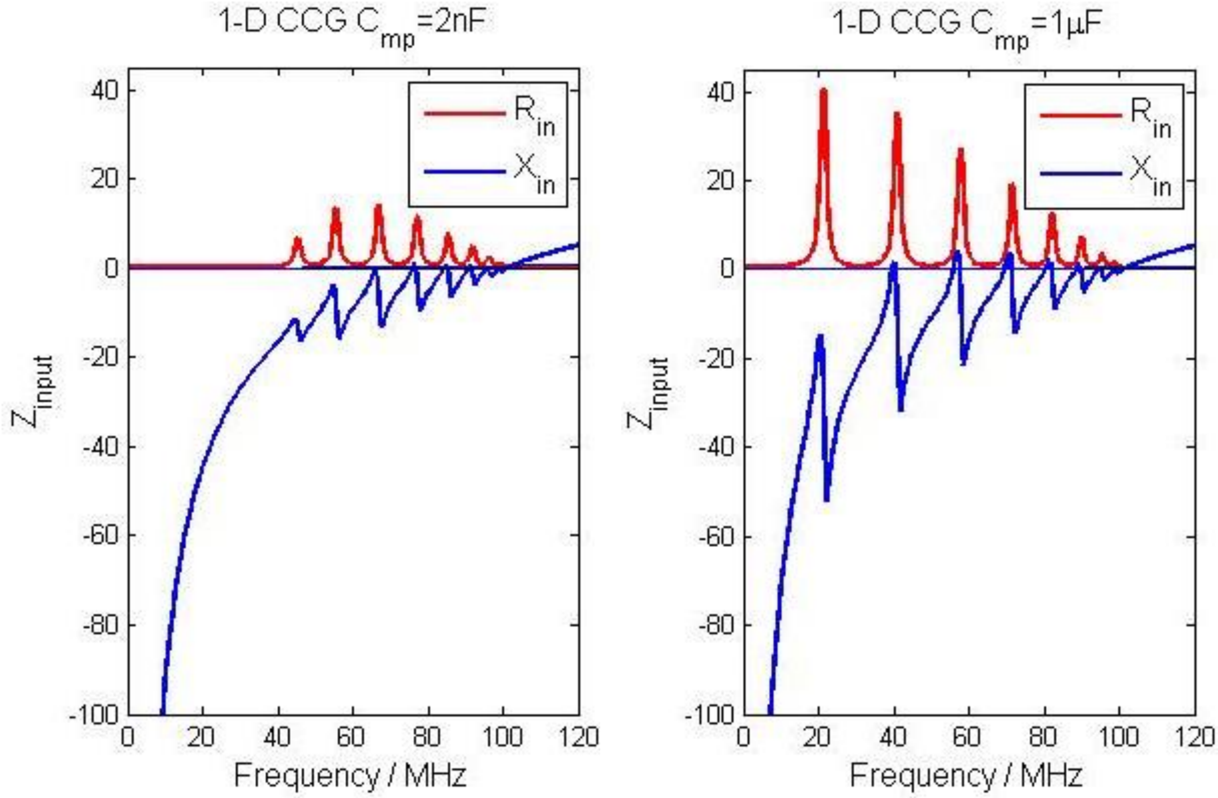

(a) (b)

Fig. 4-11 *Input impedance of CCG waveguide when (a) C_{mp}= 2 nF and (b) 1 μF.*

4.4 Conclusions

In this chapter, four demonstration structures were constructed and a simple experiment was conducted to verify the analytical model. The dispersion characteristics, both α and β, are extracted from measured wave patterns by two different methods – the fitting method and the explicit derivation method.

The fitting method is proposed in this study, which considers the analytical waveform as a superposition between the spatial variation of probe-to-loop coupling and the wave-like current along the structure. This fitting method suffers from slow computational speed. However, this method may be rather useful when the measurement set-up is coarse, for instance when the receiver probe is not placed exactly above the centre of loops to be measured. This method may be less sensitive to measurement misalignments because the calculation uses all the available measured current along the line and find the best fit based on a χ^2 criteria.

The explicit derivation method is originally proposed in [68] and offers the benefits of explicit relation between current and dispersion characteristics, and fast computation speed. This method is applied to CCG demonstration structures in order to observe their dispersion behaviours in more detail. This method shows that the measured passbands is narrower than the analytical ones. This phenomenon is analysed with the aid of reflection coefficient. It is shown that almost all the power is reflected back to the source at these frequencies. This mismatch between the source and the waveguide results that the power cannot be efficiently injected into the waveguide.

The analytical passband predicted for the demonstration structure built with 1μF is 192.4%; however, due to this inefficient power injection, the measured passband is only around 87.5%. This value has already largely exceeded the requirement of UWB channels.

There is a brief discussion about how to achieve efficient power injection in the passband by matching the transmitter with the waveguide. It is shown that the input impedance of a CCG waveguide has a rapidly diverging imaginary part. Connecting a non-resonant transmitter to a standard source can only offer resistance, so the impedance of the transmitter is purely real. Therefore, resonant transmitter should be investigated under the maximum power transfer theorem in future studies.

The rapid divergence of the imaginary impedance makes it difficult to design a transmitter whose impedance matches to the waveguide input impedance in the entire passband. Therefore, channelization can be applied to get multiple sub-channels and impedance matching can be achieved in each sub-channel.

CHAPTER 5

TWO-DIMENSIONAL CAPACITOR-CONNECTED GRIDS

Following the discussion of 1-D CCGs in previous chapters, it would be logical to proceed to two-dimensional CCG structures. A 2-D CCG waveguide would provide a multipath communication channel and allow it to be shared between multiple terminals. One would also expect that a 2-D CCG structure gives a greater bandwidth performance compared to its 1-D counterpart, in a similar fashion to MIW structures, as given by Eq. (2.15).

In Section 5.1, the structure of a 2-D CCG waveguide surface will be investigated, and its dispersion equation will be derived in Section 5.2; a 2-D demonstration structure will be introduced in Section 5.3; the dispersion characteristics on selected transmission paths along the 2-D surface will be discussed in Section 5.4; Section 5.5 presents a simple experimental setup, which will be used for experimental verification of dispersion characteristics as described in Section 5.6; and Section 5.7 presents the analytical prediction and measurement of the current distribution over a 2-D surface with the aid of the impedance matrix derived in Section 3.8.

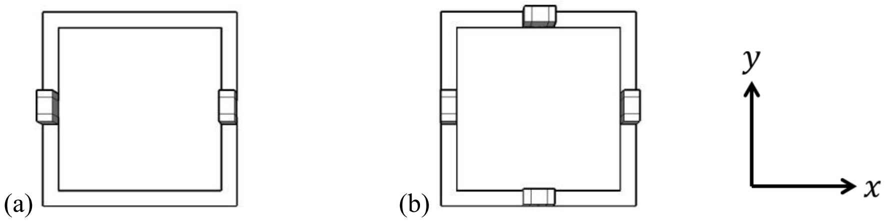

Fig. 5-1 *The structure of (a) a 2C metallic loop, which is only expandable in the* x *direction, and forms a 1-D CCG waveguide; (b) a 4C metallic loop, which is expandable in both the* x *and* y *directions and can be used to form a 2-D CCG waveguide surface.*

5.1 2-D Capacitor-Connected Grids

One is reminded that a 1-D CCG structure (Fig. 3-1 (a)) is a ladder circuit made of metallic loops interlinked by electric coupling devices. A metallic loop in a 1-D CCG is as given in Fig. 5-1 (a), which is loaded with two gap capacitors, one on each of its two vertical sides. Current circulation in such a metallic loop can generate a potential difference across the two gap capacitors, and the potential difference can be passed on to adjacent metallic loops via electric coupling devices in between.

In order to build a 2-D CCG waveguide surface, a small change has to be made to the structure of the metallic loop, enabling it to be expandable in both the x and y directions. The new structure of the metallic loop is as shown in Fig. 5-1 (b), which is loaded with gap capacitors on all four branches – two vertical ones and two horizontal ones. For convenience, one will name the previously reported metallic loop as the '2C metallic loop', as each contains two gap capacitors, and refer to the newly constructed metallic loop as the '4C metallic loop', as each one contains four gap capacitors.

Fig. 5-2 (a) shows the 4×4 array of a 2-D CCG waveguide surface, in which the 4C metallic loops are interlinked by coupling capacitors in both the x and y directions, and its 1-D counterpart is presented in Fig. 5-2 (b).

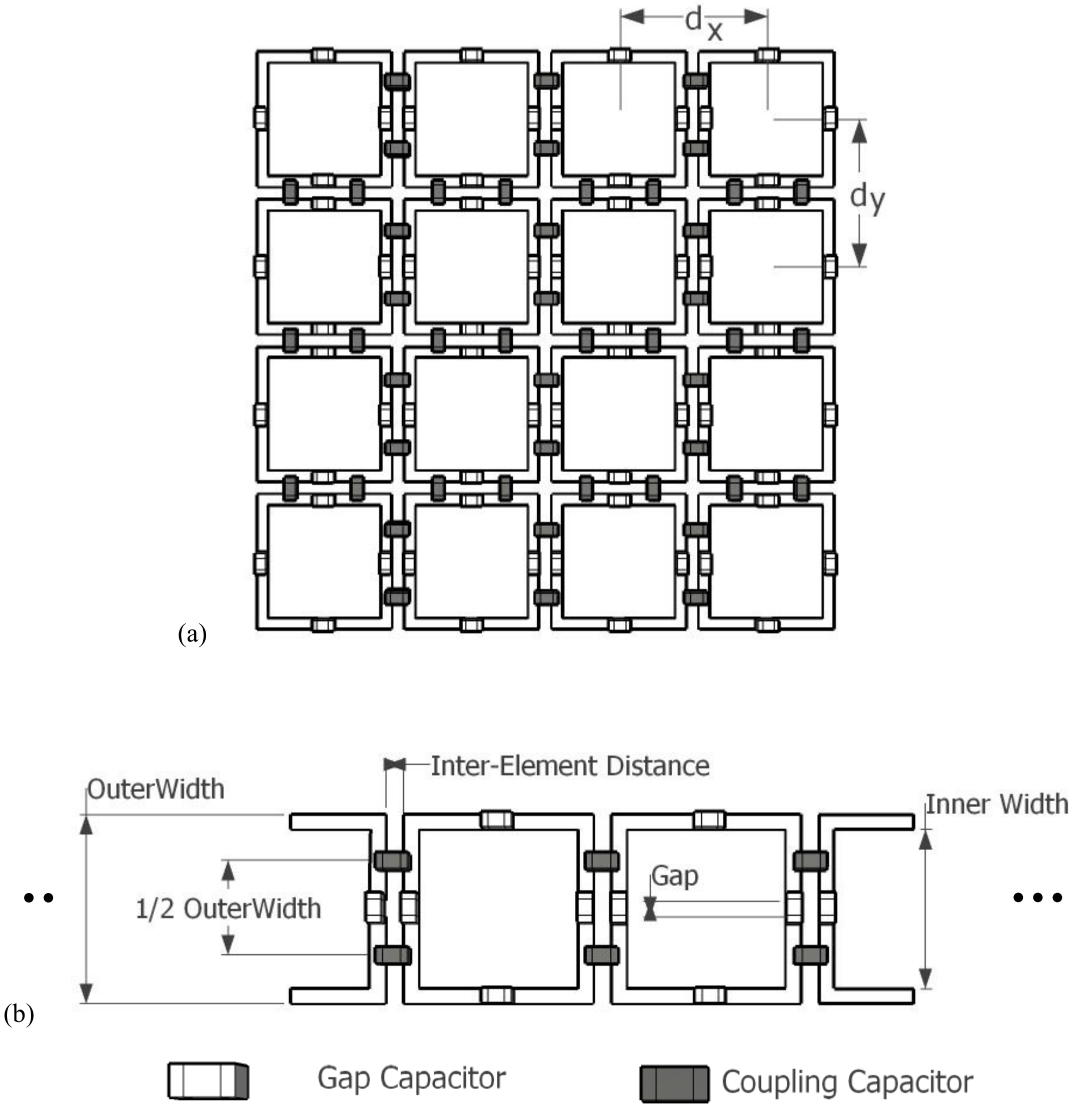

Fig. 5-2 *(a) Surface of the 2-D CCG waveguide; (b) surface of the 1-D counterpart; both are built with 4C metallic loops of the same dimensions as given in Table 3-1.*

For the purposes of differentiation, one can name the 1-D array built with 2C metallic loops (Fig. 3-1 (a)) as a 1-D 2C CCG, while the one made with 4C metallic loops (Fig. 5-2 (b)) is referred to as a 1-D 4C CCG.

5.2 Derivation of Dispersion Equation for 2-D CCG Structures

2-D CCG waveguide surfaces support the propagation of two types of wave: one is the surface wave travelling along the edge, the other is the MI and EI waves propagating inside the surface in a similar fashion to 1-D CCG structures.

In order to derive the dispersion equation for 2-D CCG structures, one must first understand the different coupling mechanisms supporting the propagation of the two types of wave. Fig. 5-3 shows the different coupling mechanisms for elements positioned either along the edge or inside the surface, where M describes magnetic coupling between adjacent major loops, M_{minp} describes magnetic coupling between a pair of adjacent major and minor loops, and M_{diag} describes magnetic coupling between diagonally adjacent major loops. The nearest-neighbour approximation, verified in [63], is applied here for simplicity. The magnetic coupling between coalesced major and minor loops M_{minp} is neglected as justified in Section 3.3. A major loop positioned along the edge is coupled to three adjacent major loops, two diagonally adjacent major loops and three coalesced minor loops, while a major loop positioned inside the surface is coupled to four adjacent major loops, four diagonally adjacent major loops and four coalesced minor loops.

One can recall that the dispersion equation of 1-D CCG structures was derived by circuit analysis under the quasi-static approximation [92]. Using a similar analysis for a 2-D array (Fig. 5-2 (a)), one arrives at the relationship for a 2-D CCG waveguide surface, as expressed by Eq. (5.1):

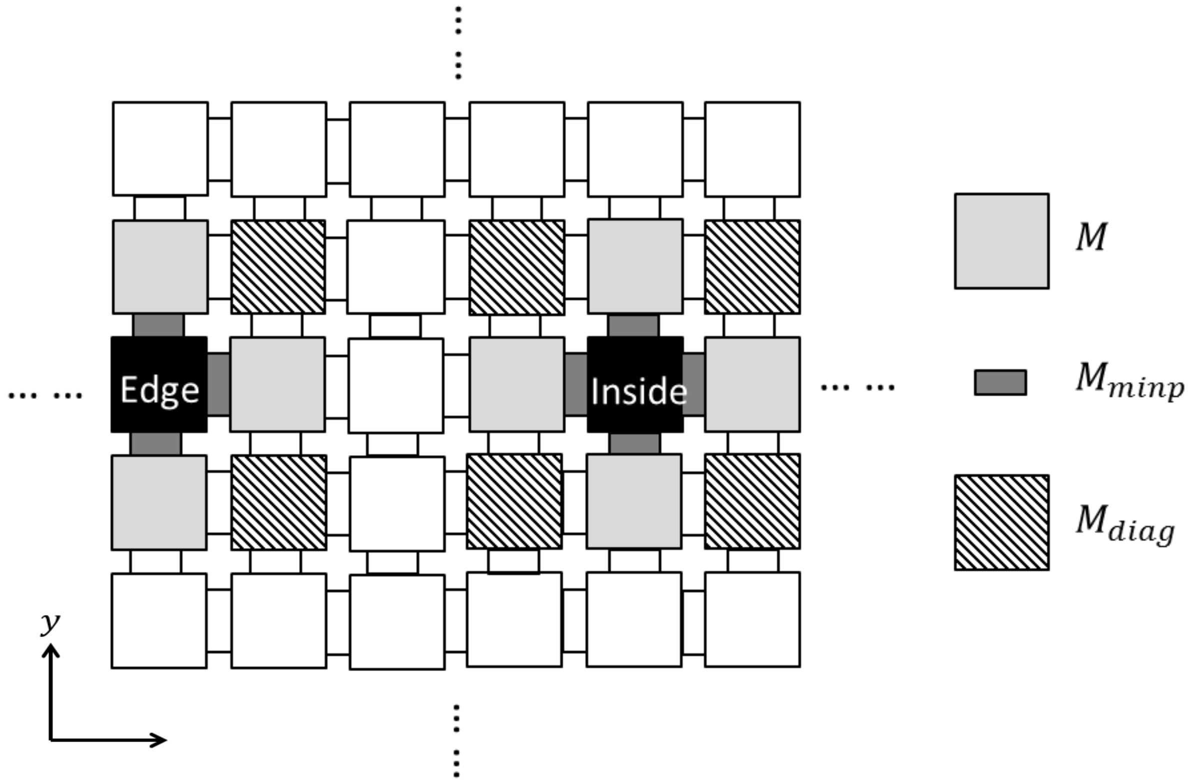

Fig. 5-3 *Illustration of coupling mechanism for elements positioned either along the edge or inside the surface*

.

$$
\begin{aligned}
Z_{minp}[Z_{maj} + M\big(A_x e^{j\gamma_x d_x} + A_{-x} e^{-j\gamma_x d_x} + A_y e^{j\gamma_y d_y} + A_{-y} e^{-j\gamma_y d_y}\big)] \\
+ M_{diag}\big[\big(A_x e^{j\gamma_x d_x} + A_{-x} e^{-j\gamma_x d_x}\big)\big(A_y e^{j\gamma_y d_y} + A_{-y} e^{-j\gamma_y d_y}\big)\big] \\
- (X_{share})^2\big(A_y + A_{-y} + A_y e^{j\gamma_y d_y} + A_{-y} e^{-j\gamma_y d_y}\big) \\
+ \big(A_x + A_{-x} + A_x e^{j\gamma_x d_x} + A_{-x} e^{-j\gamma_x d_x}\big) = 0
\end{aligned}
\tag{5.1}
$$

where d_x and d_y are the periods of the structure in the x and y directions, respectively, as shown in Fig. 3-3 (a), which are the distances between the centres of pairs of adjacent major loops (a symmetric 2-D structure is considered here, in which the array periods in the two directions are the same ($d_x = d_y$)); γ_x and γ_y are the propagation constants along the x and y directions (the propagation constant $\gamma = \alpha + j\beta$, where β and α are the wave number and attenuation constant, respectively); some variables share the same definitions as the ones in the dispersion equation of 1-D 2C CCGs, as presented in Section 3.1, including the magnetic coupling between adjacent major loops M; the minor loop impedance $Z_{minp} =$

$R + j\omega L + \frac{2}{j\omega C_{gap}} + \frac{2}{j\omega C_{mp}}$, the shared impedance between adjacent major and minor loops $X_{share} = \frac{R}{2} + \frac{j\omega L}{2} + \frac{1}{j\omega C_{gap}}$; however, the major loop impedance has to be redefined as $Z_{maj} = 4R + 4j\omega L + \frac{4}{j\omega C_{gap}}$, as each 4C metallic loop contains four gap capacitors rather than two. Here, one can recall from Section 3.2 that R and L are the resistance and inductance, respectively, associated with each side of a major loop, ω is the angular frequency of wave propagation, C_{gap} is the gap capacitance, and C_{mp} is the parallel coupling capacitance.

The four parameters A_x, A_{-x}, A_y and A_{-y} equate to either zero or one and are used to distinguish wave types and travelling paths. To describe MI and EI waves travelling inside the waveguide surface, $A_x = A_{-x} = A_y = A_{-y} = 1$; to describe surface waves travelling along one of the four edges, one among the four parameters is set to zero as the missing neighbouring coupling on one side. For example, $A_x = 0$ and $A_{-x} = A_y = A_{-y} = 1$ when describing the surface wave propagating along the leftmost edge path, while $A_y = 0$ and $A_x = A_{-x} = A_y = 1$ when describing the surface wave propagating along the uppermost edge path.

One can generate dispersion equations for a 2-D CCG waveguide surface from Eq. 4-1 by substituting a proper value of A_x, A_{-x}, A_y and A_{-y} for different wave paths.

5.3 Demonstration Structure

In order to characterize the dispersion behaviours of 2-D CCGs (Fig. 5-2 (a)), a simple demonstration structure was constructed by interlinking a chain of 4C metallic loops (Fig. 5-1 (b)) with coupling capacitors C_{mp} soldered across inter-element gaps in both the x and y directions. A 4C metallic loop shares the same dimensions as a 2C metallic loop, as given in

Table 3-1, but has gaps not only on the two perpendicular arms but also on the two horizontal arms of each loop.

For the 2-D demonstration structure, M_{diag} was predicted to be –0.256 nH by FastHenry simulation [95], C_{gap} was chosen as 220 pF and C_{mp} was chosen as 1 μF.

The structural parameters of the 2-D CCG demonstration structure are summarized in Table 5-1.

Table 5-1 *Inductive, resistive and capacitive parameters of the 2-D CCG demonstration structure*

Parameters	**Values**
M	–1.19 nH
M_{diag}	–0.256 nH
R	0.05 Ω
L	5.12 nH
C_{mp}	1μF
C_{gap}	220 pF

5.4 Dispersion Characteristics Analysis

Based on the dispersion relationships given by Eq. (5.1), one can explore the dispersion characteristics of the two types of waves propagating in 2-D CCG structures – surface waves travelling along the edges and MI and EI slow waves propagating inside the waveguide surface. The latter type of wave can propagate in a 2-D CCG structure along multiple paths, among which, two special cases are considered here: (1) waves propagating along the diagonal of a 2-D waveguide surface where $\gamma_x a_x = \gamma_y a_y$, and (2) waves propagating along a straight line along either x or y axial direction across a 2-D waveguide surface where $\gamma_x a_x$ or $\gamma_y a_y = 0$. For convenience, the three wave paths are named as 'edge path', 'diagonal <11> path' and 'axial <01/10> path', respectively.

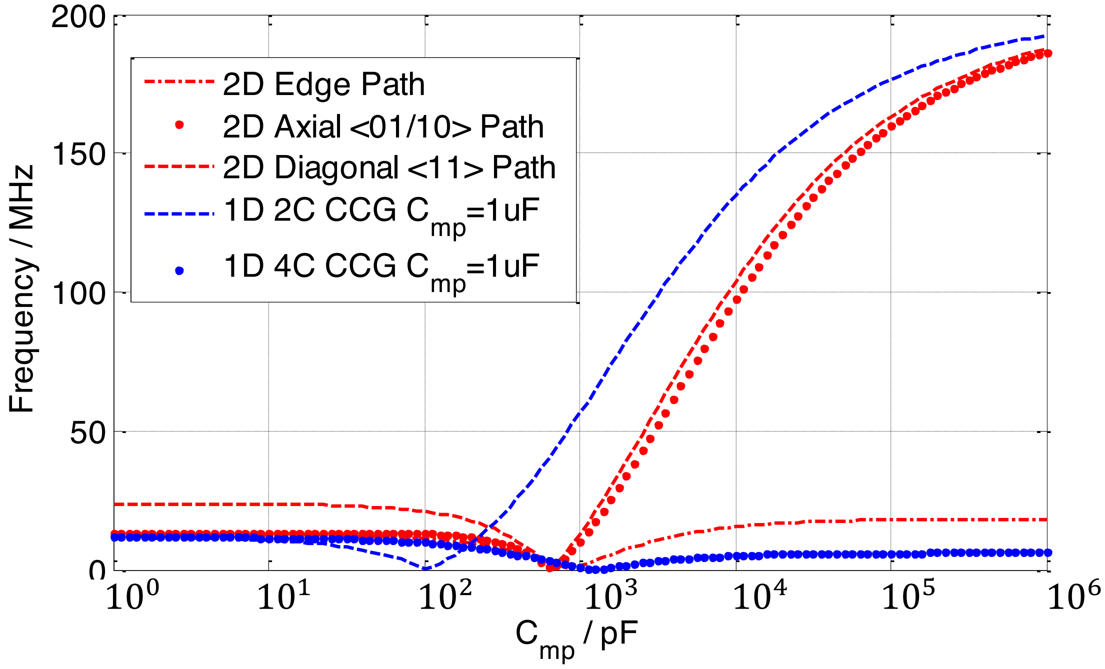

Fig. 5-4 *Fractional bandwidth of a 2-D CCG structure with C_{mp} ranging from 1 pF to 1 μF, along with results for an equivalent-sized 1-D 2C CCG and 1-D 4C CCG for comparison.*

In a similar fashion to the study on 1-D CCGs, one can explore how the available bandwidth of a 2-D CCG structure changes with electric coupling strengths by virtue of varying coupling capacitance C_{mp}. Fig. 5-4 shows the fractional bandwidths achieved by waves travelling along the three above-mentioned paths in the 2-D CCG demonstration structure built with C_{mp} varying from 1 pF to 1 μF. The results for the 2-D CCG have been presented in comparison with its 1-D counterpart, the 1-D 4C CCG, and a previously studied 1-D 2C CCG.

The metallic loops of the two 1-D devices were built with the same dimensions as the 2-D CCG structure, and shares the same inductive, resistive and capacitive parameters as given in Table 5-1. It is worth noting that the 1-D 4C CCG and the 1-D 2C CCG use the same coupling capacitance (C_{mp} = 1 μF) as the 2-D demonstration structure; however, the gap capacitance C_{gap} is 110 pF in the 1-D 2C CCG, which is half of that used in the 1-D 4C CCG

Table 5-2 *No-propagation points ($C_{mp} = C_{cross}$) found for the three 2-D paths, respectively, in comparison with results for the 1-D 4C CCG and the 1-D 2C CCG*

Propagation Paths	**No-Propagation Point (C_{cross})/pF**
Edge Path	874.98
Axial <01/10> Path	657.66
Diagonal <11> Path	657.66
1-D 2C CCG	52.48
1-D 4C CCG	1273.50

and 2-D structures in order to ensure that they share the same major loop resonant frequency (f_{maj} = 150 MHz).

One important feature of the 1-D CCG is the appearance of a no-propagation point where the positive and negative coupling exactly cancel each other. Fig. 5-4 shows that the 2-D CCG structure exhibits the same behaviour: when C_{mp} increases, the passbands of the three 2-D paths decrease until they shrink to zero at the no-propagation point and keep expanding once C_{mp} goes above the no-propagation point.

Table 5-2 shows the no-propagation points (noted as $C_{mp} = C_{\mathrm{cross}}$) found for the three 2-D paths, respectively, in comparison with results for the 1-D 4C CCG and the 1-D 2C CCG. The axial <01/10> path and the diagonal <11> path share the same no-propagation point (C_{cross}= 657.66 pF), which can be attributed to the same coupling condition of the two paths.

Previous studies of the MIW show that a 2-D MIW structure will have significantly greater bandwidth than a 1-D device [63]. One can expect to see such bandwidth improvement from dimension expansions on CCG structures. Table 5-3 presents the fractional bandwidths achieved by the three 2-D paths when C_{mp} = 1 μF, in comparison with results calculated for the 1-D 4C CCG and the 1-D 2C CCG.

***Table 5-3** Fractional bandwidth calculated at C_{mp} = 1 μF for the three 2-D paths, in comparison with results for the 1-D 4C CCG and the 1-D 2C CCG*

Propagation Paths	**FBW (C_{mp} = 1 μF)/%**
Edge Path	18.19
Axial <01/10> Path	186.4
Diagonal <11> Path	187.6
1-D 2C CCG	194.5
1-D 4C CCG	6.168

As shown in Table 5-3, the axial <01/10> path and the diagonal <11> path in the 2-D CCG demonstration structure provide much wider bandwidth than its 1-D counterpart, the 1-D 4C CCG. The edge path in a 2-D structure can essentially be considered as a 1-D CCG array, as it carries surface waves confined only to surface edges. This explains why the edge path in the 2-D CCG demonstration structure offers similar bandwidth performance to a 1-D 4C CCG.

One interesting finding is that the 1-D 2C CCG provides even better bandwidth performance compared with any of the propagation paths in the 2-D CCG, and this makes it a better solution for achieving high bandwidth. As shown in Table 5-3, the 1-D 2C CCG with C_{mp}= 1 μF gives FBW = 194.2%, while a 1-D 4C CCG built with the same C_{mp} only gives FBW = 6.168%. The two 1-D devices have identical magnetic coupling strengths as they were built with the same dimensions. It is logical to consider the difference in electric coupling strengths in the two 1-D cases to explain why including two or four capacitors in each major loop makes such a significant difference in bandwidth performance.

One can consider electric couplings in the 1-D 2C CCG and 1-D 4C CCG with the aid of a four-electrode model. Table 5-4 presents the two cases with the four-electrode model, calculating their electric coupling coefficient k_e (Eq. (3.42)).

One can simplify the expression for k_{e_4c} to k_{e_2c} multiplied by a factor of $\left(2C_{gap}+C_{mp}\right)/(6C_{gap}+5C_{mp})$. This factor is always smaller than one and keeps decreasing when C_{mp} increases. This factor approaches to 0.2 when $C_{mp} \gg C_{gap}$. Therefore, one can easily tell that electric coupling strength in a 2C case is always greater than that of the 4C case, which explains the difference in available bandwidth provided by the two becomes greater when C_{mp} increases.

The comparison between 2C and 4C CCG structure can also be understood from a waveguide point of view. A 1-D 2C CCG waveguide with $C_{mp} \gg C_{gap}$ can be considered as a transmission line which has extremely large bandwidth. Based on this understanding, the two extra gap capacitors C_{gap} in a 1-D 4C CCG can be considered as filters added in a transmission line, and therefore result in reduced passband.

The 2-D CCG waveguide surface is considered as a potential candidate for multipath data-carrying devices, so it is important to consider the effects of dispersion on signals propagating along various paths.

Fig. 5-5 shows a comparison of the group velocity dispersion and attenuation of the diagonal <11> path, axial <01/10> path and edge path in the 2-D CCG demonstration structure with results for its 1-D counterparts, the 1-D 4C CCG and the 1-D 2C CCG.

***Table 5-4** Comparison of the circuit model and impedance matrix between the 1-D 4C CCG and the 1-D 2C CCG*

Structure	**1-D 4C CCG**	**1-D 2C CCG**
Four-Electrode Model	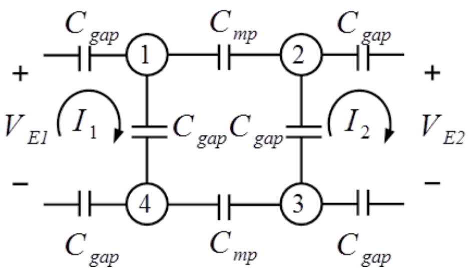	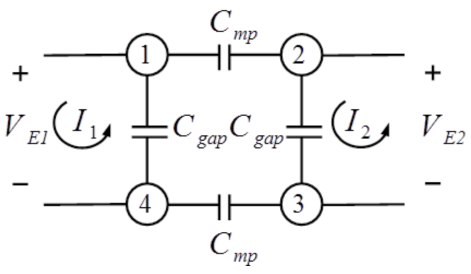
Impedance Matrix	$C_{res\_4c} = \dfrac{\left(\dfrac{C_{self}^2 - C_{meff}^2}{C_{self}}\right)\left(\dfrac{C_{gap}}{2}\right)}{\left(\dfrac{C_{self}^2 - C_{meff}^2}{C_{self}}\right) + \left(\dfrac{C_{gap}}{2}\right)}$ $K = \dfrac{C_{self}^2 - C_{meff}^2}{C_{meff}}$ $C_{self} = C_{gap} + \dfrac{C_{mp}}{2}$ $C_{meff} = \dfrac{-C_{mp}}{2}$	$C_{res\_2c} = \dfrac{C_{self}^2 - C_{meff}^2}{C_{self}}$ $K = \dfrac{C_{self}^2 - C_{meff}^2}{C_{meff}}$ $C_{self} = C_{gap} + \dfrac{C_{mp}}{2}$ $C_{meff} = \dfrac{-C_{mp}}{2}$
Electric Coupling Coefficient $\mathrm{k}_e = \dfrac{2C_{res}}{K}$	$\mathrm{k}_{e\_4c} = \dfrac{2C_{res\_4c}}{K}$ $= \mathrm{k}_{e\_2c}\, \dfrac{(2C_{gap} + C_{mp})}{(6C_{gap} + 5C_{mp})}$ $\approx 0.2\, \mathrm{k}_{\mathrm{e\_2c}}$ when $C_{mp} \gg C_{gap}$	$\mathrm{k}_{e\_2c} = \dfrac{2C_{res\_2c}}{K}$

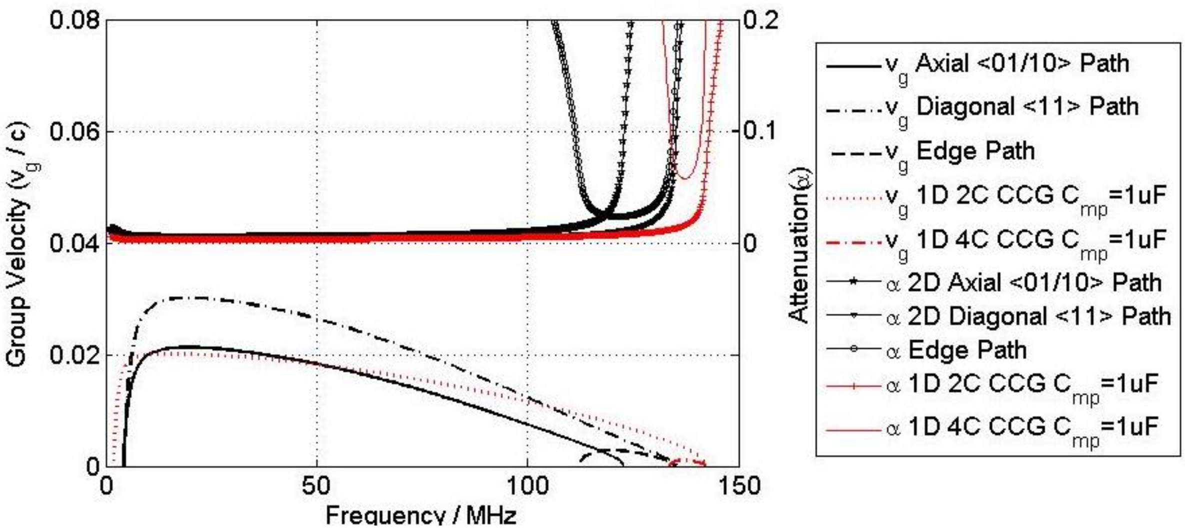

***Fig. 5-5** Comparison of the group velocity dispersion and attenuation of the axial <01/10> path, diagonal <11> path and edge path in the 2-D CCG demonstration structure with results for its 1-D counterparts, the 1-D 4C CCG and the 1-D 2C CCG.*

Table 5-5 shows the peak group velocity v_{gpeak} and bandwidth over a less dispersive frequency range defined by $1 \geq \frac{v_g}{v_{gpeak}} \geq 0.9$ for the three 2-D paths and the two 1-D structures for comparison.

Table 5-6 shows the minimum attenuation values $\alpha_{\min}$ and bandwidth defined by the –3 dB half power points for the three 2-D paths and the two 1-D structures for comparison.

In comparison with the edge path, which carries surface waves, the two inside paths – the axial <01/10> path and the diagonal <11> path – provide a less dispersive and ‘lossy’ propagation channel with significantly greater bandwidth performance. This can be attributed to the fact that an edge path carries surface waves confined only to surface edges, and therefore can essentially be considered as a 1-D CCG array. The two inside paths exhibit comparable dispersion and attenuation performance to a 1-D 2C CCG and provide reasonably good bandwidth performance that largely exceeds the 20% requirement of a UWB channel

[95] and closely approximates to the 200% extreme value. However, neither of the two exceeds the available bandwidth provided by a 1-D 2C CCG.

Table 5-5 *Comparison of group velocity dispersion and bandwidth over a less dispersive frequency range defined by* $1 \geq \frac{v_g}{v_{gpeak}} \geq 0.9$ *for the three 2-D paths and the 1-D 4C CCG and 2C CCG structures*

Path and Waveguide	**Peak Group Velocity** ($\boldsymbol{V_{gpeak}}$**/C**)	**Bandwidth with** $\mathbf{1 \geq \frac{v_g}{v_{gpeak}} \geq 0.9}$ **(MHz)**
Axial <01/10> Path	0.02125	34.40
Diagonal <11> Path	0.03011	37.57
Edge Path	0.0028	8.60
1-D 2C CCG	0.02012	43.21
1-D 4C CCG	0.0010	2.80

Table 5-6 *Comparison of minimum attenuation and bandwidth defined by the –3 dB half power point for the three 2-D paths and the 1-D 4C CCG and 2C CCG structures*

$\boldsymbol{C_{mp}}$	**Minimum Attenuation** ($\boldsymbol{\alpha_{min}}$)	**–3 dB Bandwidth/MHz**
Axial <01/10> Path	0.0047	96.5
Diagonal <11> Path	0.0033	103.5
Edge Path	0.0235	19.2
1-D 2C CCG	0.0032	115.8
1-D 4C CCG	0.0572	7.9

When comparing the two 1-D cases, the 1-D 2C CCG shows improved performance in terms of attenuation, dispersion and bandwidth, and offers great potential to be used as a 1-D contactless data transfer channel.

The 2-D CCG waveguide surface offers the possibility of developing a contactless data transfer channel offering a robust multipath environment for multiple terminal connections. The two inside paths provide good examples of data channels in 2-D CCGs with low loss and dispersion but high data capacity and speed. Channelization could be used to get several sub-channels with less dispersion and group delay, in a similar fashion to the 1-D CCG device.

5.5 Experimental Setup

A simple experimental verification was conducted to verify the analytical dispersion characteristics of the 2-D CCG waveguide surface and to explore frequency-dependent current distributions over the 2-D surface.

A 19×19 2-D CCG waveguide surface of dimensions given in Table 5-1 was fabricated by Quassia Electronics Ltd [99] on an FR4 substrate using photolithography. Each copper loop shared the same track size as the previously reported 1-D demonstration device described in Table 3-1, but included four gaps not only on the two perpendicular arms but also on the two horizontal ones. Surface-mounted ceramic multilayer chip capacitors were soldered across the four track gaps as C_{gap}, and across inter-element gaps as C_{mp}. The values of C_{gap} and C_{mp} were chosen to be 220 pF and 1 μF, respectively. This 2-D device used the same components as the 1-D demonstration structure given in Table 4-1.

Measurements of the 2-D CCG were carried out in a similar manner to that for the 1-D devices. Some repetitious details are omitted here (refer to the introduction given in Chapter 4). A simple illustration of the experimental setup is presented in Fig. 5-6 (a). Fig. 5-6 (b) shows a photograph taken of a corner area of this demonstration structure. Two loop antennas, source antenna T_x and receiving antenna R_x, were employed to provide the source signal and receive the structure's response. Two experimental runs were conducted, in which T_x was placed above the PCB board but on different locations: one with T_x centred

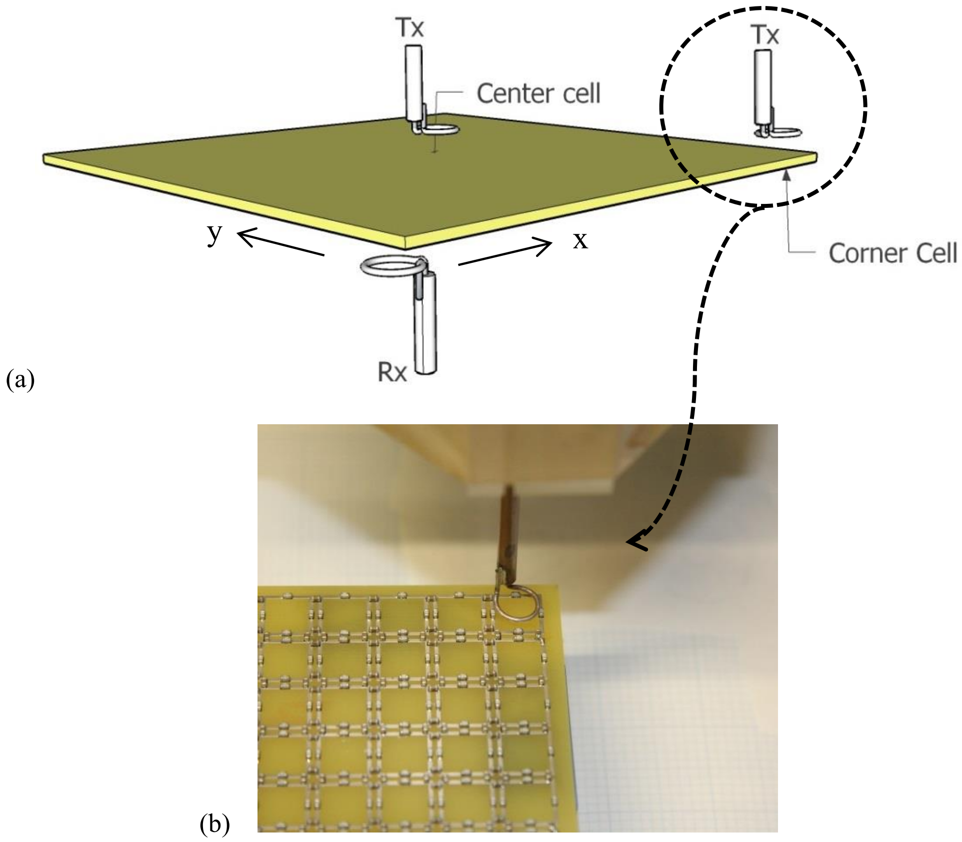

Fig. 5-6 *(a) Illustration of experimental setup for 2-D; (b) Photography of a corner of the 1-D CCG demonstration structure with the* T_x *probe positioned above the corner of the surface.*

on the major loop positioned in the middle of the surface and the other with T_x centred on a corner of the surface. For convenience, the two experimental runs were named as 'Centre T_x Measurement' and 'Corner $\mathrm{T_x}$ Measurement', respectively. The photograph shown in Fig. 5-6 (b) illustrates the latter case, showing a corner area of the waveguide surface with T_x centred on the corner major loop. During the experiments, R_x was placed under the PCB board and scanned over the entire surface using the computer-controlled translation stage mover. The receiver antenna R_x started from one corner, following a Raster scan pattern ending at the diagonally opposite corner covering a measuremnet grid at a resolution of 1mm. The probes were placed 4 mm away from the surface of the element's copper track, and this also took into account the 1.6 mm thickness of the PCB board. The two probes T_x and R_x were connected to a HP 8753ES vector network analyser (VNA) via 50 Ω coaxial cables to record the S_{21} scattering parameter. The real and imaginary components of S_{21} were taken as the average of 16 scans of 1601 points in the range 50 kHz to 150 MHz.

5.6 Experimental Analysis – Dispersion Characteristics

Fig. 5-7 (a)–(c) shows the log-magnitudes of S_{21} measured along the three paths with the same scale of –80 to –30 dB. Results for the axial <01/10> path and the diagonal <11> path were taken from the centre T_x measurement, in which the wave propagation was symmetric around the central point. Hence, one can extract dispersion characteristics from halfway along the two paths, as the element number in Fig. 5-7 (a) and (b) ranges from the central major loop (10th) to the end major loop (19th). Results for the edge path were taken from the corner T_x measurement, and the element number in Fig. 5-7 (c) ranges over the entire edge path (19 major loops). Surface waves propagating along the edge path exhibit a much narrower bandwidth than those along the two inside paths, therefore it is presented over the frequency range 90–150 MHz, while the two inside paths are presented over the frequency range 50 kHz to 150 MHz.

One can notice that there is no wave propagation under the frequency of the lowest resonance in Fig. 5-7 (a) (b) and (c). This is due to inefficient power injection at the lower part of the predicted passbands caused by the impedance mismatch between the source and the waveguide. This behaviour has been analysed in the study of 1-D structure in Section 4.3.2. The analytical fractional bandwidth of the diagonal <11> path and the axial <01/10> path are 187.6% and 186.4% respectively; however the measured ones are reduced to 83% and 81% respectively. However, these values still largely exceeds the 20% requirement of UWB channels.

One can see that a broadband beginning with a strong signal occurring around the starting element due to the strong direct coupling between R_x and T_x, as one of them is positioned just above the other. For all later loops, a clear passband emerges. Standing wave patterns appear in a similar fashion to the 1-D experimental results, which are caused by reflection at the ends of the paths.

The spatial period of a standing wave is half of its free-space wavelength ($\frac{\lambda}{2}$), which equals the distance between minima in the transmission spectra shown in Fig. 5-7 (a)–(c). The wave number β can be expressed as a function of λ as $\beta = \frac{2\pi}{\lambda}$. Therefore, one can establish a relationship between the required $\frac{\beta d}{\pi}$ and $\frac{\lambda}{2}$, as given by Eq. (5.2):

$$\frac{\beta d}{\pi} = \frac{d}{\frac{\lambda}{2}} \tag{5.2}$$

where *d* is the period of the CCG structure, which equals the distance between the centres of a pair of adjacent major loops (10.4 mm).

Eq. (5.2) allows a simple calculation for extracting the experimental dispersion characteristics $\frac{\beta d}{\pi}$. For example, one can read from Fig. 5-7 (a) that the half-wavelength of the standing wave pattern at $f = 64.22$ MHz equals the length of 4.25 structure periods. One can then calculate $\frac{\beta d}{\pi}$ by finding the ratio between *d* and this half-wavelength, which equals $\frac{1}{4.25}$ in this case. Fig. 5-7 (d)–(f) presents comparisons between predicted and measured $\frac{\beta d}{\pi}$ for the three above-mentioned paths. Dispersion curves extracted from the experimental results show good agreement with the analytical results derived from the dispersion equation of the 2-D CCG as given by Eq. (5.1).

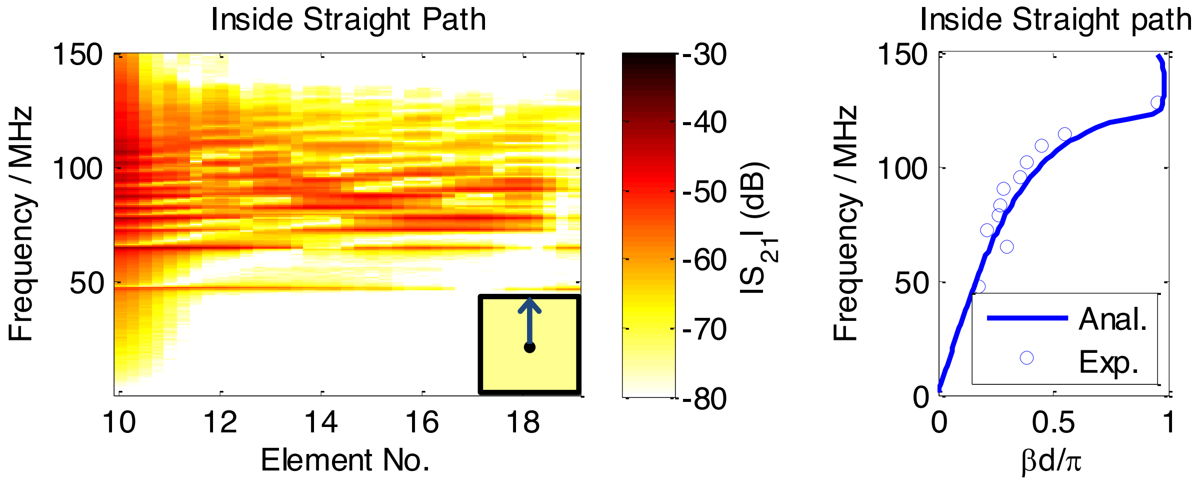

(a) Axial <01/10> Path (d) Axial <01/10> Path

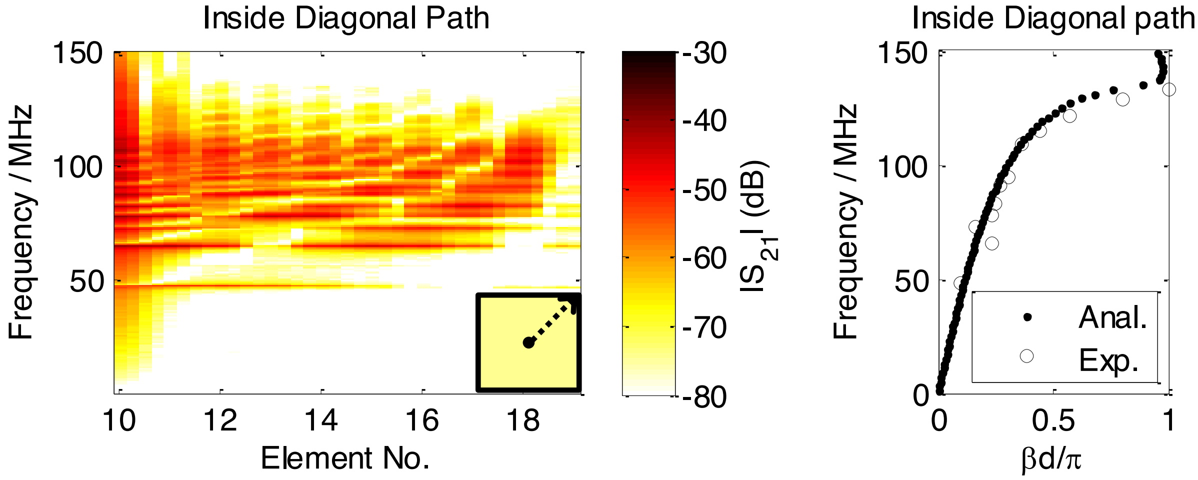

(b) Diagonal <11> Path (e) Diagonal <11> Path

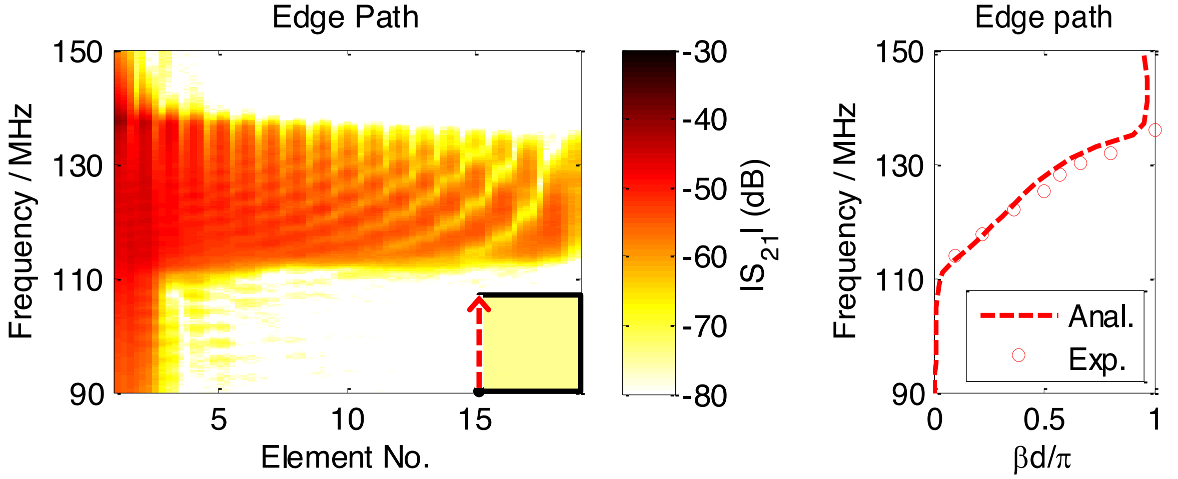

(c) Edge Path (f) Edge Path

Fig. 5-7 *(a)–(c) Log-magnitudes of* S_{21} *measured along the three paths with the same scale of –80 to –30 dB; (d)– (f)comparisons between predicted and measured βd/π for the three paths.*

When considering attenuation in a 1-D device, its attenuation is attributed mainly to resistive loss as its path loss is zero. For 2-D devices, one should also consider that planar expansion for wave-fronts leads to a $\frac{1}{r}$ path loss, where r is the distance between terminals. No attempt was made to extract a 2-D experimental attenuation performance in this study; however, it can be done by fitting the measured standing wave amplitude pattern with analytical wave patterns in a similar fashion to the 1-D study, with special consideration for path loss.

5.7 Experimental Analysis – Current Distributions

During the experiment, the R_x probe was put in close proximity to the waveguide, coupled to the magnetic flux set up by nearby waveguide elements. One can assume that magnetic field probe values are proportional to currents circulating in each waveguide element. The measurement scan over the entire surface can provide current distribution maps at the 1601 frequency sampling points between 50 kHz and 150 MHz.

In Section 3.8, the impedance matrix for the 2-D CCG was derived based on the mixed coupling model, which allows analytical predictions of the current distribution over the finite 2-D CCG array. The current in each element can be simply calculated by inverting the impedance matrix and multiplying it by the voltage vector (Eq. (3.53)). One can qualitatively predict current distributions for the 19×19 2-D demonstration device in the two measurement cases by assuming a 1 V perfect voltage source to be applied to either the centre element or to a corner element. Fig. 5-8 and Fig. 5-9 show a comparison between the predicted and measured current distribution maps over the 2-D demonstration structure. Six frequencies, 10, 62, 82, 104, 123 and 138 MHz, were chosen to show various frequency-dependent wave propagation behaviours over the passbands. Results for the corner T_x measurement and the center T_x measurement are presented below in sections (a) and (b), respectively.

(a) Corner T_x Measurement

Fig. 5-8 (a)–(f) shows analytical predictions of current distributions on a base 10 logarithmic scale and Fig. 5-8 (g)–(l) shows log-magnitudes of the forward scattering parameters S_{21} measured with T_x aligned above a corner major loop while R_x scans over the entire surface at the six exemplary frequencies.

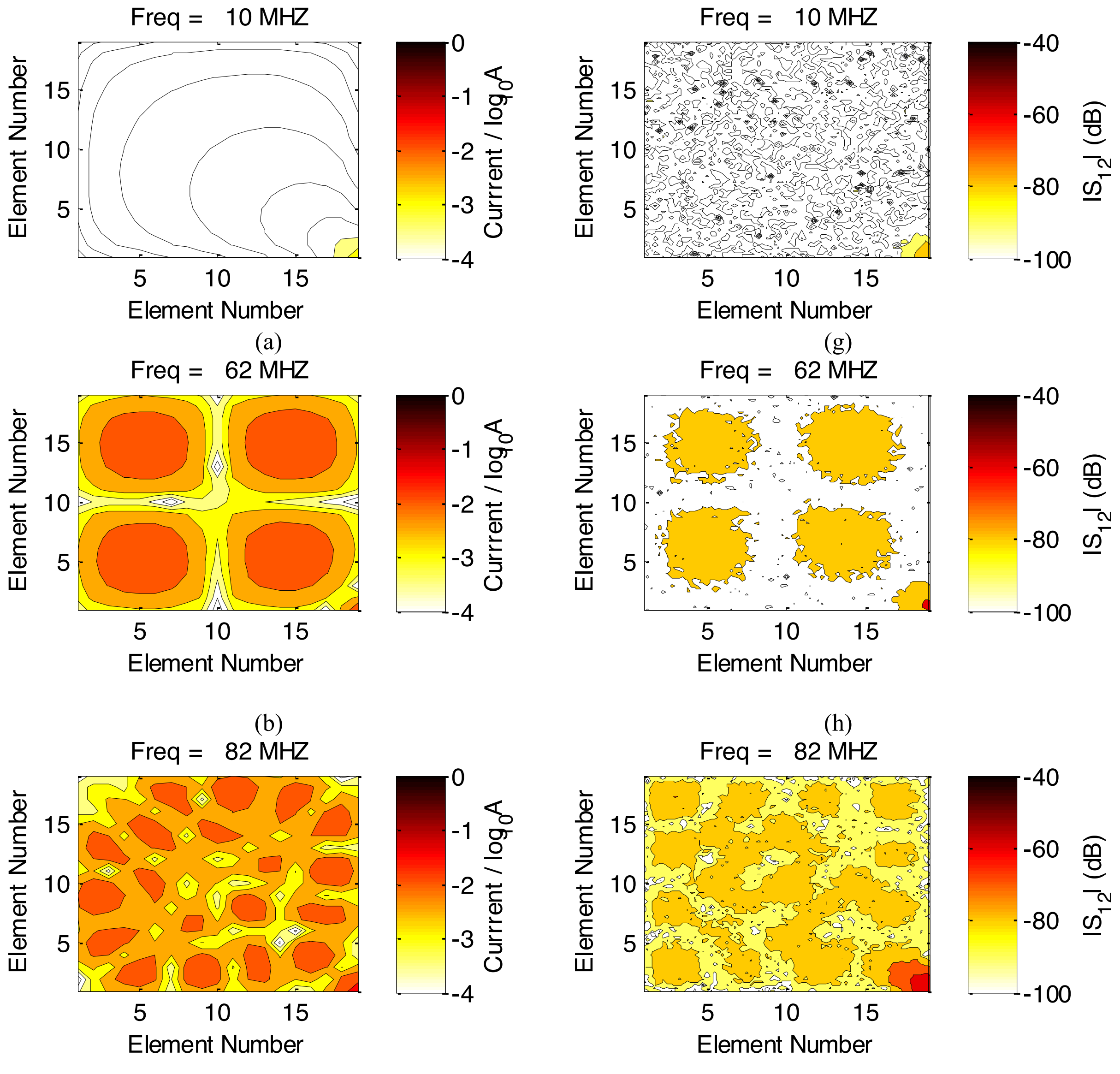

(a) (g)

(b) (h)

(c) (i)

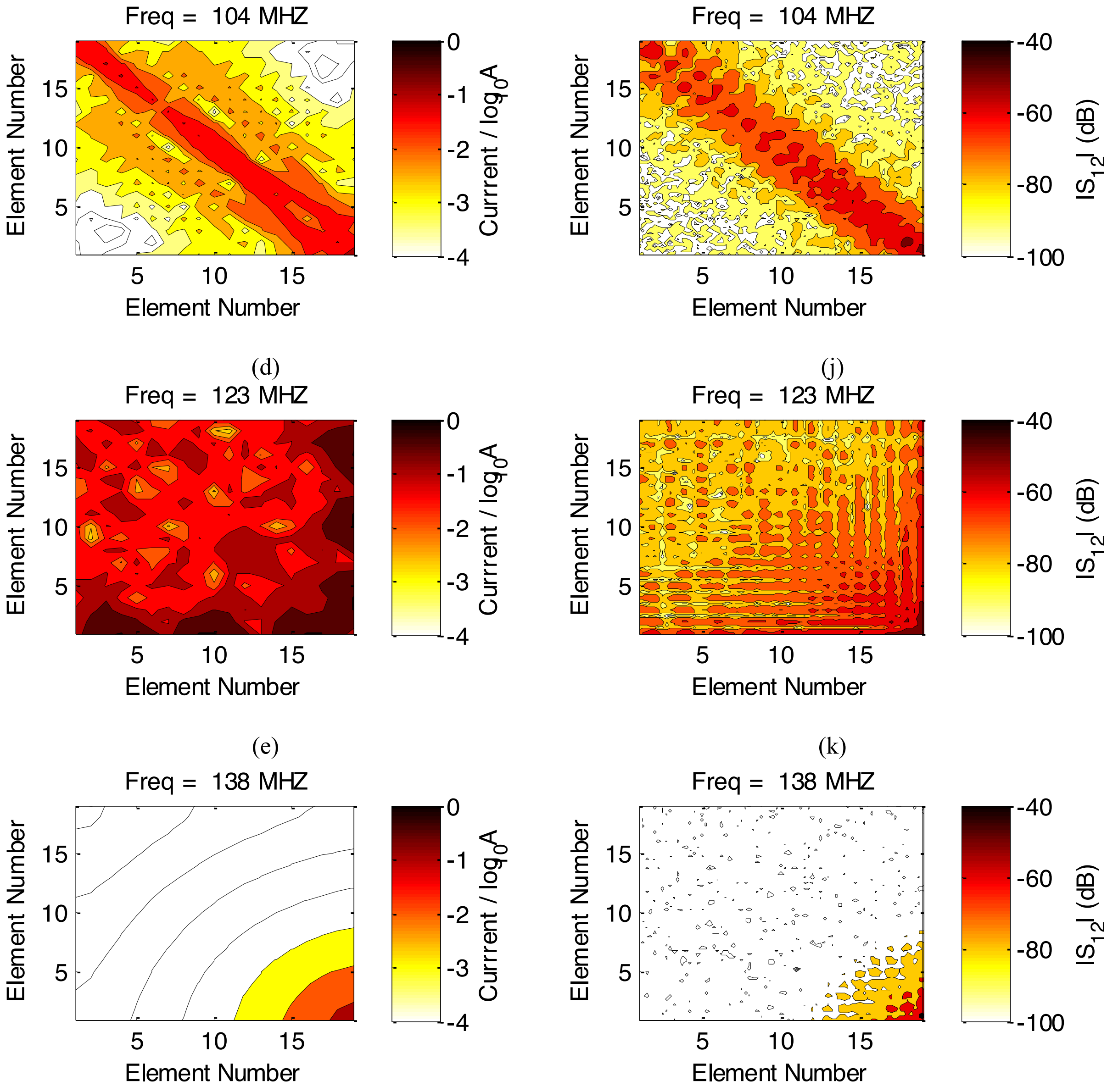

(d) (j)

(e) (k)

(f) (l)

Fig. 5-8 *The analytical current distributions on a base 10 logarithmic scale ((a)–(f)) derived from matrix analysis, and (g)–(l) log-magnitude of forward scattering parameters* S_{21} *measured in the corner* T_x *measurement taken at six frequencies, 10, 62, 82, 104, 123 and 138 MHz.*

Fig. 5-8 presents the qualitative matching between the analytical current distribution and the measured S_{21} when the transmitter antenna T_x is placed in the corner. The analytical model predicts the current circulating in each discrete loop (major loop and minor loop). The measured S_{21} represents the magnetic flux received by the receiver antenna loop R_x, which is assumed to be proportional to the current circulating in the nearest loops.

One can see that the current distribution over 2-D CCG waveguide surface is very sensitive to frequency variation. The attenuation at the edges of pass-band is so high that no standing wave patterns are present at 10 MHz and 138 MHz. When the frequency $f = 62$ MHz and 82 MHz, one can see well-distributed standing wave patterns over the entire 2-D surface. One can see that wave propagation is mainly along the diagonal <11> path when f =104MHz. When $f = 123$ MHz, it shows more intensive current distribution along the edge paths.

One can find discrepancies between the experimental and the analytical results at $f =$ 82 MHz (Fig. 5-8 (c) and (i)) and at f = 123 MHz (Fig. 5-8 (e) and (k)). At f = 82 MHz, the analytical result in (c) shows one standing wave pattern missing in the upper left corner, and its standing wave patterns in the lower left corner and upper right corner split into two as compared with the experimental result in (c). At $f = 123$ MHz, the analytical result in (e) predicts the appearance of a surface wave pattern travelling along the edges; however, the experimental result in (k) does not show this.

Three factors might account for such discrepancies:

(i) **Capacitance tolerance:** The analytical model assumes that the CCG waveguide consists of symmetric resonators which all share the same resonance frequency. However, this assumption is very difficult to achieve in the experimental set-up due to the tolerance of capacitance components. The gap capacitance C_{gap} is designed to be 220 pF and gives the resonant frequency of a 4C metallic loop as 150 MHz. In the experiment, as given in Table 4-1, the capacitance used for $\mathrm{C_{gap}}$ had a 10% tolerance and could range between 198 pF and 242 pF. This capacitance tolerance leads to a variation in the resonance frequency of 4C metallic loops, ranging between 143 and 158 MHz. The previous work [63] shows that the transmission coefficient decreases as the capacitance tolerance increases. The decreasing transmission coefficient corresponds to the increasing reflection loss. This is because the reflection not only happens at the terminus of the waveguide, but also can happen between different CCG elements in such a non-uniform waveguide.

(ii) **Resistance of solder joints:** In the study of the 1-D CCG structure, sufficient matching was achieved between the analytical and the experimental dispersion curves under the approximation that the resistance of solder joints is negligible. This approximation is applied here in the analytical calculation of 2-D CCG structures. However, a 4C metallic loop used in a 2-D structure requires solder joints on all four branches and results in a larger resistance than a 2C metallic loop used in a 1-D structure.

(iii) **Frequency resolution:** The current distribution is measured at 1601 frequencies between 50 kHz and 150 MHz, so the frequency resolution is 94 kHz. One might not be able to obtain experimental results exactly at the simulated frequencies.

(b) Centre T_x Measurement

Fig. 5-9 (a)–(f) shows analytical predictions of current distributions on a base 10 logarithmic scale and Fig. 5-9 (g)–(l) shows log-magnitudes of the forward scattering parameters S_{21} measured with T_x positioned just above the central major loop while R_x scans over the entire surface at the six exemplary frequencies.

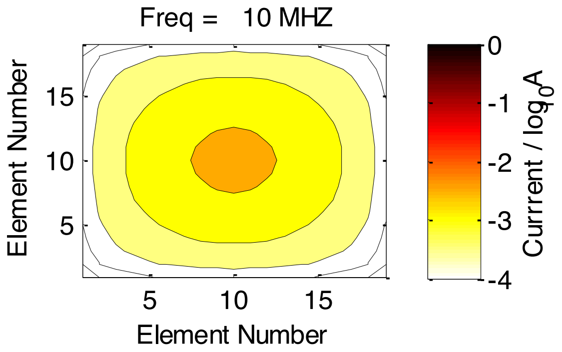
Freq = 10 MHZ
Element Number
15
10
5
5
10
15
Element Number
0
-1
-2
-3
-4
Currrent / log$_0$A

(a)

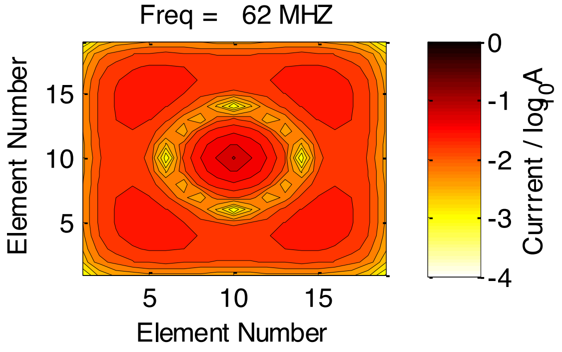
Freq = 62 MHZ
Element Number
15
10
5
5
10
15
Element Number
0
-1
-2
-3
-4
Currrent / log$_0$A

(b)

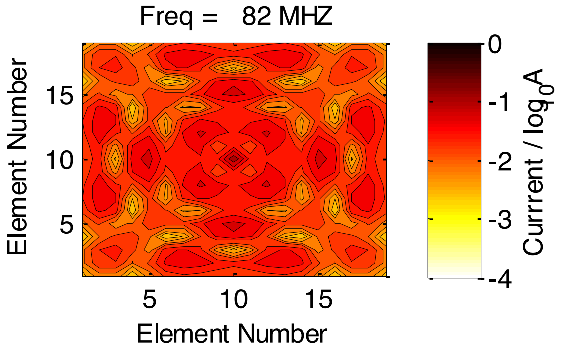
Freq = 82 MHZ
Element Number
15
10
5
5
10
15
Element Number
0
-1
-2
-3
-4
Currrent / log$_0$A

(c)

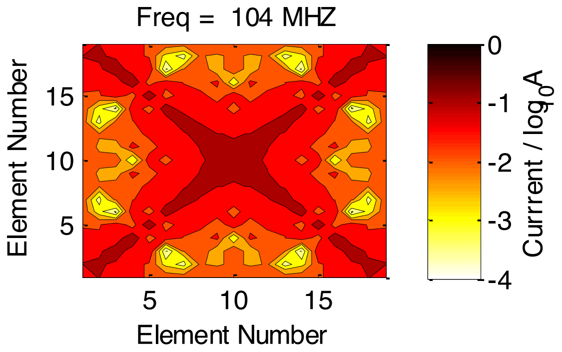
Freq = 104 MHZ
Element Number
15
10
5
5
10
15
Element Number
0
-1
-2
-3
-4
Current / log$_0$A

(d)

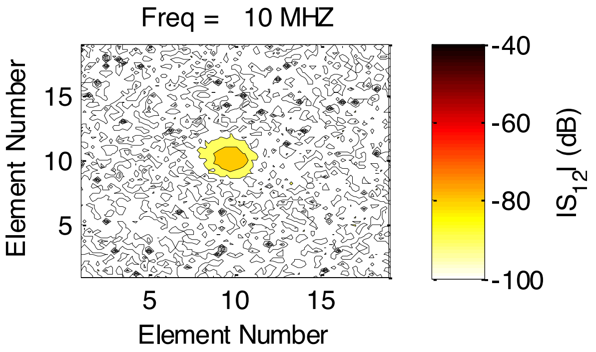
Freq = 10 MHZ
Element Number
15
10
5
5
10
15
Element Number
-40
-60
-80
-100
IS$_{12}$I (dB)

(g)

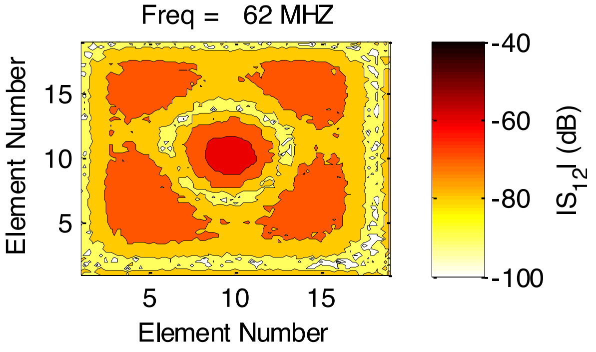
Freq = 62 MHZ
Element Number
15
10
5
5
10
15
Element Number
-40
-60
-80
-100
IS$_{12}$I (dB)

(h)

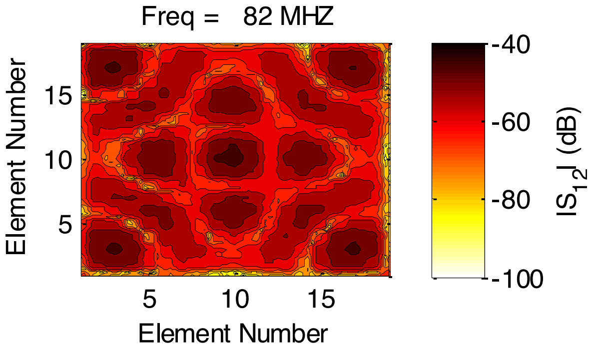
Freq = 82 MHZ
Element Number
15
10
5
5
10
15
Element Number
-40
-60
-80
-100
IS$_{12}$I (dB)

(i)

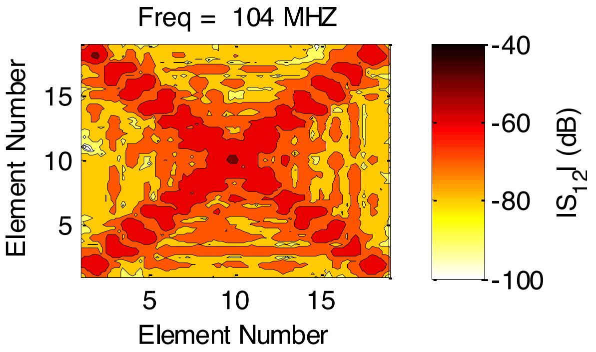
Freq = 104 MHZ
Element Number
15
10
5
5
10
15
Element Number
-40
-60
-80
-100
IS$_{12}$I (dB)

(j)

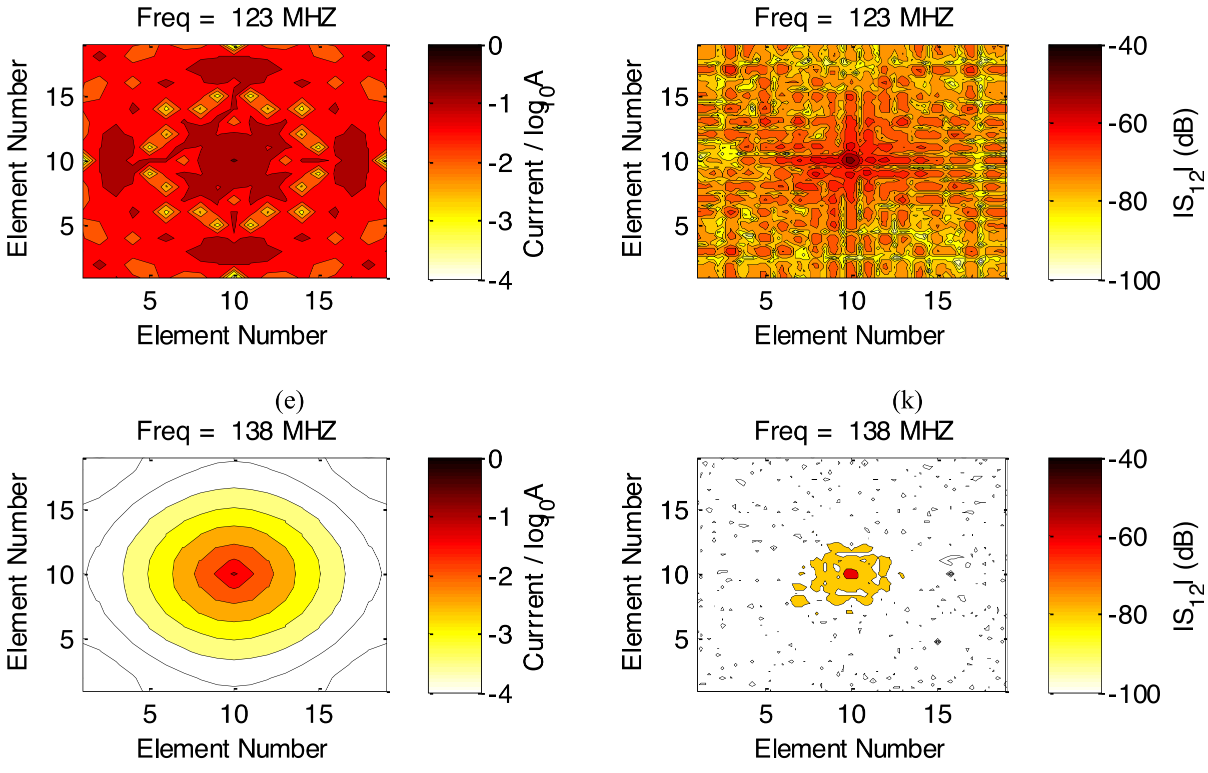

(e) (k)

(f) (l)

***Fig. 5-9** The analytical current distributions on a base 10 logarithmic scale ((a)–(f)) derived from matrix analysis, and (g)–(l) log-magnitude of forward scattering parameters S_{21} measured in the corner T_x measurement taken at six frequencies, 10, 62, 82, 104, 123 and 138 MHz.*

Fig. 5-9 shows qualitative matching between the analytical current distribution and the measured S_{21} when the transmitter antenna T_x is placed in the center of the surface. Similar to Fig. 5-8, the analytical model predicts the current circulating in each discrete loop (major loop and minor loop). The measured S_{21} represents the magnetic flux received by the receiver antenna loop R_x which is assumed to be proportional to the current circulating in the nearest loops.

The current distribution over 2-D CCG waveguide surface is very sensitive to frequency variation. The attenuation at the edges of pass-band is so high that no standing wave patterns are present at 10 MHz and 138 MHz. When the frequency f = 62 MHz and 82 MHz, one can see well-distributed standing wave patterns over the entire 2-D surface. One can see that wave propagation is mainly along the diagonal <11> path in both cases when f =104 MHz.

When f =123 MHz, the analytical result shows more intensive current distribution along axial <01/10> path.

One can find discrepancies between the experimental and the analytical results at f = 123 MHz (Fig. 5-9 (e) and (k)). The analytical result in Fig. 5-9 (e) predicts that there should be standing wave patterns along the axial <01/10> path. The experimental result in Fig. 5-9 (k) shows more intensive current distribution along this path; however, it does not present standing wave patterns. Possible reasons to explain this discrepancy are similar to those used in the discussion of Fig. 5-9.

The frequency-dependent current distribution behaviour of the 2-D CCG gives it the potential to be used as a 2-D contactless data transfer channel offering a robust multipath environment for multiple terminal connections. Frequency channelization can be applied in the 2-D CCG waveguide surface, allowing waves of different frequency ranges to propagate along various paths and to be excited and picked up by terminals at different locations.

5.8 Conclusions

This chapter takes the 1-D CCG study to its 2-D expansion and explores the 2-D CCG waveguide surface from two perspectives: dispersion characteristics and current distributions over the surface. The 2-D CCG was studied in comparison with its 1-D counterpart – the 1-D 4C CCG and its previously reported 1-D structure, the 1-D 2C CCG.

There are two types of waves propagating in 2-D CCG structures: surface waves travelling along edge paths and MI and EI waves propagating inside the waveguide surface. The latter type of wave can propagate in a 2-D CCG structure along multiple paths, among which, two special cases are considered here – the diagonal <11> path and the axial <01/10> path.

The 2-D CCG exhibits the same important feature of the 1-D CCG: the appearance of a no-propagation point where the positive and negative couplings exactly cancel each other. These no-propagation points were found at different capacitance values for the three paths studied here.

Considering both bandwidth and dispersion performance, the two inside paths – the diagonal <11> path and the axial <01/10> path – provide a less dispersive and 'lossy' propagation channel, with significantly greater bandwidth performance, in comparison with the edge path carrying surface waves. The two inside paths exhibit comparable dispersion and attenuation performance to the 1-D 2C CCG and provide reasonably good bandwidth performance. The analytical fractional bandwidth of the diagonal <11> path and the axial <01/10> path are 187.6% and 186.4% respectively; however the measured ones are reduced to 83% and 81% respectively. This is due to the inefficient power injection at the lower part of the predicted passbands caused by the impedance mismatch between the source and the waveguide. However, these values still largely exceeds the 20% requirement of UWB channels. The two inside paths provide good examples of data channels in a 2-D CCG with low loss and dispersion but high data capacity and speed. Channelization can be used to get several sub-channels with less dispersion and group delay in a similar fashion to the 1-D CCG device.

When comparing the two 1-D cases, the 1-D 2C CCG shows improved performance in terms of attenuation, dispersion and bandwidth, and offers great potential to be used as a 1-D contactless data transfer channel.

Current distributions over the 2-D CCG waveguide surface were studied, both numerically and experimentally, and found to be very sensitive to frequency variation. Such frequency-dependent current distribution behaviour of the 2-D CCG gives it the potential to be used as a 2-D contactless data transfer channel offering a robust multipath environment for multiple terminal connections. Frequency channelization can be applied in the 2-D CCG waveguide surface, allowing waves of different frequency ranges to propagate along various paths and to be excited and picked up by terminals at different locations.

The 2-D CCG waveguide surface has the potential to be used as a track-free data bus in electronic systems with possibilities for inter-chip communications if the ICs in such systems are capable of launching and detecting MI and EI waves. The 2-D CCG waveguide surface also sees potential in body area networking, such as linking up patient monitors, saving alarms and headphones through clothes embedded with 2-D waveguide surfaces.

CHAPTER 6

TERMINAL OPTIMIZATION

In previous chapters, CCG structures have been considered as potential candidates for distributed broadband data transfer channels, where bandwidth is significant in determining overall data capacity. This contrasts strongly with the requirements for a power transfer system. The minimum requirement of an efficient power transfer system is to transfer power at one single frequency, but high power transfer efficiency is required.

This chapter investigates the potential for the 1-D CCG structure to be used as a contactless power transfer device, capable of carrying power along a 1-D array between suitably prepared T_x and R_x terminals. The study focuses on terminal optimizations with a view to maximizing power transfer efficiency for a CCG-based power transfer system. Section 6.1 describes a simple 1-D CCG-based contactless power transfer system; Section 6.2 describes the theory of the reflectionless matching condition which enables optimum terminals offering maximized power transfer efficiency; Section 6.3 determines the terminating impedance for semi-infinite CCG-based power transfer structures; Section 6.4 considers a finite length structure and the impact of standing waves on input impedance; Section 6.5 describes a simple experimental setup to measure power transfer efficiency; and Section 6.6 compares the experimental results to the predictions of the analytical model.

6.1 1-D CCG-based Power Transfer System

A review of previous work described in [50], [84], [85] and [97] gives a complete view of terminal optimizations for a MIW-based power transfer system. These studies introduced an analytical method for modelling an MIW-based power transfer line with T_x and R_x terminals coupled to resonators located at points anywhere along the line. This model allows the prediction of power transfer efficiency and for obtaining optimal terminal designs for MIW-based power transfer systems. Both T_x and R_x terminals were investigated with two different configurations: the source or the load connected in *series* with other RLC components along the loop or in *parallel* across the capacitance of the loop.

One can now investigate terminal optimizations for a CCG-based power transfer system in a similar fashion to the MIW-based study. This study only considers one simple case, in which a parallel-connected T_x terminal and a series-connected R_x terminal are coupled to the first and the last major loop, respectively. Only the optimum R_x terminal will be proposed here, as the T_x terminal can be analysed following a similar procedure.

Fig. 6-1 presents a sketch of a 1-D CCG-based power transfer system, including an *N*-element CCG array with a parallel-connected T_x terminal and a series-connected R_x terminal.

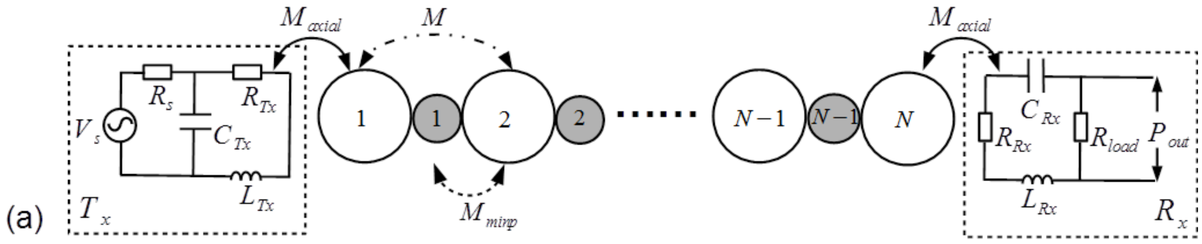

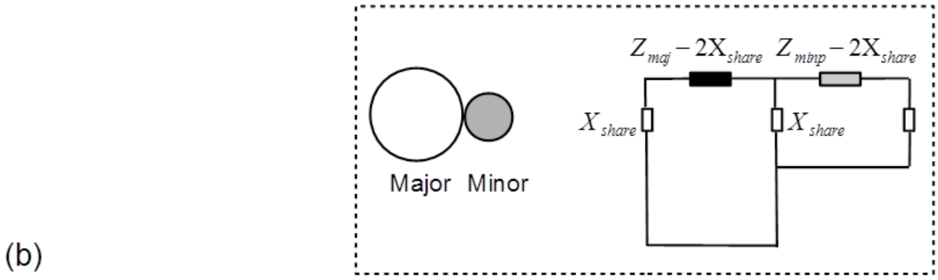

Fig. 6-1 *(a) Sketch of a 1-D CCG-based contactless power transfer system: a CCG line consisting of N pairs of major and minor loops;* T_x *and* R_x *are aligned to the first and last major loops, respectively; (b) illustration of an equivalent circuit consisting of a pair of adjacent cells (large white cell and small grey cell) which represent the major and minor loops, respectively. Parameters used in this figure follow the naming conventions used in previous chapters.*

The *N*-element CCG array discussed here consists of *N* major loops and $N - 1$ minor loops as it both starts and ends with major loops. M represents the mutual inductance between nearest-neighbour major loops, M_{minp} represents the mutual inductance between a pair of adjacent major and minor loops with a common branch shared between them (proven to be negligible as shown in Table 3-2, so it would not be considered in the following discussion), and M_{axial} represents the mutual inductance which couples T_x and R_x terminals to its nearest-neighbour major loop.

6.2 Reflectionless Matching Condition

Fig. 6-2 (a) illustrates a 1-D CCG waveguide with real termination – a series-connected R_x terminal coupled to the last major loop – while Fig. 6-2 (b) shows equivalent termination, where Z_{load} represents the load impedance effectively introduced by the R_x terminal into the last major loop via the mutual inductance M_{axial}.

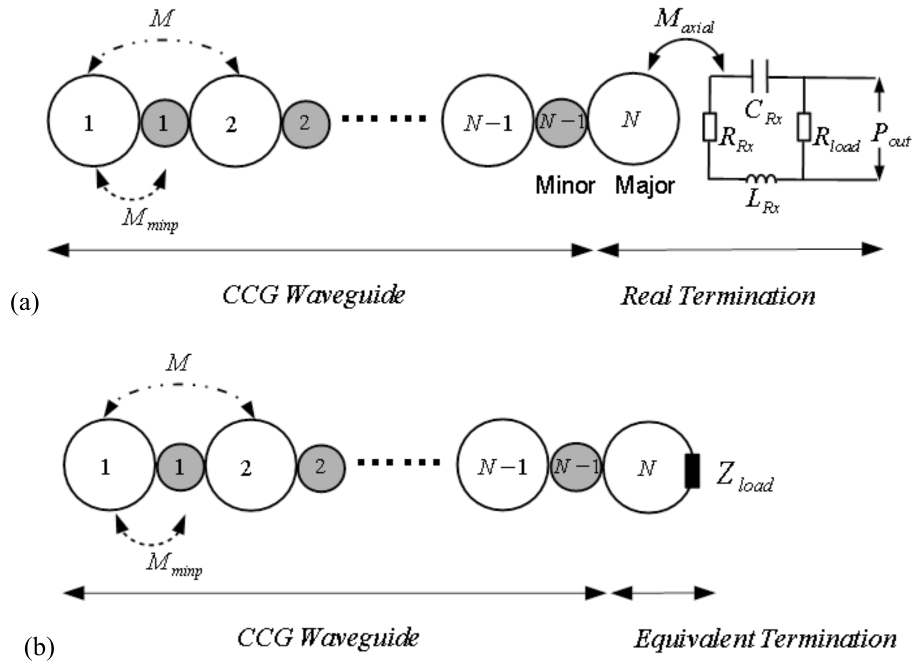

Fig. 6-2 *Schematic diagram of a 1-D CCG-based waveguide with (a) real termination –* R_x *terminal; (b) equivalent termination.*

Given that the series-connected R_x terminal has a total impedance $Z_{Rx} + R_{load}$, where $Z_{Rx} = R_{Rx} + j\omega L_{Rx} + \frac{1}{j\omega C_{Rx}}$, and is coupled to the last major loop with a mutual inductance M_{axial}, the load impedance Z_{load} effectively introduced into the last major loop can be calculated via a circuit analysis [100] and can be expressed as Eq. (6.1):

$$Z_{load} = \frac{\omega^2 M_{axial}^2}{Z_{Rx} + R_{load}} \tag{6.1}$$

A non-reflective CCG-based waveguide can be formed by inserting an extra terminating impedance Z_{T-CCG} into the last major loop. The terminating impedance Z_{T-CCG} acts as a semi-infinite CCG line connected to the last major loop, which absorbs all the incident power and gives to a finite structure the property of an infinite line. The concept of forming a non-waveguide by inserting a terminating impedance was originally studied for MIW-based waveguides in [63], as reviewed in Section 2.3, and the corresponding terminating impedance Z_{T-MIW} was given by Eq. (2.17).

In a power transfer system, absorbing terminations are most undesirable as they will lead to large fixed losses and seriously degrade overall efficiency unless they are themselves the loads to which power is being provided [10]. However, an R_x terminal, whose load impedance Z_{load} is equalized to impedance of a non-reflective termination Z_{T-CCG}, makes the optimal terminal as it stops reflection and offers the maximum power transfer efficiency to the load. This reflectionless matching condition can be expressed by Eq. (6.2):

$$Z_{load} = Z_{T-CCG} \tag{6.2}$$

6.3 Terminating Impedance

Fig. 6-3 presents an equivalent circuit model corresponding to a non-reflective 1-D CCG waveguide formed by including a terminating impedance Z_{T-CCG} in its last major loop.

One can derive Z_{T-CCG} for 1-D CCG waveguides with the aid of the dispersion equation and Kirchhoff's Voltage Law applied to the last major loop.

We shall now return to Eq. (3.1) which describes the total potential of the m^{th} major loop. The relation described in Eq. (3.1) can be applied to every loop in a 1-D CCG array except at the first and last major loops. When assuming that a CCG waveguide ends with the m^{th} major loop, this last major loop can see both major and minor neighbours at the $m-1^{th}$ site, but the m^{th} minor loop and the $m+1^{th}$ major loop are both missing. Eq. (6.3) results from applying Kirchhoff's Voltage Law to the m^{th} major loop when neglecting M_{minp}:

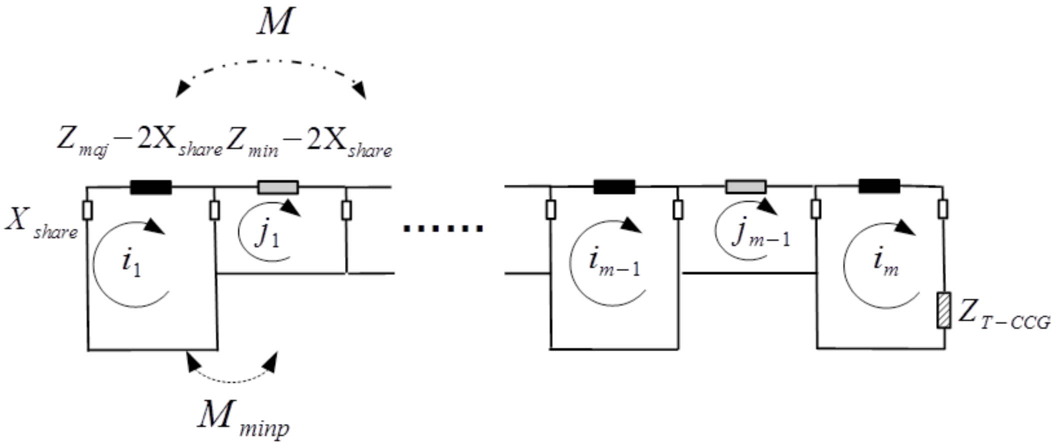

Fig. 6-3 *Use of a terminating impedance Z_{T-CCG} to allow calculation for an infinite 1-D CCG waveguide; Z_{maj} is the impedance of a major loop in the CCG; Z_{min} is the impedance of a minor loop; X_{share} is the impedance of one shared branch between a pair of adjacent major and minor loops.*

$$\left(Z_{maj} + Z_{T-CCG}\right)i_m + j\omega M i_{m-1} + j_{m-1}(-X_{share}) = 0 \tag{6.3}$$

where the current in the m^{th} major loop is given by i_m, while the current in the $m-1^{th}$ minor loop is given by j_{m-1}. Recall that the expression for travelling waves is $i_m = I_0 e^{-\gamma md}$ and $j_m = J_0 e^{-\gamma md}$, where I_0 and J_0 are the current amplitudes at the first major and first minor loops, respectively.

One can substitute the impedance for the missing m^{th} minor and $m+1^{th}$ major loops by inserting Z_{T-CCG} into the m^{th} major loop. Therefore, Z_{T-CCG} can be found by equating Eqs. (6.3) and (3.1), as expressed by Eq. (6.4):

$$Z_{T-CCG} = j\omega M e^{-\gamma d} - \frac{(-X_{share})^2(1+e^{-\gamma d})}{Z_{min}} \tag{6.4}$$

Fig. 6-4 shows the results of $Z_{T-CCG} = R_{T-CCG} + jX_{T-CCG}$ calculated for a demonstration structure built with the same dimensions as the one introduced in Table 3-1. This device therefore shares all the geometry-dependent inductive and resistive parameters with the previously constructed one given in Table 3-2, but uses different gap capacitances

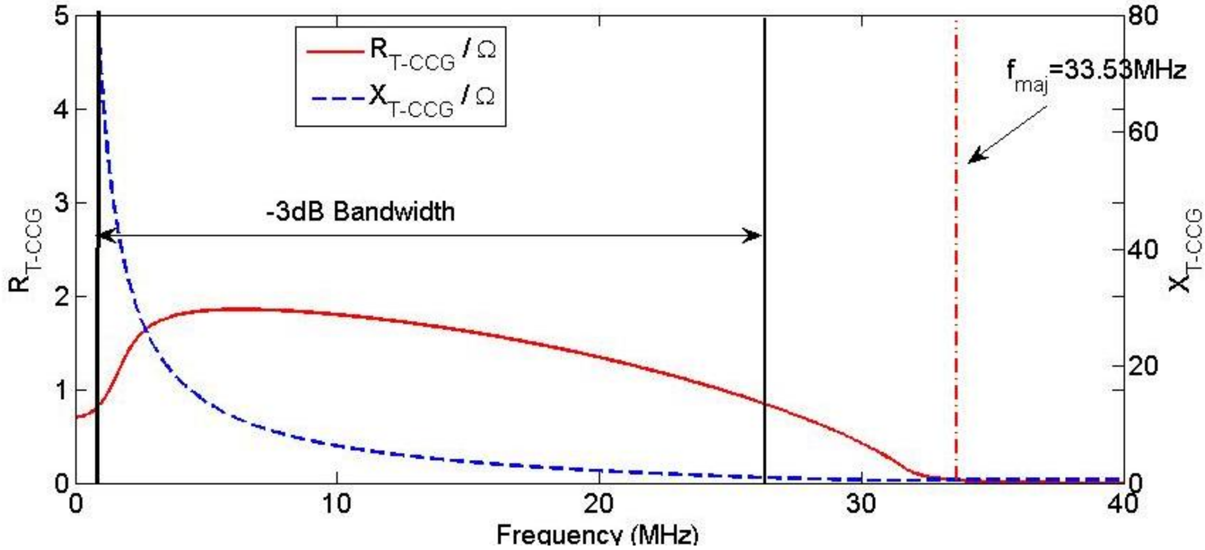

Fig. 6-4 Results of $Z_{T-CCG} = R_{T-CCG} + jX_{T-CCG}$ calculated for a 1-D CCG demonstration structure with C_{gap} = 2200 pF.

(C_{gap}= 2200 pF). The resonant frequency of a major loop is thus now tuned to f_{maj} = 33.53 MHz.

In practice, building an R_x terminal satisfying the reflectionless matching condition ($Z_{load} = Z_{T-CCG}$) can be rather difficult over a large bandwidth, as both the real component R_{T-CCG} and the imaginary component X_{T-CCG} are very sensitive to frequency variation. For the –3 dB bandwidth, R_{T-CCG} varies by 35% about 1.36 Ω, while X_{T-CCG} varies by nearly 100% about –30.3 H and approaches infinity when the frequency tends to zero.

The minimum requirement for an efficient power transfer system is to transfer power at a single frequency, but with high transfer efficiency. Therefore, Z_{T-CCG} can be used to design an optimal R_x terminal for a predetermined frequency based on Eqs. (6.1) and (6.2). The impedance of a series-connected R_x terminal has a real component ($R_{load} + R_{Rx}$) and an imaginary component ($j\omega L_{Rx} + \frac{1}{j\omega C_{Rx}}$). The geometry-dependent components R_{Rx} and L_{Rx} are fixed once the dimension of an R_x terminal loop is determined, while R_{load} and C_{Rx} are adjustable to achieve the reflectionless matching condition. The R_x terminal loop shares the

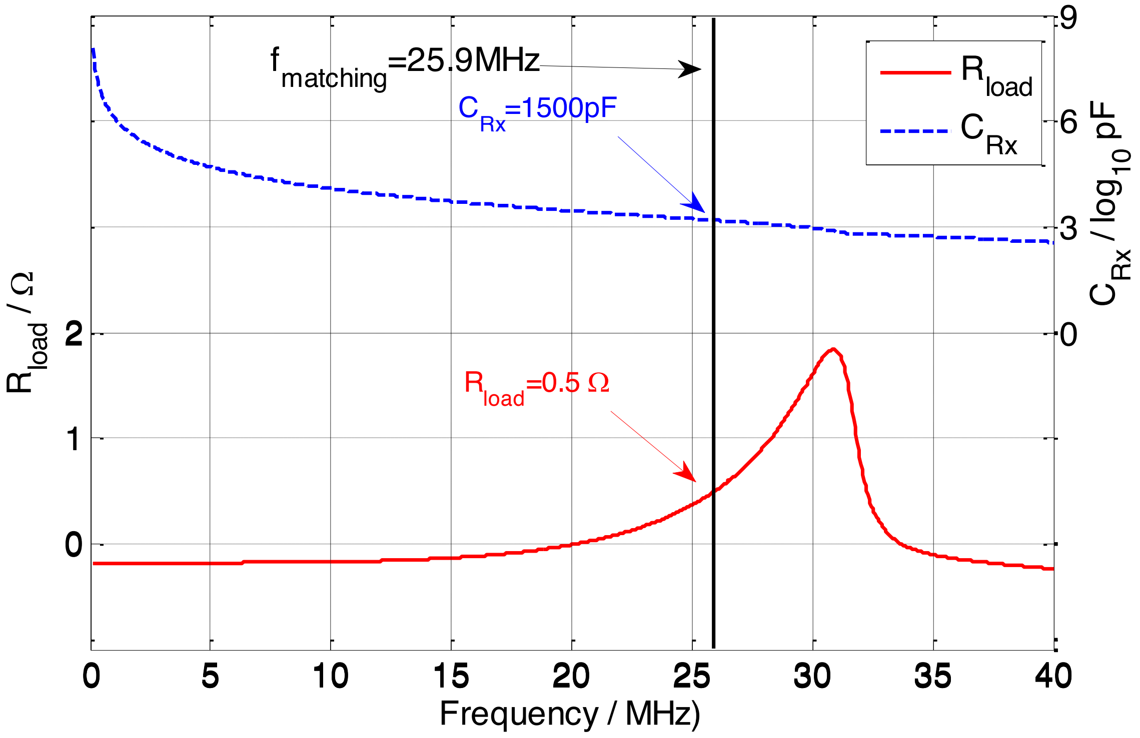

Fig. 6-5 Results of R_{load} and C_{Rx} required to design an optimal R_x terminal, where $f_{matching}$ is the matching frequency using the reflectionless matching condition.

same track size as previously reported in the 1-D demonstration device described in Table 3-1, so L_{Rx}= 20.48 nH and R_{Rx}= 0.2 Ω. Fig. 6-5 shows the values of R_{load} and C_{Rx} required to design optimal R_x terminals. For example, the R_x terminal built with R_{load} = 0.5 Ω and C_{Rx}= 1500 pF is the optimal terminal for $f_{matching}$ = 25.9 MHz.

6.4 Input Impedance and Standing Waves

The previous section shows that the optimal R_x terminal can be achieved under the reflectionless matching condition where $Z_{load} = Z_{T-CCG}$. In order to further explore this condition, this section compares the input impedance calculated for an infinite CCG array and a finite 10-element CCG array with Z_{T-CCG} included in the last major loop.

When considering a semi-infinite CCG array connected to a source-driven major loop, as shown in Fig. 6-6, one can simply derive the effective input impedance ($\mathrm{Z_{input}} = \mathrm{R_{in}} + \mathrm{jX_{in}}$) presented to the source, as expressed by Eq. (6.5):

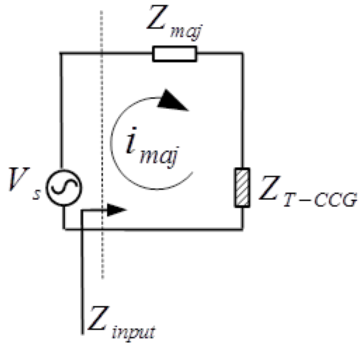

Fig. 6-6 *Circuit diagram for Z_{T-CCG}, which is the impedance of a semi-infinite line connected to a source-driven major loop. Z_{input} is the input impedance of the whole system as illustrated.*

$$Z_{input} = \left(Z_{maj} + Z_{T-CCG}\right) \tag{6.5}$$

Fig. 6-7 shows the input impedance for a semi-infinite line, which is a smooth function, but for a finite line there will be strong reflection of power back along the line towards the source, resulting in standing waves being formed. The effects of standing waves are expected to modulate the input impedance about the infinite model result, and therefore have an impact on the performance for most applications. However, if a terminating impedance Z_{T-CCG}, suitably prepared for a chosen frequency, is included in the last major loop of the line, this finite line should behave the same as an infinite line at this specific frequency.

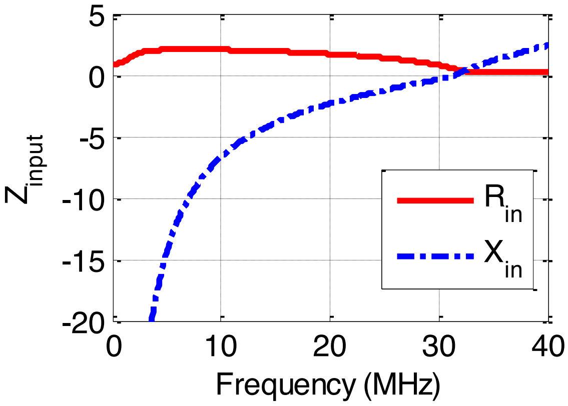

Fig. 6-7 *Input impedance $Z_{input} = R_{in} + jX_{in}$ calculated for an infinite 1-D CCG waveguide.*

To calculate the input impedance of a finite *N*-element CCG waveguide, one can obtain an N×N impedance matrix ($\boldsymbol{Z}$), as expressed by Eq. (3.53) (see Section 3.8), which can be used to compute the current ($\boldsymbol{I}$) circulating in each loop of a line driven by a source voltage connected to the first major loop, as expressed by Eq. (3.53). The input impedance is the ratio of the potential generated across the input of the waveguide and the current drawn from the source.

Fig. 6-8 shows the comparisons between the input impedance of an infinite line and the results calculated for a finite 10-element CCG waveguide. Four cases are presented here, among which, Fig. 6-8 (a) shows a finite line without any load and Fig. 6-8 (b)–(d) shows finite lines with an extra Z_{load} included in the last major loop, whose value is designed to be equalized to Z_{T-CCG} at three different matching frequencies $f_{matching}$: 10, 15 and 20 MHz. Fig. 6-8 (a) shows that the effects of standing waves modulate the input impedance components about the infinite model results. Fig. 6-8 (b)–(d) shows that the input impedances of the three loaded waveguides are in fact quite close to the result for an infinite line around these matching frequencies $f_{matching}$ at which $Z_{load} = Z_{T-CCG}$. These optimal loads suppress standing waves around the corresponding frequencies, removing the strong frequency variation in input impedance generated in the unloaded finite line at their operating frequencies.

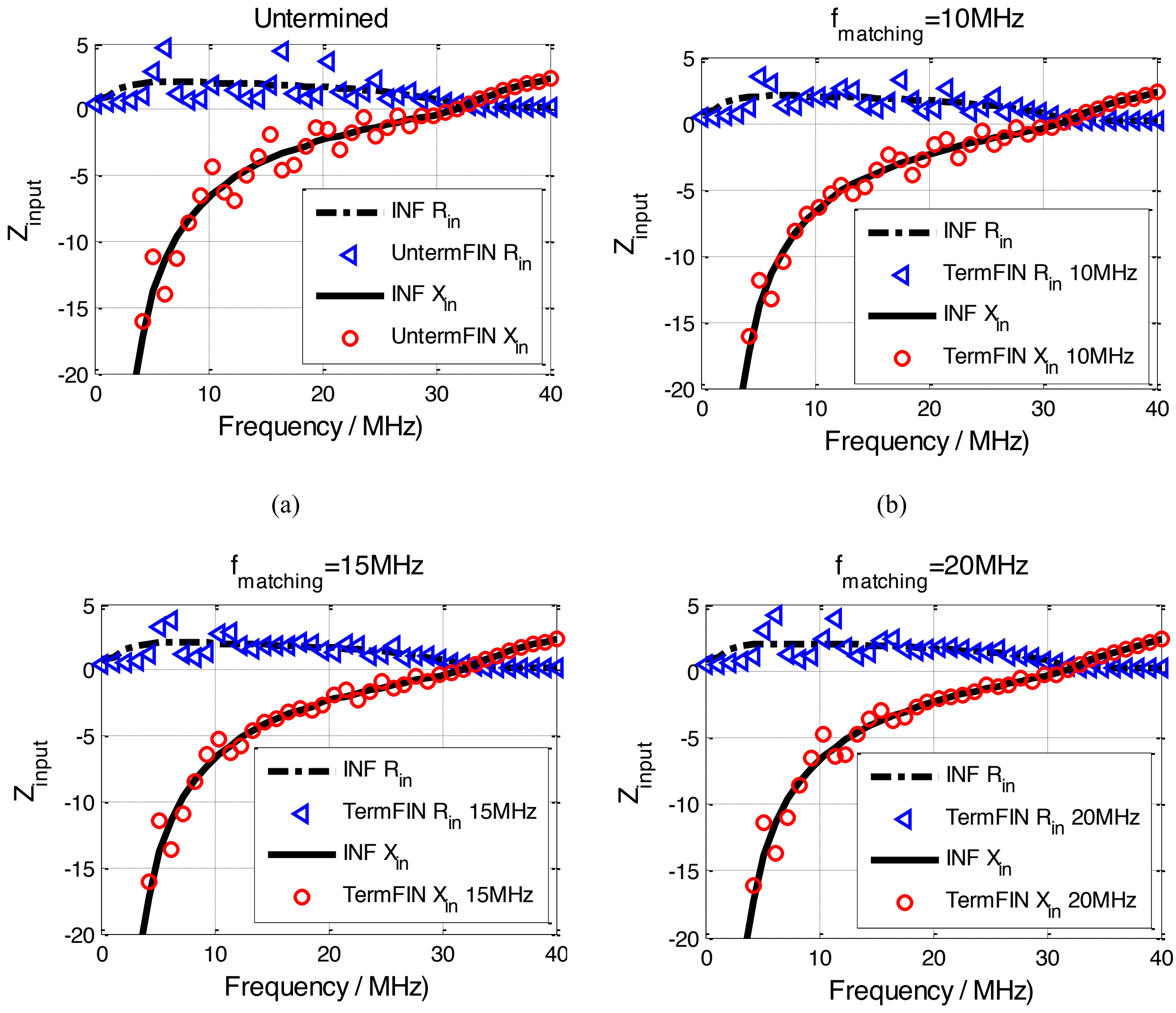

(a) (b)

(c) (d)

Fig. 6-8 *Input impedance calculated for an infinite CCG line in comparison with (a) a finite line without any load; a 10-element finite line with load impedance* Z_{load} *prepared to be equal to terminating impedance* Z_{T-CCG} *at three different frequencies: (b) 10 MHz; (c) 15 MHz; and (d) 20 MHz.*

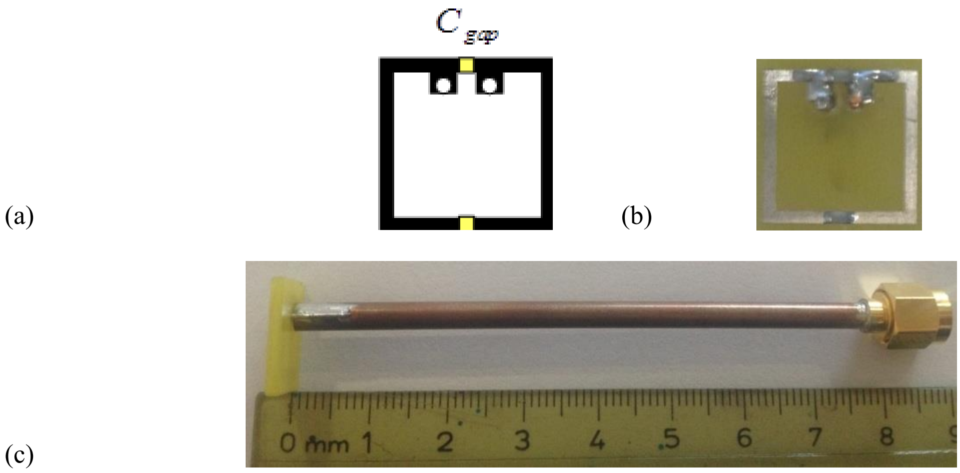

Fig. 6-9 *Description of the parallel-connected* T_x *terminal loop built for the experiment: (a) sketch of the* T_x *terminal tracks with the two gap capacitances* C_{gap} *labelled; (b) photograph taken of the* T_x *terminal with the two gap capacitances* C_{gap} *clearly displayed; (c) photograph of the whole terminal structure, showing the attachment of the resonant loop to an 8 mm long semi-rigid cable terminated by a SMA male connector.*

6.5 Experimental Setup

In previous sections, analytical models were derived which allowed the design and construction of an optimal R_x terminal under reflectionless matching conditions. A simple experimental verification was conducted and will be presented in this section. A 10-element 1-D CCG waveguide, a parallel-connected T_x terminal and a series-connected R_x terminal were constructed as a demonstration system.

A 10-element waveguide was built with the same geometric dimensions as the one described in Table 3-1 (see Section 3.3). A sketch of the demonstration waveguide can be found in Fig. 4-1 (see Section 4.1). This device uses a coupling capacitance C_{mp} = 1 μF and a gap capacitance C_{gap} = 2200 pF (f_{maj} = 33.59 MHz).

The parallel-connected T_x terminal shown in Fig. 6-9 was composed of a square resonator with very small pads on either side of one of the two capacitor gaps to provide space for holes to accommodate wires that connect the terminal to an 8 mm length of RG402/U semi-rigid coaxial cable, terminated by a male SMA connector. Through one hole was threaded the

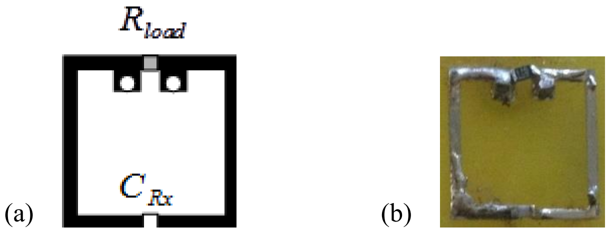

Fig. 6-10 *Description of the series-connected* R_x *terminal loop built for the experiment: (a) sketch of the* R_x *terminal with* C_{Rx} *and* R_{load} *labelled; (b) photograph taken of the* R_x *terminal with the two gap capacitances* C_{gap} *clearly displayed.*

central conductor of the semi-rigid cable, and through the other hole was threaded a wire of the same diameter as the central conductor, soldered onto the outer jacket of the semi-rigid cable. The T_x terminal used the equivalent-sized copper track as used in the waveguide and the same gap capacitance C_{gap} = 2200 pF, and so was tuned to the same resonant frequency of a major loop in the waveguide.

The series-connected R_x terminal shown in Fig. 6-10 was composed of an equivalent-sized square resonator to the one used in the T_x terminal, with the load resistance R_{load} placed over the gap connected to the two small pads and the receiver capacitance C_{Rx} placed over the other gap. The R_x terminal was also attached to an 8 mm length of RG402/U semi-rigid coaxial cable terminated by a male SMA connector.

There is an example of an optimal R_x terminal configuration being given in Section 6.3, which states that a square resonator with R_{load} = 0.5 Ω and C_{Rx} = 1500 pF over the two gaps creates the optimal R_x terminal offering maximum power efficiency at $f_{matching}$ = 25.9 MHz. In order to verify this analytical prediction, the experiment compared the power transfer efficiency achieved by R_x terminals built with a 0.5 Ω load resistance and seven different receiver capacitors: C_{Rx} = 1200 pF, 1390 pF, 1470 pF, 1520 pF, 1760 pF, 1820 pF and 2000 pF.

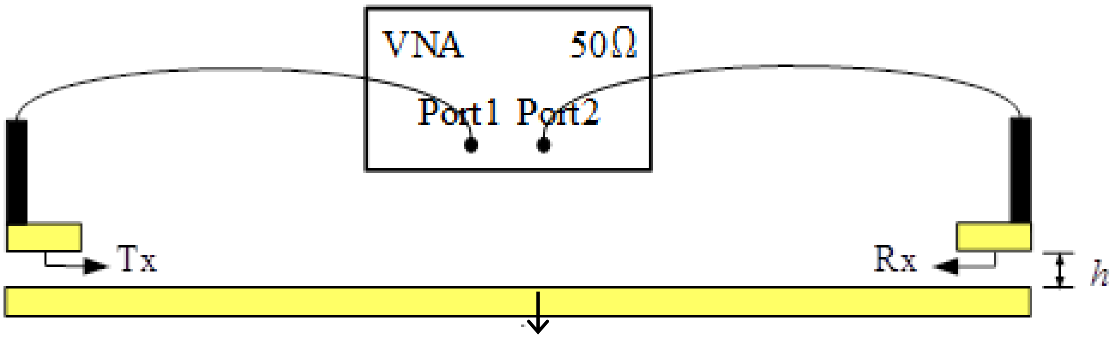

10-Element CCG Waveguide

Fig. 6-11 *Experimental apparatus with a demonstration power transfer system, composed of a 10-element CCG waveguide and* T_x *and* R_x *terminals connected to VNA for measurements of scattering parameters* S_{21} *and* S_{11}.

The experimental apparatus is shown in Fig. 6-11. The terminals were placed 1.6 mm away from the surface of the elements' copper tracks, and therefore gave M_{axial} = 7.2 nH. During the experiment, the two terminals T_x and R_x were both held in place by Perspex clamps and PTFE rods; T_x was fixed so as to align with the first major loop in the demonstration waveguide and R_x was fixed so as to align with the last major loop. The T_x and R_x terminals were connected to Ports 1 and 2, respectively, on a HP 8753ES VNA by means of 50 Ω coaxial cables to record the forward (S_{21}) and backward (S_{11}) scattering parameters which represent the transmission of power from one antenna to the other. The real and imaginary components of S_{21} and S_{11} were taken as the average of 16 scans of 1601 points between 50 kHz and 50 MHz.

6.6 Experimental Analysis

Fig. 6-12 shows the effective power transfer efficiency achieved with R_x terminals built with the seven different C_{Rx}, as calculated based on Eq. (6.6). It is worth noting that, in a realistic implementation, there will be some source losses reducing the overall system efficiency.

When analysing data obtained using a VNA, one must consider the mismatch between the impedance of the VNA and the actual load resistance. Eq. (6.6) combines the forward and backward scattering parameters, S_{21} and S_{11}, in order to convert the measured S_{21} to effective power transfer efficiency.

$$\eta = \frac{|S_{21}|^2}{(1-|S_{11}|^2)}(1+\frac{50\,\Omega}{R_{load}}) \tag{6.6}$$

where 50 Ω is the characteristic resistance of the VNA and the load resistance R_{load} is chosen as 0.5 Ω. Due to this substantial mismatch, the effective power efficiency is 100 times the measured value of S_{21}. The resistor component used for R_{load} = 0.5 Ω was a surface-mounted chip resistor manufactured by Bourns with a ±5% resistance tolerance, which can result in a ±5.2% error bar on the results, i.e. the effective efficiency η can vary between 32.34% and 35.88%, as labelled in Fig. 6-12. This result, however, does not include any source losses as the measured data have effectively been corrected by this process. In a realistic implementation, there will be some source losses which reduce the overall system efficiency below these values.

The R_x terminals used in this experiment were constructed with a fixed value of load resistance R_{load} = 0.5 Ω and seven different receiver capacitors C_{Rx}. The insert in Fig. 6-12 shows a satisfactory match between the predicted $f_{matching}$ and the experimental data, showing frequencies at which a peak efficiency was achieved for each C_{Rx}. Among these R_x terminals, the one built with C_{Rx} = 1520 pF gives the maximum power efficiency η_{max} = 34.11% at $f_{matching}$= 25.9 MHz.

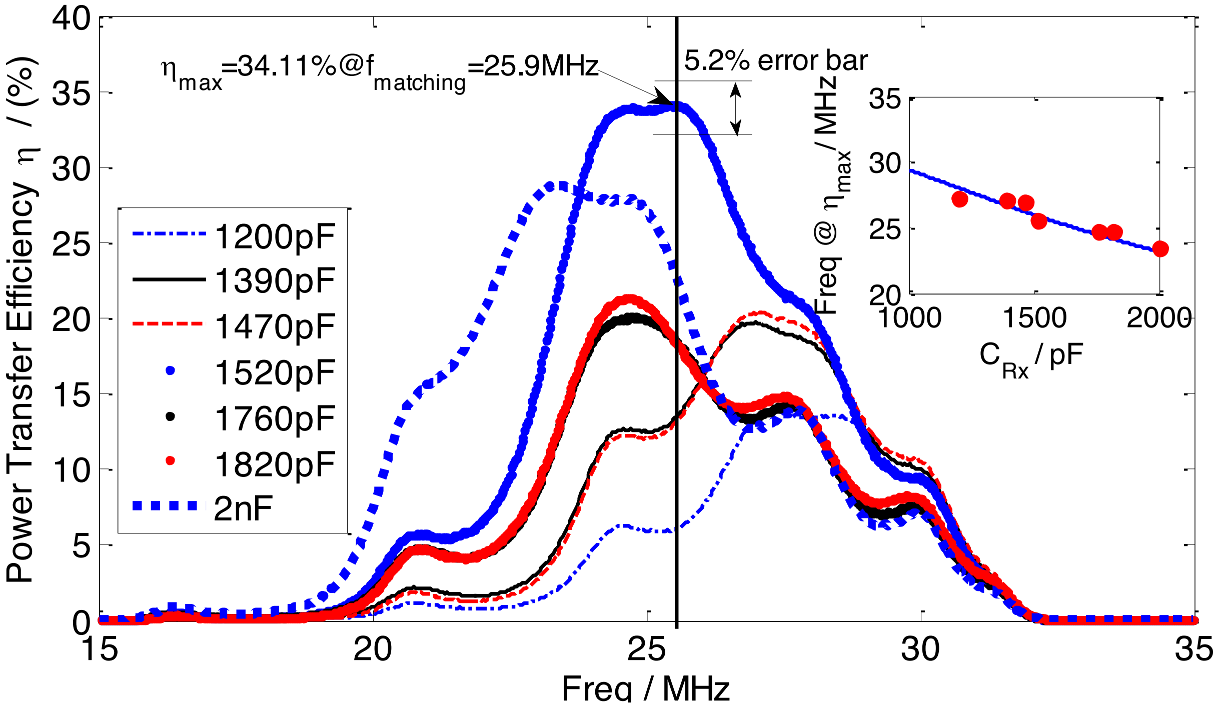

***Fig. 6-12** Power transfer efficiency measured with R_x terminals built with a 0.5 Ω load resistance and seven different receiver capacitors; the insert shows the frequencies at which maximum efficiency can be achieved using R_x terminals with various receiver capacitors; the red dots are experimental results and the blue line is the analytical prediction.*

One can calculate the analytical power transfer efficiency using similar circuit analysis as [89] for a CCG waveguide using this optimal Rx terminal design. The result is $\eta_{non-reflect}$ =34.5%, which corresponds to the experimental result η_{max} = 34.11% at $f_{matching}$=25.9MHz. It shows that reflectionless matching condition has been successfully achieved in the experiment with the optimal R_x terminal design proposed above. This study assumes a perfect voltage source which has no resistive loss. When calculating the power transfer efficiency for a realistic waveguide system, the loss from the source resistance should be considered.

In order to further improve the power transfer efficiency of this system, future work could focus on reducing the return loss by matching the T_x terminal under the maximum power transfer theorem. One should first find the source impedance effectively introduced by the T_x terminal into the first major loop via the mutual inductance M_{axial} according to Eq. (6.1).

The maximum power transfer theorem states that maximum power transfer occurs when the source impedance Z_{source} is equal to the complex conjugate of the input impedance Z_{input}, as calculated from Eq. (6.5).

The calculation of the optimum T_x design can follow the same procedure as used to find the optimum R_x design. A brief discussion is made here about the challenge of finding the optimum T_x design. As shown in Fig. 6-5, a relatively low resistance value (< 2 Ω) is required for both of the optimum R_x design and T_x design. This is not a problem for the design of R_x because the resistance from a metal loop is originally quite small (0.2 Ω), and the margin can be made up by using resistive components. However, this requirement of low resistance remains as a challenge for the design of T_x. The T_x terminal needs to be connected to a source which provides extra resistance. In this study, the characteristic resistance from the VNA is 50 Ω. This extra resistance, if larger than the resistance value required for matching, affects the efficiency of power injections. This constraint in finding the optimum T_x design could be further investigated in future work. A possible solution might be using transformer or connecting the power source directly to the first major loop.

One can also increase the efficiency when targeting at a lower frequency in the passband as the attenuation is lower; however, as shown in Fig. 6-5, the required R_{load} is negative when the target $f_{matching}$ decreases below 20.2 MHz. This can constrain terminal optimization seeking to offer maximum power efficiency.

6.7 Conclusions

This chapter has investigated the potential of 1-D CCG structures to be used as contactless power transfer devices and has focused on terminal optimizations under reflectionless matching conditions.

The concept of reflectionless matching was originally studied for MIW-based waveguides, which states that a non-reflective waveguide can be formed by inserting a terminating impedance that behaves as a semi-infinite line connected to the line end, absorbs all the incident power and gives to a finite structure the input property of an infinite line. In a general power transfer system, absorbing terminations are most undesirable, as they will lead to large fixed losses and seriously degrade overall efficiency unless they are themselves the loads to which power is being provided. However, a terminal whose load impedance is equalized to the terminating impedance offers the maximized power transfer efficiency.

The reflectionless matching condition has been studied analytically and verified experimentally in this study. The optimal terminal tested in these experiments has successfully stopped the reflection at the line end, as all the losses come from reflection at the T_x terminal and resistive loss along the line. The demonstration system gives the maximum power transfer efficiency of 34.11% at $f_{matching}$= 25.9 MHz.

In order to further improve the power transfer efficiency of this system, future work could focus on reducing the return loss by matching the T_x terminal under the maximum power transfer theorem. The calculation of the optimum T_x design can follow the same procedure as used to find the optimum R_x design. A brief discussion is made here about the constraint in finding the optimum T_x design and could be further investigated in future work.

The efficiency can also be increased when targeting a lower frequency in the passband as the attenuation is lower; however, the required load resistance turns negative when the target $f_{matching}$ decreases below a certain value. This can constrain terminal optimization seeking to offer maximum power efficiency.

CHAPTER 7

CONCLUSIONS AND FUTURE WORK

7.1 Conclusions

In the Introduction, the objective of this study is to build a more strongly coupled metamaterial waveguide, overcoming the limit of coupling strength in conventional almost purely magnetically coupled MIWs, and as such achieve more efficient contactless data and power transfer channels. Four challenges proposed in the Introduction with a view to achieving this objective, and the following conclusions will give answers to these four topics:

(i) Characterization of 1-D CCG metamaterial waveguides

In chapter 3, the dispersion characteristics and coupling mechanism of 1-D CCG waveguides were analysed via an equivalent circuit model derived in Section 3.1. The coupling mechanism of CCG waveguides can be explained as a competition between positive and negative coupling, and therefore generates two different propagation modes that were studied in Sections 3.4 and 3.5. When negative magnetic coupling dominates, CCG waveguides support MI backward wave propagation in much the same way that purely magnetically coupled waveguides do. When electric coupling dominates, CCG waveguides support EI forward wave propagation. When the two couplings cancel each other, CCG waveguides exhibit magnetic resonance without, however, permitting end-to-end energy propagation.

In the positive electric coupling dominated region, the pass-band keeps broadening with increased electric coupling strength. The analytical dispersion analysis predicts that a 1-D CCG waveguide built with parallel coupling capacitance C_{mp}=1μF can achieve the fractional bandwidth achieved of 192.4%. However, in the experiment as shown in Chapter 4, due to inefficient power injection from the source to the waveguide, the measured fractional bandwidth is only around 87.5%. This value has already largely exceeded the requirement of UWB channels. This clearly shows the potential of 1-D CCG waveguides to be used as UWB data transfer channels with low loss.

In Chapter 4, the dispersion characteristics are extracted from measured wave patterns by two different methods – the fitting method and the explicit derivation method.

The fitting method is proposed in this study, which considers the analytical waveform as a superposition between the spatial variation of probe-to-loop coupling and the wave-like current along the structure. This fitting method suffers from slow computational speed. However, this method may be rather useful when the measurement set-up is coarse, for instance when the receiver probe is not placed exactly above the centre of loops to be measured. This method may be less sensitive to measurement misalignments because the calculation uses all the available measured current along the line and find the best fit based on a χ^2 criteria.

The explicit derivation method is originally proposed in [68] and offers the benefits of explicit relation between current and dispersion characteristics, and fast computation speed.

(ii) Derivation of a mixed coupling model

In Section 3.6, an existing analytical model from previous study [68] is adjusted and then applied to 1-D CCG waveguides. The adjustment made in order to apply this model to CCG waveguides includes: (i) the resonance capacitance and the mutual capacitance are no longer calculated based on the geometry of structures, instead they are expressed as functions of capacitive component values used in CCG structures; (ii) the calculation of the resonance capacitance is no longer based on an isolated resonator, instead it considers the fact that the electric coupling between two resonators will affect the value of the resonance capacitance.

The first adjustment is made based on the very nature of CCG waveguide in which electric coupling is determined by capacitive components used in CCG structures. The main contribution of this adjustment is to understand the formation of the resonance capacitance C_{res} and the mutual capacitance K. The electric coupling is analysed with the aid of a four-electrode model, including coupling capacitance included in both parallel and diagonal configurations. It is shown that the parallel coupling capacitance contributes to positive electric coupling; while the diagonal coupling capacitance contributes to negative electric coupling. Although only parallel capacitance is used in this study, based on this understanding, future studies could explore various ways to introduce additional electric couplings into waveguides similar to CCGs, for example a structure built with diagonal capacitances only and a structure includes both diagonal and parallel capacitances.

The second adjustment extends the original model to cases where the effect of electric coupling on the value of resonance capacitance is not negligible.

This adjusted analytical model is verified by comparing to the dispersion equation derived from circuit analysis. It shows that parallel coupling capacitance introduces positive electric coupling which carries forward EI waves; while diagonal coupling capacitance introduces negative electric coupling which carries backward EI waves.

When applying this adjusted model to 1-D CCGs, one can simplify the bi-atomic model to a monoatomic model, in which the original minor loops are only considered as electric coupling devices interlinking adjacent major loops. After being simplified to a monoatomic model, the derivation process of dispersion equations, impedance matrix, as well as the dimension extension to 2-D structures can be much simplified as shown in Section 3.7.

This adjusted model helps to evaluate the respective contributions of the magnetic and electric couplings. Therefore, it allows the design of many mixed coupling waveguides, like 1-D CCGs, to be readily adjusted to suit the conditions and requirements of various dispersion characteristics. This adjusted model is easily adjustable to metamaterial elements of arbitrary shape, if, instead of relying on component values, geometry-based values are used.

(iii) Dimensional extension to 2-D CCG waveguide surfaces

In chapter 5, the study of the 1-D CCG waveguide proceeded to its 2-D expansion – the 2-D CCG waveguide surface. Sections 5.4 and 5.5 explored, both analytically and experimentally, the dispersion characteristics of waves propagating along three different paths in a 2-D CCG waveguide: the 'edge path', the 'diagonal <11> path' and the 'axial <01/10> path'. The 2-D CCG exhibited similar dispersion features to the 1-D device, which demonstrates that all three paths can support either backward MI or forward EI wave propagation when negative magnetic coupling or positive electric coupling dominates and can display no-propagation points when the two types of coupling cancel out.

Considering both bandwidth and dispersion performance, the two inside paths – the diagonal <11> path and the axial <01/10> path – provide a less dispersive and 'lossy' propagation channel, with significantly greater bandwidth performance, in comparison with the edge path carrying surface waves. The two inside paths exhibit comparable dispersion and attenuation performance to the 1-D 2C CCG and provide reasonably good bandwidth performance. The analytical fractional bandwidth of the diagonal <11> path and the axial <01/10> path are 187.6% and 186.4% respectively; however the measured ones are reduced to 83% and 81% respectively. This is due to the inefficient power injection at the lower part of the predicted passbands caused by the impedance mismatch between the source and the waveguide. However, these values still exceeds the 20% requirement of UWB channels. The two inside paths provide good examples of data channels in a 2-D CCG with low loss and dispersion but high data capacity and speed. Channelization can be used to get several sub-channels with less dispersion and group delay in a similar fashion to the 1-D CCG device.

When comparing the two 1-D cases, the 1-D 2C CCG shows improved performance in terms of attenuation, dispersion and bandwidth, and offers great potential to be used as a 1-D contactless data transfer channel.

In Section 5.7, the current distributions over the 2-D CCG waveguide surface were studied both analytically and experimentally and found to be very sensitive to frequency variation. Such frequency-dependent current distribution behaviour of the 2-D CCG gives it the potential to be used as a 2-D contactless data transfer channel offering a robust multipath environment for multiple terminal connections. Frequency channelization can be applied in the 2-D CCG waveguide surface, allowing waves of different frequency range to propagate along various paths and to be excited and picked up by terminals at different locations.

(iv) Explore the potential of CCG in contactless data and power transfer

This study has explored the potential for using CCG devices as 1-D or 2-D data transfer channels which offer a realistic potential to link near-field coupled devices at high bandwidth and low loss. For example, a 1-D CCG waveguide can replace wired connections between electronic devices; a 2-D CCG waveguide surface provides a multipath environment allowing multi-terminal access to electronics devices and can be readily embedded into fabrics to enhance body area networking [13]. Furthermore, such contactless metamaterial waveguides may also serve as track-free data buses for inter-chip, and perhaps intra-chip, communications [9], replacing the PCB in electronics systems if the ICs in such systems are capable of launching and detecting MI and EI waves. Devices must remain sufficiently small in order to be incorporated into these applications. As elements made of smaller metallic loops have limited inductance, eventually relatively larger-value capacitors are needed to keep the resonance frequency within the frequency range of interests and greater resistive loss is encountered as the dissipation factor of a capacitive component is proportional to its capacitance [101]. One might consider building the capacitors with prototype cables of copper-clad polyimide, as originally proposed in [100]; however, the use of geometric capacitance compromises the applicability of metamaterial waveguides for two reasons: (i) it takes up much more space than chip capacitors (a 20 pF capacitor fabricated via this method can be up to 2 m in length) and (ii) it makes waveguides very susceptible to external dielectric objects. Therefore, there will perhaps always be a trade-off between physical size and performance loss for this type of waveguide.

Chapter 6 investigated the potential of 1-D CCG structures to be used as contactless power transfer devices, focusing on terminal optimizations with a view to offering maximized power transfer efficiency.

Section 6.2 proposed that the optimal terminal can be achieved under the reflectionless matching condition, which states that a non-reflective waveguide can be formed by inserting a terminating impedance that behaves as a semi-infinite line and gives to a finite structure the input property of an infinite line. Section 6.4 showed that optimal terminals suppress standing waves around the matching frequencies, removing the strong frequency variation in input impedance generated in the unloaded finite line at their operating frequencies.

In contrast to data transfer applications which demand wide passbands, an efficient power transfer system only needs to transfer power at a single frequency, but with high power transfer efficiency. The study of terminal optimization allows for deducing the specific resistive and capacitive components required for each matching frequency. When choosing the matching frequency, one can see that targeting at a lower frequency in the passband gives lower attenuation, and therefore higher power transfer efficiency. However, the required load resistance can turn negative, and therefore becomes impossible to realize when the targeting matching frequency decreases below a certain value. This can constrain terminal optimization seeking to offer maximum power efficiency.

In Section 6.5, a simple experiment was conducted which proved that an R_x terminal built according to the analytical model can successfully absorb all the incident power at the line end. The demonstration system used in this study included a 10-element CCG-based waveguide, an unmatched parallel-connected T_x terminal and a well-loaded series-connected R_x terminal. The demonstration system gives the maximum power transfer efficiency of 34.11% at $f_{matching}$= 25.9 MHz.

7.2 Future Work

This study proposes a mixed coupling model for structures incorporating both magnetic and electric coupling. According to the predictions of this model, electric coupling can be either positive or negative depending on whether parallel or diagonal coupling capacitors are in use. Having analysed CCGs built with parallel coupling capacitors and offering positive electric coupling, a natural step for future study is to design a new variant of the CCG using diagonal coupling capacitors and offering negative electric coupling. This new variant would increase the flexibility of CCG designs suiting different requirements.

An important feature of CCG devices is the appearance of a no-propagation point when positive electric and negative magnetic coupling exactly cancel each other; however, this is rather difficult to achieve. The fabrication tolerances of capacitive components would introduce uncertainties in the electric coupling strength. According to the mixed coupling model, the parallel and diagonal coupling capacitances contribute to positive and negative electric coupling, respectively, so the two compensate each other when both exist in a circuit. Therefore, one may be able to design a structure in which both the sign and the strength of the electric coupling are flexible so as to be altered by carefully adjusting the parallel and diagonal coupling capacitances. This structure increases the chances of achieving the no-propagation point. At this point, CCG waveguides still exhibit magnetic resonances without permitting end-to-end energy propagation. This property of CCGs could be exploited in super lens imaging applications in the future.

There is an important phenomenon observed in both 1-D and 2-D CCG structures - the measured passband is actually narrower than the predictions. This is due to the inefficient power injection caused by the impedance mismatch between the transmitter probe which directly connected to the source and the waveguide. Future work should explore on how to inject power efficiently into the waveguide by designing a transmitter matching with the input impedance of the waveguide under maximum power transfer theorem. It can be difficult to use one transmitter to match to the waveguide across the entire passband; therefore frequency channelization can be explored in order to increase power injection efficiency in sub-channels.

In this study, an optimal terminal configuration was derived and was proved to work experimentally, which required a load resistance of 0.5 Ω. Such low resistance can be difficult to get when considering the availability and fabrication tolerance of resistive components. If one can design a structure where a matching load is exactly 50 Ω, the optimal terminal might be much easier to achieve, as it can be simply achieved by connecting to a 50 Ω coaxial cable and load.

When choosing the matching frequency, targeting at a lower frequency in the passband gives lower attenuation and therefore higher power transfer efficiency. However, the required load resistance turns negative below a certain frequency, and therefore becomes difficult to realize. One possible solution to achieving negative resistance might be the use of an impedance inverter circuit [102]; however, the use of active components such as amplifiers in such a circuit would introduce constraints on the applicable frequency range for CCG-based power transfer systems. It would be very helpful if this critical frequency could be described mathematically, so that one might explore the reasons for the negative resistance and be able to push it below the frequency at which minimum attenuation, and therefore maximum power transfer efficiency, can be achieved.

This page is intentionally left blank

Table of Key Symbols

μ	Permeability
ε	Permittivity
Q	Quality factor
q	Charge induced by electric coupling
$L_{MIW}, C_{MIW,} R_{MIW,}$	Inductance, capacitance, and resistance of a MIW resonator
$L_C, C_C,$	Inductance and capacitance of a CSSR resonator
$C_M, C_G,$	Mutual-inductance and capacitance to ground of a CSSR resonator
λ_0	Free space wavelength
γ	Propagation constant
γ_x,γ_y	Propagation constant in x axis (subscript x) and y axis (subscript y)
α	Attenuation coefficient
β	Wave number
Z_{maj}	Impedance of a major loop (subscript maj)
Z_{minp}, Z_{mind}	Impedance of a parallel-configured minor loop (subscript minp), and a diagonal-configured minor loop (subscript mind)
X_{share}	Impedance of the common branch shared between adjacent major and minor loops
M	Mutual inductance between nearest neighbouring MIW resonators/ between nearest neighbouring CCG major loops
M_{minp}, M_{mind}	Mutual inductance between adjacent major and parallel-configured minor loop (subscript minp); between adjacent major and diagonal-

	configured minor loop (subscript mind)
R	Resistance associated with each side of a major loop
L	Inductance associated with each side of a major loop
C_{gap}	Gap capacitance
C_{mp},C_{md}	Parallel coupling capacitance (subscript mp) and diagonal coupling capacitance (subscript md)
i_m	Current circulating in the mth major loop
i'_m	Analytical current form from the waveform fitting method
j_m	Current circulating in the mth parallel-configured minor loop
d_m	Current circulating in the mth diagonal-configured minor loop
I_0	Current amplitudes at the first major loop
I_r	Current amplitudes at the last major loop at which the reflected wave starts to propagate
J_0	Current amplitudes at the first parallel-configured minor loop
f_{L1}, f_{L2}	Frequency bounds of the lower passband
f_{H1}, f_{H2}	Frequency bounds of the higher passband
f_{maj}, f_{min}	Resonant frequency of a major loop (subscript maj) and a minor loop (subscript min)
C_{cross}	Crossing-over capacitance at which there is no propagation along CCG waveguides
v_g, v_p	Group velocity (subscript g) and phase velocity (subscript p)
v_{gpeak}	Peak group velocity
α_{min}	Minimum attenuation

$\varepsilon_{maj}, \varepsilon_{min}$	Electromotive force induced in a major loop through magnetic coupling between neighbouring major loops (subscript maj) and through magnetic coupling between adjacent major and minor loop (subscript min)
ε_M	The total electromotive force induced by magnetic coupling in a major loop
V_E	The voltage passed to a major loop through electric coupling
V_{total}	The total voltage passed to a major loop via overall effect of electric coupling and magnetic coupling
k_m, k_e	Magnetic coupling coefficient (subscript m) and electric coupling coefficient (subscript e)
k_{total}	Mixed coupling coefficient
k_{e_4c}, k_{e_2c}	Electric coupling coefficient for 1-D 4C CCG (subscript e_4c) and 1-D 2C CCG (subscript e_2c)
L_{self}	Self-inductance of a resonator
L_{res}	Resonance inductance of a resonator
C_{res}	Resonance capacitance of a resonator
K	Mutual capacitance of a resonator
C_{meff}	Effective mutual capacitance of a resonator
C_{self}	Self-capacitance of a coupled resonator used in mixed coupling model and purely capacitive model
$\boldsymbol{Z}$	Impedance matrix
$\boldsymbol{V}$	voltage matrix
$\boldsymbol{I}$	Current matrix

Z_0	Self-impedance of a single element in metamaterial waveguide
Z_m	Mutual-impedance of a single element in metamaterial waveguide
$\Gamma_{probe-loop}$	Probe-to-loop coupling parameter
M_{axial}	Mutual inductance between transmitter/ receiver probe and the major loop coupled to the probe
M_{diag}	Mutual inductance between diagonally adjacent major loops/ resonators in two dimensional waveguide surface
r	The ratio between the shared inductance to the total inductance of a major loop
Z_{T-MIW}	Terminating Impedance for one dimensional MIW structure
Z_{T-CCG}	Terminating Impedance for one dimensional CCG structure
R_{T-CCG}	The real part of CCG terminating impedance
X_{T-CCG}	The imaginary part of CCG terminating impedance
Z_{input}	Input impedance of the waveguide
Z_{load}	Effective load impedance inserted by the receiver to the waveguide
R_{load}	Resistive (real) part of Z_{load}
Z_{Rx}, C_{Rx}, L_{Rx}, R_{Rx}	Impedance, capacitance, inductance and resistance required to build a receiver which matches to the waveguide input impedance
$f_{matching}$	The matching frequency at which the reflectionless matching condition can be achieved
η	Power transfer efficiency
η_{max}	Maximum power transfer efficiency
S_{21}	Forward scattering parameter

S_{11}	Backward scattering parameter

Table of Abbreviations

PCB	Printed circuit board
MIW	Magneto-inductive waveguide
MI wave	Magneto-inductive wave
1-D	One dimensional
2-D	Two dimensional
CCG	Capacitor-connected Grid
EI wave	Electro-inductive wave
EM	Electromagnetic
LHM	Left-handed material
SRR	Split ring resonator
EIW	Electro-inductive waveguide
CSRR	Complementary split ring resonator
CSSRR	Complementary square split ring resonator
MRI	Magnetic resonance imaging
SNR	Signal-to-noise ratio
WPT	Wireless power transfer

IC	Integrated Circuit
BAN	Body-area networking
FBW	Fractional Bandwidth
UWB	Ultra-Wideband
PTFE	Polytetrafluoroethylene
VNA	Vector network analyser
GPIB	General purpose interface bus
USB	Universal serial bus

List of Figures

List of Tables

BILIOGRAPHY

[1] A. Kurs, A. Karalis, R. Moffatt, and J. D. Joannopoulos, “Wireless power transfer via strongly coupled magnetic resonances,” *Science (80-.).*, vol. 317, no. 5834, pp. 83–86, 2007.

[2] S. Luan, A. Eftekhar, O. H. Murphy, and T. G. Constandinou, “Towards an inductively coupled power/data link for bondpad-less silicon chips,” in *Proceedings - IEEE International Symposium on Circuits and Systems*, 2011, pp. 2597–2600.

[3] S. Kim, D. H. Jung, J. J. Kim, B. Bae, S. Kong, S. Ahn, J. Kim, and J. Kim, “High-Efficiency PCB- and Package-Level Wireless Power Transfer Interconnection Scheme Using Magnetic Field Resonance Coupling,” *IEEE Transactions on Components, Packaging and Manufacturing Technology*, 2015.

[4] B. L. Cannon, J. F. Hoburg, D. D. Stancil, and S. C. Goldstein, “Magnetic Resonant Coupling As a Potential Means for Wireless Power Transfer to Multiple Small Receivers,” *IEEE Trans. Power Electron.*, vol. 24, no. 7, pp. 1819–1825, 2009.

[5] C. J. Stevens, “Some consequences of the properties of metamaterials for wireless power transfer,” in *2015 9th International Congress on Advanced Electromagnetic Materials in Microwaves and Optics (METAMATERIALS)*, 2015, pp. 295–297.

[6] W. Cai and V. Shalaev, *Optical Metamaterials*. New York, NY: Springer New York, 2010.

[7] E. Shamonina, V. A. Kalinin, K. H. Ringhofer, and L. Solymar, “Magneto-inductive waveguide,” *Electron. Lett.*, vol. 38, no. 8, p. 371, 2002.

[8] C. W. T. Chan and C. J. Stevens, “Two-dimensional magneto-inductive wave data structures,” *{...} 5th Eur. Conf.*, 2011.

[9] C. J. Stevens, C. W. T. Chan, K. Stamatis, and D. J. Edwards, “Magnetic Metamaterials as 1-D Data Transfer Channels: An Application for Magneto-Inductive Waves,” *IEEE Trans. Microw. Theory Tech.*, vol. 58, no. 5, pp. 1248–1256, 2010.

[10] C. J. Stevens, “A magneto-inductive wave wireless power transfer device,” *Wirel. Power Transf.*, vol. 2, no. 01, pp. 51–59, 2015.

[11] C. J. Stevens, “Magnetoinductive Waves and Wireless Power Transfer,” *Power Electron. IEEE Trans.*, vol. 30, no. 11, pp. 6182–6190, 2015.

[12] O. Sydoruk, A. Radkovskaya, O. Zhuromskyy, E. Shamonina, M. Shamonin, C. J. Stevens, G. Faulkner, D. J. Edwards, and L. Solymar, “Tailoring the near-field guiding properties of magnetic metamaterials with two resonant elements per unit cell,” *Phys. Rev. B*, vol. 73, no. 22, p. 224406, 2006.

[13] C. W. T. Chan, “Magneto-inductive wave data communications systems,” University of Oxford, 2014.

[14] A. Radkovskaya, O. Sydoruk, M. Shamonin, C. J. Stevens, G. Faulkner, D. J. Edwards, E. Shamonina, and L. Solymar, “Transmission properties of two shifted

magnetoinductive waveguides," *Microw. Opt. Technol. Lett.*, vol. 49, no. 5, pp. 1054–1058, 2007.

[15] R. R. A. Syms, I. R. Young, and L. Solymar, "Low-loss magneto-inductive waveguides," *J. Phys. D. Appl. Phys.*, vol. 39, no. 18, pp. 3945–3951, 2006.

[16] E. Tatartschuk, N. Gneiding, F. Hesmer, A. Radkovskaya, and E. Shamonina, "Mapping inter-element coupling in metamaterials: Scaling down to infrared," *J. Appl. {...}*, vol. 111, no. 9, p. 94904, 2012.

[17] L. Solymar, D. Walsh, and R. R. A. Syms, *Electrical Properties of Materials*. Oxford: Oxford University Press, 2014.

[18] J. D. Joannopoulos, P. R. Villeneuve, and S. Fan, "Photonic crystals: putting a new twist on light," *Nature*, vol. 386, no. 6621, pp. 143–149, 1997.

[19] C. M. Soukoulis, "Photonic Band Gap Materials," in *Diffuse Waves in Complex Media*, Dordrecht: Springer Netherlands, 1999, pp. 93–107.

[20] J. D. Joannopoulos, S. G. Johnson, J. N. Winn, and R. D. Meade, *Photonic Crystals*. Princeton University Press, 2011.

[21] E. Yablonovitch, "Photonic band-gap structures," *JOSA B*, vol. 10, no. 2, pp. 283–295, 1993.

[22] P. R. Villeneuve, J. S. Foresi, J. Ferrera, E. R. Thoen, G. Steinmeyer, S. Fan, J. D. Joannopoulos, L. C. Kimerling, H. I. Smith, and E. P. Ippen, "Photonic-bandgap microcavities in optical waveguides," *Nature*, vol. 390, no. 6656, pp. 143–145, 1997.

[23] G. V Eleftheriades and K. G. Balmain, *Negative-Refraction Metamaterials*. John Wiley {&} Sons, 2005.

[24] N. Engheta and R. W. Ziolkowski, *Metamaterials*. Hoboken, NJ, USA: John Wiley {&} Sons, 2006.

[25] C. Caloz and T. Itoh, *Electromagnetic Metamaterials*. Hoboken, NJ, USA: John Wiley {&} Sons, 2005.

[26] A. K. Sarychev and V. M. Shalaev, *Electrodynamics of Metamaterials*. WORLD SCIENTIFIC, 2007.

[27] R. B. Wehrspohn, H. S. Kitzerow, and K. Busch, Eds., *Nanophotonic Materials*. Weinheim, Germany: Wiley-VCH Verlag GmbH {&} Co. KGaA, 2008.

[28] R. Marqués, F. Martín, and M. Sorolla, "Metamaterials with negative parameters: Theory, design and microwave applications," *Mater. Today*, vol. 11, no. 3, p. 57, 2008.

[29] L. Solymar and E. Shamonina, *Waves in Metamaterials*. Oxford University Press, 2009.

[30] C. Denz, S. Flach, and Y. Kivshar, *Nonlinearities in Periodic Structures and Metamaterials*, vol. 150. Berlin, Heidelberg: Springer, 2010.

[31] V. G. Veselago, "The Electrodynamics of Substances with Simultaneously Negative

Values of ε and μ,” *Sov. Phys. Uspekhi*, vol. 10, no. 4, pp. 509–514, 2007.

[32] E. Shamonina and L. Solymar, “Properties of magnetically coupled metamaterial elements,” *J. Magn. Magn. Mater.*, vol. 300, no. 1, pp. 38–43, 2006.

[33] J. B. Pendry, A. J. Holden, D. J. Robbins, and W. J. Stewart, “Low frequency plasmons in thin-wire structures,” *J. Phys. Condens. Matter*, vol. 10, no. 22, pp. 4785–4809, 1999.

[34] J. B. Pendry, A. J. Holden, W. J. Stewart, and I. Youngs, “Extremely Low Frequency Plasmons in Metallic Mesostructures,” *Phys. Rev. Lett.*, vol. 76, no. 25, pp. 4773–4776, 1996.

[35] J. B. Pendry, A. J. Holden, D. J. Robbins, and W. J. Stewart, “Magnetism from conductors and enhanced nonlinear phenomena,” *IEEE Trans. Microw. Theory Tech.*, vol. 47, no. 11, pp. 2075–2084, 1999.

[36] D. R. Smith, W. J. Padilla, D. C. Vier, S. C. Nemat-Nasser, and S. Schultz, “Composite Medium with Simultaneously Negative Permeability and Permittivity,” *Phys. Rev. Lett.*, vol. 84, no. 18, pp. 4184–4187, 2000.

[37] D. R. Smith and N. Kroll, “Negative Refractive Index in Left-Handed Materials,” *Phys. Rev. Lett.*, vol. 85, no. 14, pp. 2933–2936, 2000.

[38] R. A. Shelby, “Experimental Verification of a Negative Index of Refraction,” *Science (80-.).*, vol. 292, no. 5514, pp. 77–79, 2001.

[39] J. B. Pendry, “Negative Refraction Makes a Perfect Lens,” *Phys. Rev. Lett.*, vol. 85, no. 18, pp. 3966–3969, 2000.

[40] G. Dolling, “Simultaneous Negative Phase and Group Velocity of Light in a Metamaterial,” *Science (80-.).*, vol. 312, no. 5775, pp. 892–894, 2006.

[41] D. R. Smith, “Metamaterials and Negative Refractive Index,” *Science (80-.).*, vol. 305, no. 5685, pp. 788–792, 2004.

[42] J. B. Pendry, D. Schurig, and D. R. Smith, “Controlling Electromagnetic Fields,” *Science (80-.).*, vol. 312, no. 5781, pp. 1780–1782, 2006.

[43] J. B. Pendry, “Time Reversal and Negative Refraction,” *Science (80-.).*, vol. 322, no. 5898, pp. 71–73, 2008.

[44] T. J. Yen, “Terahertz Magnetic Response from Artificial Materials,” *Science (80-.).*, vol. 303, no. 5663, pp. 1494–1496, 2004.

[45] S. Linden, “Magnetic Response of Metamaterials at 100 Terahertz,” *Science (80-.).*, vol. 306, no. 5700, pp. 1351–1353, 2004.

[46] C. M. Soukoulis, S. Linden, and M. Wegener, “PHYSICS: Negative Refractive Index at Optical Wavelengths,” *Science (80-.).*, vol. 315, no. 5808, pp. 47–49, 2007.

[47] J. Yao, Z. Liu, Y. Liu, Y. Wang, C. Sun, G. Bartal, A. M. Stacy, and X. Zhang, “Optical Negative Refraction in Bulk Metamaterials of Nanowires,” *Science (80-.).*,

vol. 321, no. 5891, p. 930, 2008.

[48] D. Schurig, J. J. Mock, B. J. Justice, S. A. Cummer, J. B. Pendry, A. F. Starr, and D. R. Smith, “Metamaterial Electromagnetic Cloak at Microwave Frequencies,” *Science (80-.).*, vol. 314, no. 5801, pp. 977–980, 2006.

[49] R. Liu, C. Ji, J. J. Mock, J. Y. Chin, T. J. Cui, and D. R. Smith, “Broadband Ground-Plane Cloak,” *Science (80-.).*, vol. 323, no. 5912, pp. 366–369, 2009.

[50] T. Ergin, N. Stenger, P. Brenner, J. B. Pendry, and M. Wegener, “Three-Dimensional Invisibility Cloak at Optical Wavelengths,” *Science (80-.).*, vol. 328, no. 5976, pp. 337–339, 2010.

[51] B. Wood, J. B. Pendry, and D. P. Tsai, “Directed subwavelength imaging using a layered metal-dielectric system,” *Phys. Rev. B*, vol. 74, no. 11, p. 115116, 2006.

[52] I. I. Smolyaninov, Y. J. Hung, and C. C. Davis, “Magnifying superlens in the visible frequency range,” *arXiv.org*, no. 5819, pp. 1699–1701, 2006.

[53] Z. Liu, H. Lee, Y. Xiong, C. Sun, and X. Zhang, “Far-Field Optical Hyperlens Magnifying Sub-Diffraction-Limited Objects,” *Science (80-.).*, vol. 315, no. 5819, p. 1686, 2007.

[54] T. Driscoll, H. T. Kim, B. G. Chae, B. J. Kim, Y. W. Lee, N. M. Jokerst, S. Palit, D. R. Smith, M. Di Ventra, and D. N. Basov, “Memory Metamaterials,” *Science (80-.).*, vol. 325, no. 5947, pp. 1518–1521, 2009.

[55] C. M. Soukoulis and M. Wegener, “Optical Metamaterials--More Bulky and Less Lossy,” *Science (80-.).*, vol. 330, no. 6011, pp. 1633–1634, 2010.

[56] J.-S. G. Hong and M. J. Lancaster, *Microstrip Filters for RF / Microwave Applications*. New York, USA: John Wiley {&} Sons, 2004.

[57] A. A. Radkovskaya, V. N. Prudnikov, O. A. Kotel\textquoterightnikova, and A. P. Sukhorukov, “Waves in magnetic metamaterials with strong coupling of elements,” *Phys. Wave Phenom.*, vol. 21, no. 1, pp. 41–47, 2013.

[58] F. Capolino, *Theory and Phenomena of Metamaterials*. CRC Press, 2009.

[59] F. Hesmer, E. Tatartschuk, O. Zhuromskyy, A. A. Radkovskaya, M. Shamonin, T. Hao, C. J. Stevens, G. Faulkner, D. J. Edwards, and E. Shamonina, “Coupling mechanisms for split ring resonators: Theory and experiment,” *{...} status solidi*, vol. 244, no. 4, pp. 1170–1175, 2007.

[60] V. Lomanets, O. Zhuromskyy, G. Onishchukov, and U. Peschel, “Electrical circuit model of arrays of resonant elements,” *Phys. Rev. B*, vol. 85, no. 12, p. 125110, 2012.

[61] M. Beruete, F. Falcone, M. J. Freire, R. Marqués, and J. D. Baena, “Electroinductive waves in chains of complementary metamaterial elements,” *Appl. Phys. Lett.*, vol. 88, no. 8, p. 83503, 2006.

[62] E. Shamonina and L. Solymar, “Magneto-inductive waves supported by metamaterial elements: components for a one-dimensional waveguide,” *J. Phys. D. Appl. Phys.*, vol.

37, no. 3, pp. 362–367, 2004.

[63] E. Shamonina, V. A. Kalinin, K. H. Ringhofer, and L. Solymar, “Magnetoinductive waves in one, two, and three dimensions,” *J. Appl. {...}*, vol. 92, no. 10, pp. 6252–6261, 2002.

[64] M. C. K. Wiltshire, E. Shamonina, I. R. Young, and L. Solymar, “Dispersion characteristics of magneto-inductive waves: comparison between theory and experiment,” *Electron. Lett.*, vol. 39, no. 2, p. 215, 2003.

[65] S. Hrabar, Z. Ereš, and J. Bartolić, “Capacitively Loaded Loop as Basic Element of Negative Permeability Meta-material,” in *32nd European Microwave Conference, 2002*, 2002, pp. 1–4.

[66] R. Marqués, F. Medina, and R. Rafii-El-Idrissi, “Role of bianisotropy in negative permeability and left-handed metamaterials,” *Phys. Rev. B*, vol. 65, no. 14, p. 144440, 2002.

[67] A. Radkovskaya, M. Shamonin, C. J. Stevens, G. Faulkner, D. J. Edwards, E. Shamonina, and L. Solymar, “An experimental study of the properties of magnetoinductive waves in the presence of retardation,” *J. Magn. Magn. Mater.*, vol. 300, no. 1, pp. 29–32, 2006.

[68] A. Radkovskaya, O. Sydoruk, M. Shamonin, E. Shamonina, C. J. Stevens, G. Faulkner, D. J. Edwards, and L. Solymar, “Experimental study of a bi-periodic magnetoinductive waveguide: comparison with theory,” *IET Microwaves, Antennas {&} Propag.*, vol. 1, no. 1, p. 80, 2007.

[69] J. D. Baena, J. Bonache, F. Martín, R. M. Sillero, F. Falcone, T. Lopetegi, M. A. G. Laso, J. Garcia-Garcia, I. Gil, M. F. Portillo, and M. Sorolla, “Equivalent-circuit models for split-ring resonators and complementary split-ring resonators coupled to planar transmission lines,” *IEEE Trans. Microw. Theory Tech.*, vol. 53, no. 4, pp. 1451–1461, 2005.

[70] F. Falcone, T. Lopetegi, M. A. G. Laso, J. D. Baena, J. Bonache, M. Beruete, R. Marqués, F. Martín, and M. Sorolla, “Babinet Principle Applied to the Design of Metasurfaces and Metamaterials,” *Phys. Rev. Lett.*, vol. 93, no. 19, p. 197401, 2004.

[71] M. J. Freire, R. Marqués, F. Medina, M. A. G. Laso, and F. Martín, “Planar magnetoinductive wave transducers: Theory and applications,” *Appl. Phys. Lett.*, vol. 85, no. 19, pp. 4439–4441, 2004.

[72] M. C. K. Wiltshire, “Microstructured Magnetic Materials for RF Flux Guides in Magnetic Resonance Imaging,” *Science (80-.).*, vol. 291, no. 5505, pp. 849–851, 2001.

[73] E. Shamonina, “Slow waves in magnetic metamaterials: history, fundamentals and applications,” *{...} status solidi*, vol. 245, no. 8, pp. 1471–1482, 2008.

[74] M. J. Freire and R. Marqués, “Planar magnetoinductive lens for three-dimensional subwavelength imaging,” *Appl. Phys. Lett.*, vol. 86, no. 18, p. 182505, 2005.

[75] I. S. Nefedov and S. A. Tretyakov, “On potential applications of metamaterials for the

design of broadband phase shifters," *Microw. Opt. Technol. Lett.*, vol. 45, no. 2, pp. 98–102, 2005.

[76] R. R. A. Syms, L. Solymar, and E. Shamonina, "Absorbing terminations for magneto-inductive waveguides," *Microwaves*, vol. 152, no. 2, p. 77, 2005.

[77] O. Zhuromskyy, E. Shamonina, and L. Solymar, "2D metamaterials with hexagonal structure: spatial resonances and near field imaging," *Opt. Express*, vol. 13, no. 23, pp. 9299–9309, 2005.

[78] P. A. Belov and C. R. Simovski, "Subwavelength metallic waveguides loaded by uniaxial resonant scatterers," *Phys. Rev. E*, vol. 72, no. 3, p. 36618, 2005.

[79] R. R. A. Syms, E. Shamonina, and L. Solymar, "Magneto-inductive waveguide devices," *Microwaves*, vol. 153, no. 2, p. 111, 2006.

[80] O. Sydoruk, M. Shamonin, A. Radkovskaya, O. Zhuromskyy, E. Shamonina, R. Trautner, C. J. Stevens, G. Faulkner, D. J. Edwards, and L. Solymar, "Mechanism of subwavelength imaging with bilayered magnetic metamaterials: Theory and experiment," *J. Appl. {...}*, vol. 101, no. 7, p. 73903, 2007.

[81] N. Tesla, "The Transmission of Electric Energy without Wire," *Sci. Am.*, vol. 57, no. 1483supp, pp. 23760–23761, 1904.

[82] S. Y. R. Hui, W. Zhong, and C. K. Lee, "A Critical Review of Recent Progress in Mid-Range Wireless Power Transfer," *IEEE Trans. Power Electron.*, vol. 29, no. 9, pp. 4500–4511, 2014.

[83] Y. Lim, H. Tang, S. Lim, and J. Park, "An Adaptive Impedance-Matching Network Based on a Novel Capacitor Matrix for Wireless Power Transfer," *IEEE Trans. Power Electron.*, vol. 29, no. 8, pp. 4403–4413, 2014.

[84] C. K. Lee, W. X. Zhong, and S. Y. R. Hui, "Effects of Magnetic Coupling of Nonadjacent Resonators on Wireless Power Domino-Resonator Systems," *IEEE Trans. Power Electron.*, vol. 27, no. 4, pp. 1905–1916, 2012.

[85] Y. Narusue, Y. Kawahara, and T. Asami, "Impedance matching method for any-hop straight wireless power transmission using magnetic resonance," in *2013 IEEE Radio and Wireless Symposium (RWS)*, 2013, pp. 193–195.

[86] K. Mori, H. Lim, S. Iguchi, K. Ishida, M. Takamiya, and T. Sakurai, "Positioning-Free Resonant Wireless Power Transmission Sheet With Staggered Repeater Coil Array (SRCA)," *Antennas {...}*, vol. 11, pp. 1710–1713, 2012.

[87] "PowerMat Inc." 2009.

[88] X. Liu and S. Y. R. Hui, "Equivalent Circuit Modeling of a Multilayer Planar Winding Array Structure for Use in a Universal Contactless Battery Charging Platform," *IEEE Trans. Power Electron.*, vol. 22, no. 1, pp. 21–29, 2007.

[89] R. Neufeld, "Contactless energy transfer: Mobile power on the go," *Plant Eng.*, vol. 61, pp. 21–22, 2007.

[90] D. Kurschner and C. Rathge, “Contactless energy transmission systems with improved coil positioning flexibility for high power applications,” in *2008 IEEE Power Electronics Specialists Conference - PESC 2008*, 2008, pp. 4326–4332.

[91] C. J. Stevens, Y. Li, and C. W. T. Chan, “Forward magneto-inductive wave propagation in planar magnetically coupled capacitor grids,” *J. Electromagn. Waves Appl.*, vol. 29, no. 6, pp. 753 – 762, 2015.

[92] L. D. Landau, J. S. Bell, M. J. Kearsley, L. P. Pitaevskii, E. M. Lifshitz, and J. B. Sykes, *Electrodynamics of Continuous Media*. Elsevier, 1984.

[93] O. Sydoruk, O. Zhuromskyy, E. Shamonina, and L. Solymar, “Phonon-like dispersion curves of magnetoinductive waves,” *Appl. Phys. Lett.*, vol. 87, no. 7, p. 72501, 2005.

[94] N. W. Ashcroft and N. D. Mermin, *Solid State Physics*. Cengage Learning, 1976.

[95] C. Chong, F. Watanabe, and H. Inamura, “Potential of UWB Technology for the Next Generation Wireless Communications,” in *2006 IEEE Ninth International Symposium on Spread Spectrum Techniques and Applications*, 2006, pp. 422–429.

[96] Z. L. Yang, “Mutual capacitance-duality principle evolved from planar network,” *IEEE Trans. Circuits Syst. I Fundam. Theory Appl.*, vol. 39, no. 12, pp. 1005–1006, 1992.

[97] Q. Li, M. Soltani, A. H. Atabaki, S. Yegnanarayanan, and A. Adibi, “Quantitative modeling of coupling-induced resonance frequency shift in microring resonators.,” *Opt. Express*, vol. 17, no. 26, pp. 23474–87, 2009.

[98] “PW Circuit Ltd.: Premier Works.” Canal Street, South Wigton, LE18 4PN, Leicester, UK, Leicester.

[99] “Quassia Electronics Ltd. .” Bearwalden Business Park, Wenden Ambo CB11 4JX Saffron Walden, UK.

[100] R. R. A. Syms, L. Solymar, and I. R. Young, “Broadband coupling transducers for magneto-inductive cables,” *J. Phys. D. Appl. Phys.*, vol. 43, no. 28, p. 285003, 2010.

[101] S. P. Thompson, *Dynamo-electric Machinery*. London, New York: E. {&} F.N. Spon., 1886.

[102] E. W. Herold, “Negative Resistance and Devices for Obtaining It,” *Proc. IRE*, vol. 23, no. 10, pp. 1201–1223, 1935.

This page is intentionally left blank